Fenton, C. R., Niedermann, S., Dunai, T., Binnie, S. A. (2019): The SPICE project: Production rates of cosmogenic 21Ne, 10Be, and 14C in quartz from the 72 ka SP basalt flow, Arizona, USA. - *Quaternary Geochronology*, *54*.

DOI: http://doi.org/10.1016/j.quageo.2019.101019

The SPICE Project: Production rates of cosmogenic ^{21}Ne, ^{10}Be, and ^{14}C in quartz from the 72 ka SP basalt flow, Arizona, USA

Cassandra R. Fenton[*, 1, 2, 3]

Samuel Niedermann[3]

Tibor Dunai[2]

Steven A. Binnie[2]

[*]Corresponding author: E-mail: cassiefenton@gmail.com

[1] Present Address: Department of Physical and Environmental Sciences, Colorado Mesa University, Grand Junction, CO 81501, USA

[2] Institut für Geologie und Mineralogie, Universität zu Köln, 50674 Cologne, Germany. sbinnie@uni-koeln.de, tdunai@uni-koeln.de

[3] Deutsches GeoForschungsZentrum, Telegrafenberg, 14473 Potsdam, Germany; nied@gfz-potsdam.de

Revisions submitted for publication in Quaternary Geochronology

August 28, 2019

Keywords: cosmogenic nuclide production rates, ^{21}Ne, ^{10}Be, ^{14}C, quartz, geomagnetic field, SP lava flow

HIGHLIGHTS

- Total reference production rates at SLHL are calculated in 72 ka quartz.
- Cosmogenic ^{21}Ne, ^{10}Be, and ^{14}C rates (*St*): 17.0±1.1, 3.84±0.27, and 11.2±0.6 at/g/yr.
- These rates agree with *St* scaled production rates over past 20 ka in literature.
- There is a proposed period of decreased geomagnetic field strength from 20 to 50 ka.
- SPICE rates do not record increased cosmogenic nuclide production over past 72 ka.

ABSTRACT

The SP lava flow is a quartz-, olivine- and pyroxene-bearing basalt with an $^{40}Ar/^{39}Ar$ age of 72±4 ka (2σ). The flow is preserved in the desert climate of northern Arizona, USA. Its unweathered appearance and the lack of soil development indicate it has undergone negligible erosion and/or burial, making it an ideal site for direct calibration of cosmogenic nuclide production rates. Cross-calibrated production rates and production rate ratios for cosmogenic ^{21}Ne, ^{10}Be, and ^{14}C have been determined from SP flow quartz. Production rate ratios for $^{21}Ne/^{10}Be$, $^{21}Ne/^{14}C$, and $^{14}C/^{10}Be$ are based on the total, local production rates of each cosmogenic nuclide, independent of scaling models, and have error-weighted means (±2σ uncertainty) of 4.44 ± 0.32, 1.43 ± 0.10, and 2.85 ± 0.21, respectively. Error-weighted mean, sea-level, high latitude (SLHL) total reference production rates of ^{21}Ne, ^{10}Be, and ^{14}C are 17.0 ± 1.1, 3.84 ± 0.27, and 11.2 ± 0.6 at/g/yr (2σ), respectively, using time-independent Lal (1991)/Stone (2000) (*St*) scaling factors. *St* scaled spallogenic ^{10}Be and ^{14}C rates are 3.73 ± 0.26 and 9.2 ± 0.6 at/g/yr, respectively. ^{21}Ne and ^{10}Be production rates are integrated over the past 72 ka, whereas ^{14}C production rates are integrated over 25 ka, the time at which SP flow quartz has reached saturation with respect to ^{14}C. These rates overlap within 2σ uncertainty with other *St*-scaled production rates in the literature, including the total reference SLHL ^{21}Ne production rate of Niedermann (2000), which is revised in this paper to 16.8 ± 3.3 at/g/yr (2σ; *St* scaling) to reflect a recent change in age control at the Sierra Nevada sites. All SLHL production rates are lower if time-dependent *Sf*, *Sa*, and *Lm* scaling factors are used. For example, error-weighted mean, sea-level, high latitude (SLHL) total reference production rates for ^{10}Be as calculated in the CREp online calculator range from 3.49 ± 0.23 to 3.74 ± 0.25 at/g/yr (2σ), using time-dependent *Lm* scaling factors. Commonly used SLHL ^{10}Be and ^{14}C production rates in the literature were calibrated on surfaces that have been exposed to cosmic rays for less than 20 ka. Between 20 and 50 ka, the geomagnetic field is proposed to have been weaker than it is today. Production rates of cosmogenic nuclides increase during periods of weaker geomagnetic field strength. However, our study finds no measureable difference between *St*-scaled production rates of cosmogenic ^{21}Ne and ^{10}Be over the past 20 ka and *St*-scaled ^{21}Ne and ^{10}Be production rates over the past 72 ka. As such, the study suggests that ^{21}Ne and ^{10}Be production rates in quartz were not significantly greater during the proposed period of decreased magnetic strength from 20 to 50 ka.

1. Introduction

Cosmogenic-nuclide geochronology has revolutionized Quaternary geology. Scientists can now quantify large-scale, long-term (Myr time-scale) landscape evolution, determine rates of generation and movement of sediment through drainage systems, and date glacial moraines, debris flows, landslides, lava flows, and alluvial/fluvial deposits. Nearly all Quaternary paleoclimate syntheses make use of glacial geochronology studies that rely in large part on cosmogenic nuclide data (Balco, 2011). Cosmogenic nuclide burial dating is even being used for age control at archeological sites (Gibbon et al., 2009; 2014).

Cosmogenic ^{21}Ne, ^{10}Be, and ^{14}C are among the most extensively used nuclides from the cosmogenic nuclide repertoire, because they are formed and retained in quartz, one of the most common minerals on Earth. Cosmogenic ^{21}Ne, ^{10}Be, and ^{14}C are often used in multi-nuclide studies that quantify erosion rates on the short- (^{14}C /^{10}Be), intermediate- (^{26}Al/^{10}Be) and long-term (^{21}Ne/^{10}Be; ^{21}Ne/^{26}Al) timescales. This study focuses on calibration of new cosmogenic ^{21}Ne, ^{10}Be, and ^{14}C production rates in quartz at the 72±4 ka basaltic SP lava flow in northern Arizona.

Production rates of cosmogenic nuclides are determined either directly (calibrated) or indirectly. Calibrated production rates are determined by measuring the concentration of cosmogenic nuclides in rocks (minerals) at sites with independent age control (e.g., radiocarbon dates, ^{40}Ar/^{39}Ar ages). Indirect production rates are calculated in one of two ways: 1) The production-rate ratio technique uses a calibrated production rate for one nuclide to estimate the rate for the other based on the assumption that the production-rate ratio of the two nuclides is constant. For example, a ^{21}Ne production rate can be estimated by multiplying the ratio ^{21}Ne/^{10}Be by the calibrated ^{10}Be production rate. 2) If a mineral has reached saturation with respect to a radionuclide (e.g., ^{14}C), the cosmogenic nuclide production rate equals the decay rate defined as the decay constant times the concentration of the radionuclide. Radioactive saturation, independent of erosion, occurs at sites where the age of the landform is older than four to five half-lives of the cosmogenic radionuclide of interest. Accurate production-rate calibrations, whether they are directly or indirectly calibrated, require negligible erosion rates.

A variety of algorithms, termed scaling methods, have been developed to adjust production rates for local conditions of latitude, longitude, elevation, and time (e.g. Nishiizumi et al., 1989; Lal, 1991; Stone, 2000; Lifton et al., 2014; Lifton, 2016). Scaling for time presents a special problem because fluctuations in the Earth's magnetic field change the intensity of cosmic radiation, and thereby, change the rate of cosmogenic nuclide production. Heretofore, the Lal (1991)/Stone (2000) scaling method (*St*) has been used for calculating constant (or time-independent) scaling factors based on the average strength of the Earth's magnetic field over time. It could be argued the *St* method has been the most often used of scaling methods, and continues to be, even with the advent of time-dependent scaling methods (e.g., *Sf* and *Sa*; Lifton et al., 2014; *Lm*, Nishiizumi et al., 1989; Balco et al., 2008), which account for time-variant weakening and strengthening of the Earth's magnetic field. Abbreviations *St*, *Sf*, *Sa*, and *Lm* are used in this study to be consistent with abbreviations used in Balco et al. (2008), Marrero et al. (2016), and Martin et al. (2017).

Most production rate calibration studies, particularly those focusing on cosmogenic ^{10}Be and ^{14}C, are based on independent ages at calibration sites that are <20 ka (Heyman, 2014 and references therein; Borchers et al., 2016; Martin et al., 2017). Yet, these ^{10}Be production rates are commonly extrapolated to date landforms much older than 20 ka. Landform surfaces older than 20 ka have cosmogenic nuclide inventories which 'integrate' or average temporal changes in rates of cosmogenic nuclide production dependent on magnetic field strength. It has been proposed that Earth experienced a decrease in its magnetic field strength between 20 and 50 ka, and thus increased cosmogenic nuclide production (Lifton et al., 2005; Lifton et al., 2014 and references therein). Minerals, including quartz xenocrysts, in SP flow basalt contain a record of cosmogenic nuclide accumulation that includes this period of higher nuclide production. If the increased production were significant, we would expect it to be detected in measured cosmogenic nuclide concentrations in SP flow minerals.

This paper is the first of several papers planned to present data from the SPICE (**S**P Flow **P**roduction-Rate **I**nter-Calibration Site for **C**osmogenic-Nuclide **E**valuations) project. Here, we present calibrated production rates and production-rate ratios for cosmogenic ^{21}Ne, ^{10}Be, and ^{14}C in 72±4 ka SP flow quartz, and suggest that the *St* scaled production rates can be used to calculate accurate exposure ages and erosion rates even on surfaces between 20 and 70 ka in age.

2. The SP Lava Flow

The SP lava flow and its cinder cone (formally named SP Mountain; Billingsley et al., 2007) are located in the northern part of the San Francisco volcanic field, about 55 km north of Flagstaff, AZ, USA (Figure 1). The flow contains co-existing quartz xenocrysts, olivine, and pyroxene in a dark-gray crystalline basaltic andesite (Billingsley et al., 2007). This is a relatively rare occurrence, as quartz does not usually crystallize in basaltic magmas. The flow is preserved in the arid desert climate of northern Arizona, USA and its youthful, unweathered appearance and the lack of soil development indicate it has undergone negligible erosion (Fenton et al., 2013) (Figures 2, 3, and Figures S1 through S13, found in Supplementary Material).

The SP lava flow retains well-defined lava-flow levees, aa, pressure ridges, and agglutinate features. The SP lava flowed northward from its vent for approximately 6.5 km. The flow is between 6 and 40 m thick and has a rough blocky surface and steep flow fronts. Most of the lava-flow surface is free of desert-pavement and/or soil formation, and appears as the black areas in the satellite image (Figure 2; '2018 SPICE Sample Sites.kmz here'). Areas along the edges of the flow, mainly on the western side, do have occasional, well-developed patches of pavements overlying the fine-grained A soil horizon (A_v; 10-15 cm deep; McFadden et al., 1998). These areas are the gray-to-green colored areas in the satellite image of the SP lava flow.

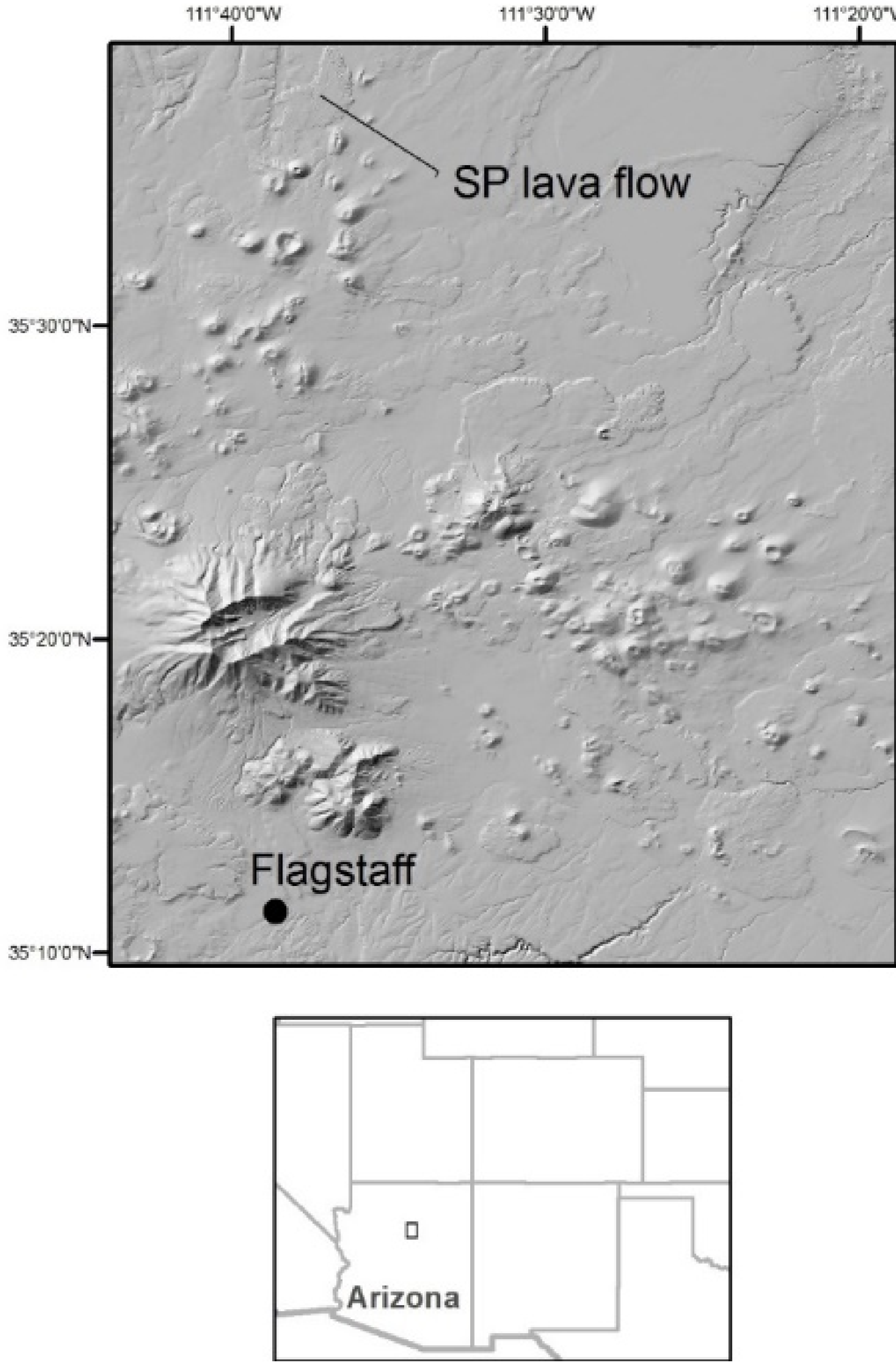

Figure 1. Location of the SP lava flow in the San Francisco volcanic field, north of Flagstaff, Arizona. The small box in the lower figure indicates the extent of the top image.

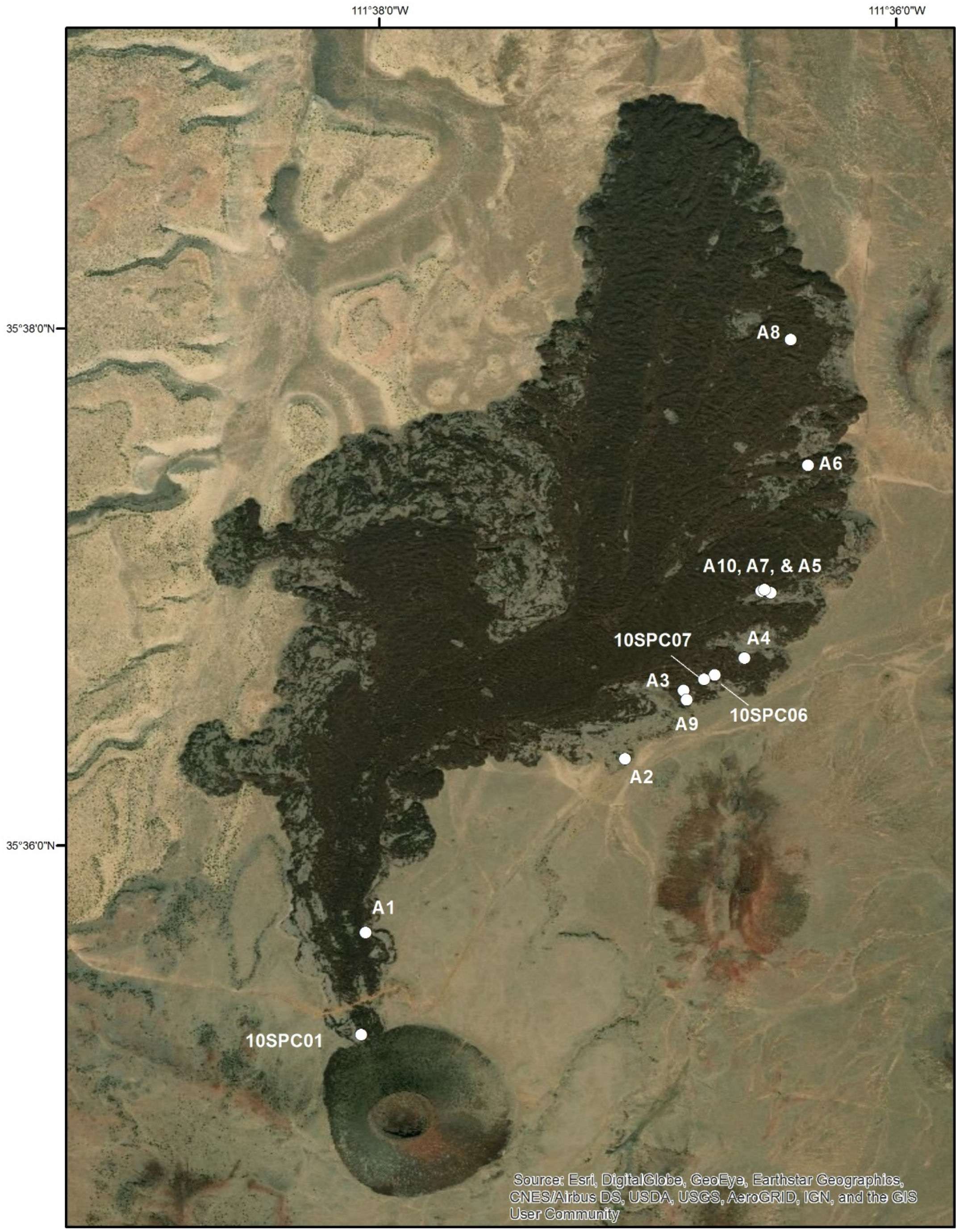

Figure 2. Satellite image of the SP lava flow and its cinder cone. White circles indicate locations of SPICE sample sites. Table 1 lists the latitude, longitude, and elevation of each SPICE sample site. An interactive Google Earth map is also available '2018 SPICE Sample Sites.kmz here', so it is possible to zoom in on a specific sample site.

Table 1. Information on sampling locations and sample types collected from the SP lava flow and SP Crater in the San Francisco volcanic field in northern Arizona, USA. An interactive Google Earth map is also available '2018 SPICE Sample Sites.kmz here', where it is possible to zoom in on a specific sample site.

Location/ Sample	Latitude (°N)	Longitude (°W)	Elev. (m)	Collected rock mass (kg)	Maximum sample thickness (cm)	Bulk whole-rock density (g/cm^3)[a]	Dip (°)	Dip azimuth	Topographic shielding factor[b]	Sample thickness shielding factor[c]	Total shielding factor [d]	Pre-acid etching quartz mass[e](g)	Quartz mass used in ^{10}Be analysis (g)	Quartz mass used in ^{21}Ne analysis (g)	Quartz mass used in ^{14}C analysis (g)
SPICE-															
A1	35.5944	111.6342	1837	19.1	8	2.25	0	n/a	0.999	0.946	0.945	6.10	2.1608	0.48040	1.001167
A2 [g]	35.6056	111.6175	1807	30.5	8	2.26	0	n/a	0.999	0.946	0.945	5.39	2.0711 2.0559	0.47372	0.989148
A3 [g]	35.6100	111.6137	1810	24.1	13	2.15	0	n/a	0.999	0.918	0.917	8.16	2.1188 2.0803	0.48278	0.957357
A4	35.6121	111.6098	1803	30.9	13	2.13	12	45	0.998	0.918	0.916	10.09	2.0803	0.80032	0.983676
A5	35.6163	111.6081	1800	26.8	13	2.28	0	n/a	1.000	0.913	0.913	8.53	2.1358	0.48470	0.993877
A6 [g]	35.6245	111.6057	1778	29.5	12	2.29	0	n/a	1.000	0.919	0.919	7.35	2.0919 2.1112	0.48494	0.971801
A7	35.6164	111.6087	1800	25.9	13	2.45	0	n/a	1.000	0.907	0.907	6.78	2.0676	0.47508	0.983313
A8	35.6326	111.6068	1778	25.0	13	2.05	15	38	0.997	0.921	0.918	12.19[f]	2.1340	0.80998	0.999341
A8 [g]	35.6326	111.6068	1778	25.0	13	2.05	15	38	0.997	0.921	0.918	12.19[f]	2.1391 2.1340	0.80998	0.999341
A9	35.6094	111.6135	1810	30.5	13	2.29	0	n/a	0.999	0.912	0.912	8.49	2.0503	0.46248	1.061305
A10	35.6165	111.6085	1800	25.0	12	2.31	7	315	0.999	0.918	0.917	5.32	2.0525	0.48178	0.978158
10SPC01	35.5878	111.6345	1876	n/a	6	2.25	0	n/a	0.985	0.959	0.945	n/a	n/a	0.52770	n/a
10SPC06	35.6110	111.6117	1799	n/a	6	2.25	15	45	0.999	0.959	0.958	n/a	n/a	0.50342	1.052221
10SPC07	35.6107	111.6124	1787	n/a	6	2.25	23	233	0.995	0.959	0.954	n/a	n/a	0.73352	1.070891

Note: All SPICE samples were collected from the exposed surfaces of pressure ridges on the SP lava flow. Samples 10SPC01, 10SPC06, and 10SPC07 were collected in 2010. All other SPICE samples were collected in 2015. n/a = not applicable or not available.

[a] Bulk densities were measured for each sample, except for samples 10SPC01, -06, and-07, for which densities reported here are an average of the measured densities for samples SPICE-A1 to -A10.

[b] Calculated using CRONUSCalc Topographic Shielding Calculator version 2.0 (Marrero et al., 2016).

[c] Calculated using CRONUS-EU CosmoCalc version 3.0 (Vermeesch, 2007) with the bulk whole-rock density measured or reported for each sample and an exponent of topographic shielding correction of 2.3.

[d] The total shielding factor includes corrections for sample depth (self-shielding) and topographic shielding, which includes dipping of a sample site surface, when present. Shielding factor = 1.0 equates to no shielding correction.

[e] Samples yielded quartz concentrates (>75% quartz) in the 125-1000 µm fraction, unless otherwise noted. Masses reported here are the amounts of quartz extracted from each basalt sample prior to any treatment with HF acid.

[f] Sample yielded quartz concentrates in the 90-1000 µm fraction.

[g] Sufficient purified quartz was obtained to allow duplicate sample preparation and ^{10}Be measurement. Listed masses are those used in duplicate sample preparation and AMS measurements.

The age of the SP lava flow has been debated since the first K-Ar age (70±8 ka; 2σ) was reported by Baksi (1974). Many volcanologists who studied the flow argued that the flow surface appeared “too young” to be 70 ka. More age-dating studies followed. Quartz xenocrysts in the SP flow yielded OSL ages of 5.5-6 ka (Rittenour et al., 2012). Fenton et al. (2013) reported an age of 72±4 ka (2σ; ± 5.6%) for the SP lava flow, based on ^{40}Ar/^{39}Ar analysis of three basalt groundmass samples (Figure 4). The ^{40}Ar/^{39}Ar age is in excellent agreement with the previously reported K-Ar age (70±8 ka; Baksi, 1974). Fenton and Niedermann (2014) also report an exposure age of 69±7 ka based on cosmogenic ^{3}He and ^{21}Ne concentrations in SP flow pyroxene (*St* scaling) and production rates from Goehring et al. (2010) and Fenton et al. (2009). The ^{3}He and ^{21}Ne exposure ages further substantiate the ^{40}Ar/^{39}Ar and K-Ar ages. The strong agreement between initial cosmogenic ^{3}He and ^{21}Ne data and the existing ^{40}Ar/^{39}Ar and K-Ar ages indicates that the SP flow has undergone negligible erosion and is suitable for cross-calibrating production rates of cosmogenic nuclides. The small uncertainty (± 5.6%) of the ^{40}Ar/^{39}Ar age, in combination with lack of erosion or burial and the presence of quartz, olivine, and pyroxene in the basalt, made the SP lava flow an obvious candidate as a primary calibration site for cosmogenic nuclide production rates (Fenton et al., 2013; Fenton and Niedermann, 2014).

3. Background on Terrestrial Cosmogenic Nuclides

Cosmogenic nuclides are produced by spallation reactions induced by high-energy nucleons, secondary thermal and epithermal neutron capture reactions, and muon-induced reactions (Gosse and Phillips, 2001). Cosmogenic nuclides produced by spallation reactions and those produced by muon-induced reactions are referred to as spallogenic and muogenic nuclides, respectively. Spallation reactions are the dominant mechanism by which cosmogenic nuclides are produced in rocks at the Earth's surface.

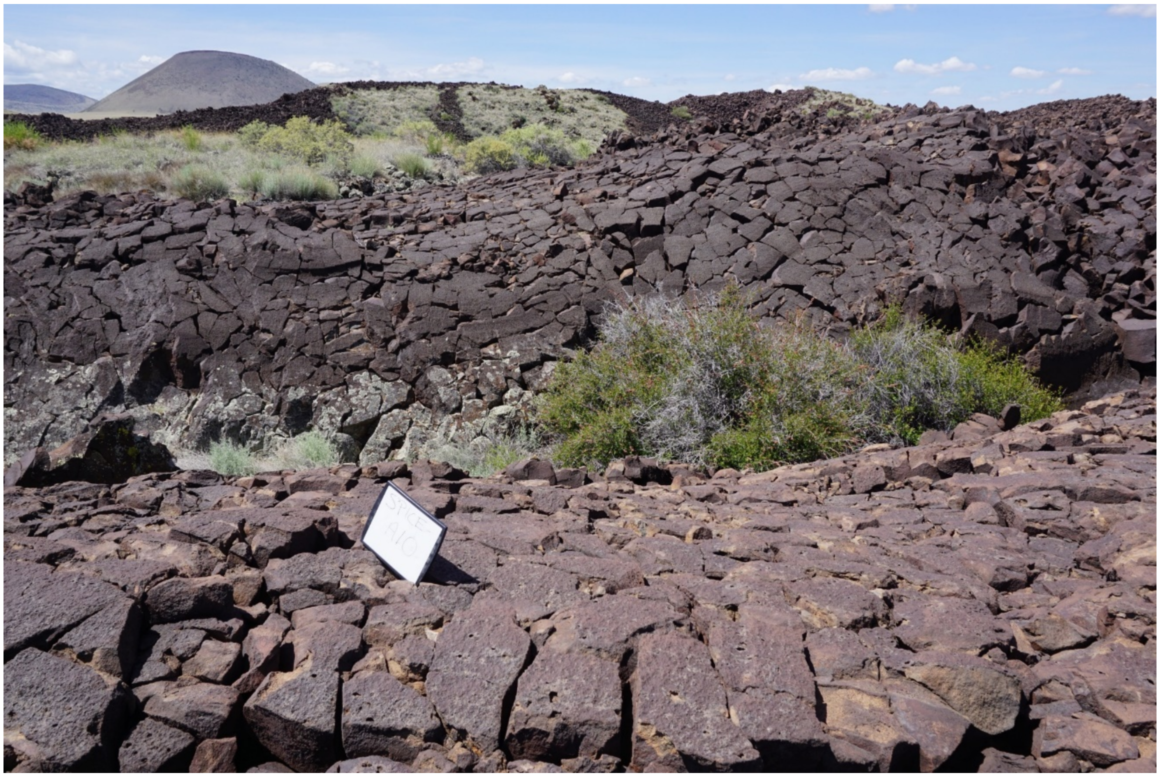

Figure 3. Photograph of a representative pressure ridge at the SP lava flow. The whiteboard stands 8.5 inches tall and is on the surface from which SPICE-A10 was collected. Note the continuity of the pressure-ridge surfaces and the well-developed desert varnish, indicating negligible erosion.

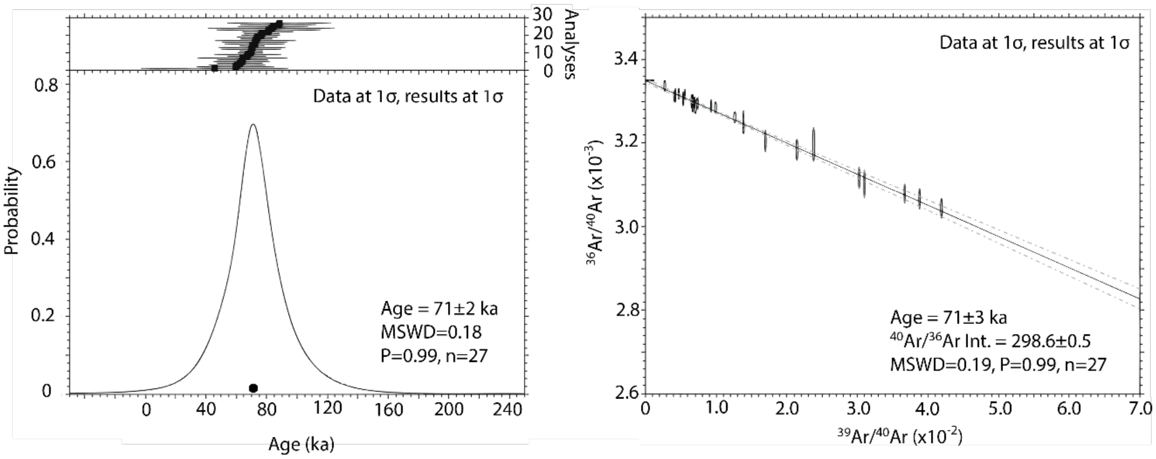

Figure 4. Relative probability plot (left) showing all age steps from the three $^{40}Ar/^{39}Ar$ step-heating experiments for the SP flow samples. The isotope correlation plot (right) also shows all age steps from the three step-heating experiments for the SP flow. Figure is modified from Fenton et al. (2013) and the age (72±4 ka) of the SP flow is recalculated relative to the optimization model of Renne et al. (2010).

The production of in-situ cosmogenic nuclides is dominantly controlled by the flux of galactic cosmic rays (with energies >100 MeV) through Earth's atmosphere (Cerling and Craig, 1994). This flux of nucleons (primarily protons and alpha particles) is modulated by the strength of the Earth's magnetic field. During periods of weaker magnetic strength, the flux is higher. Secondary particles (i.e. neutrons) responsible for cosmogenic nuclide production at the Earth's surface are created during nucleonic interactions between galactic cosmic rays and elements in the Earth's upper atmosphere. These secondary particles then penetrate rocks/minerals, striking target atoms (e.g., O, Mg, Si, etc.) and causing spallation reactions that produce terrestrial cosmogenic nuclides (Gosse and Phillips, 2001), such as ^{21}Ne, ^{10}Be, and ^{14}C.

The production rates of these nuclides in rocks are highest in the upper 4 cm of the Earth's surface, and are dependent not only on the Earth's magnetic field strength, but also on the chemical composition of the bulk-rock and mineral of interest and on the latitude and elevation where the rock or mineral of interest is located.

Production rates increase with increasing latitude and elevation. Longitude plays a smaller role in modifying production rates, but is sometimes considered because of the non-dipole nature of the Earth's magnetic field (Gosse and Phillips, 2001; Dunai, 2001; Lifton et al., 2005; Lifton et al., 2014). In addition, sample depth affects production rates. Generally, the production rate of a cosmogenic nuclide decreases exponentially with increasing depth (Gosse and Phillips, 2001).

There are stable cosmogenic nuclides (e.g., ^{21}Ne) and radioactive cosmogenic nuclides (e.g., ^{10}Be and ^{14}C). In the absence of erosion or burial, concentrations of stable nuclides accumulate with time (Equation 1),

$$C(t) = P_0 t \qquad \text{[Eq. 1]}$$

where C is the concentration of the stable nuclide as a function of time (t), and P_0 is the production rate of the stable nuclide. In the same conditions, concentrations of radionuclides ($C(t)$) are governed by their production rates (P_0) and their decay constants (λ) (Equation 2),

$$C(t) = \frac{P_0}{\lambda}\left(1 - e^{-\lambda t}\right) \qquad \text{[Eq. 2].}$$

When the production rate of a cosmogenic radionuclide equals its decay rate (or $\lambda C(t)$), the radionuclide has reached secular equilibrium. Concentrations of nuclides at secular equilibrium are, thus, governed by their production rate and decay constant (Equation 3),

$$C(t) = \frac{P_0}{\lambda} \qquad \text{[Eq. 3].}$$

Radioactive nuclide saturation (>95%) can be assumed to occur between 4 and 5 half-lives (Lifton et al., 2001). Erosion, burial, and cover (i.e. soil, snow, dust, etc.) will affect the concentrations of cosmogenic nuclides in a given rock or mineral sample by decreasing production via shielding.

The total production rate of a cosmogenic nuclide includes spallation production and muon-induced production at a given latitude, longitude, and elevation. Muogenic ^{10}Be and ^{21}Ne only contribute a small fraction (~2%) to total ^{10}Be and ^{21}Ne production at the Earth's surface (Heisinger et al., 2002a; 2002b; Balco et al., 2008; 2009; Goethals et al., 2009; Kober et al., 2011;). In contrast, the muogenic component of the total reference ^{14}C production rate is significantly higher at the Earth's surface (~20%; Heisinger et al., 2002a; 2002b; Lupker et al., 2015). Spallation production rates for ^{21}Ne, ^{10}Be, and ^{14}C include production of each nuclide from fast-muon induced spallation, following Lal (1991)/Stone (2000) and Dunai (2000). Muogenic contributions (2%) to the total ^{21}Ne production rate should only come from fast muon interactions (Balco and Shuster, 2009; Goethals et al., 2009; Kober et al., 2011), and recent data confirms production of ^{21}Ne from negative muon capture is indeed negligible (Balco et al., 2019). Consequently, no distinction between total and spallogenic production rates of ^{21}Ne is made in this paper.

Because production rates vary by latitude, longitude, and elevation, and because they also vary with time-dependent fluctuations in the Earth's magnetic field strength, scientists have set out over the past few decades to establish production-rate calibration sites all over the globe. The goal has been to increase the accuracy of global, average production rates, such that associated uncertainties are minimized to less than 5% (Phillips, 2016).

Scientists contributing to the global production-rate database have been striving to quantify the time-and-space variability in production rates and to use this variability to construct or improve scaling methods (Nishiizumi et al., 1989; Lal, 1991; Stone, 2000; Dunai 2000, 2001; Desilets and Zreda, 2003; Lifton et al., 2005; Desilets et al., 2006; Lifton et al., 2014; Lifton, 2016). These scaling methods comprise complex algorithms that calculate scaling factors, which are used to normalize 'local' production rates from various elevations and latitudes to a sea-level and high-latitude (>60°) (SLHL) production rate. Conversely, the scaling factors are also used as 'multipliers' to scale a SLHL production rate to a local production rate (for a specific latitude, longitude, and elevation).

Until recently, the combined Lal (1991)/Stone (2000) model (*St*) has been the most commonly used scaling model. This time-independent model calculates a constant scaling factor for a given latitude and elevation. In the *St* model, scaling-factor values are mainly controlled by the geographic position of a sample site. Other models are time dependent and account for documented variations in the strength of the geomagnetic field. The time-dependent models (*Sf* and *Sa*) were developed by Lifton et al. (2014). *Sf* scaling factors can be used with any cosmogenic nuclide, whereas *Sa* scaling factors are nuclide specific. The time dependent *Lm* scaling method (denoted as *Lm* by Balco et al., 2008) is based on the *St* model of Lal (1991)/Stone (2000) and is modified for geomagnetic corrections as described in Nishiizumi et al. (1989). In general, sites at high latitudes and high elevations will have higher resultant scaling factors than sites at low latitudes and low elevations.

Sf, Sa, and Lm scaling factors also account for periods of lower or higher nuclide production that are tied to the strengthening or weakening of the Earth's magnetic field, respectively (Nishiizumi et al., 1989; Lifton et al., 2014; Lifton, 2016). Periods of weak field strength result in higher nuclide production, and thus result in an increase in the scaling factor value at, and vice versa. The SP lava flow surface has been exposed to cosmic rays for the past 72 ka, which includes a proposed period of higher cosmic-ray flux between 20 and 50 ka, when the Earth's magnetic field was weaker than it is now (Figure 5; Lifton et al., 2014). *Sf* and *Sa* scaling factors are calculated to incorporate the proposed increase in cosmogenic nuclide production. *Lm* scaling factors calculated in the online CREp calculator (https://crep.otelo.univ-lorraine.fr/#/init; Martin et al., 2017) using the "LSD Framework" also incorporate this proposed increase in production. CREp *Lm* scaling factors are calculated using three different virtual dipole moment (VDM) databases: (1) the atmospheric ^{10}Be-based VDM of Muscheler et al. (2005) and Valet et al. (2005); (2) the Lifton VDM of Lifton (2016); and (3) the LSD Framework of Lifton et al. (2014). In this study, these three virtual dipole moment databases are referred to as VDM 1, VDM 2, and VDM 3, respectively.

VDM 1 and VDM 2 indicate a period of only slightly decreased virtual dipole moment, or geomagnetic field strength, between 20 and 50 ka, whereas VDM 3 indicates a more pronounced decrease during the same time period (Figure 5). VDM 3 values are predominantly between 4×10^{22} and $6 \text{ x } 10^{22}$ Am^2, whereas VDM 1 and VDM 2 values are predominantly between 5×10^{22} and 10×10^{22} Am^2.

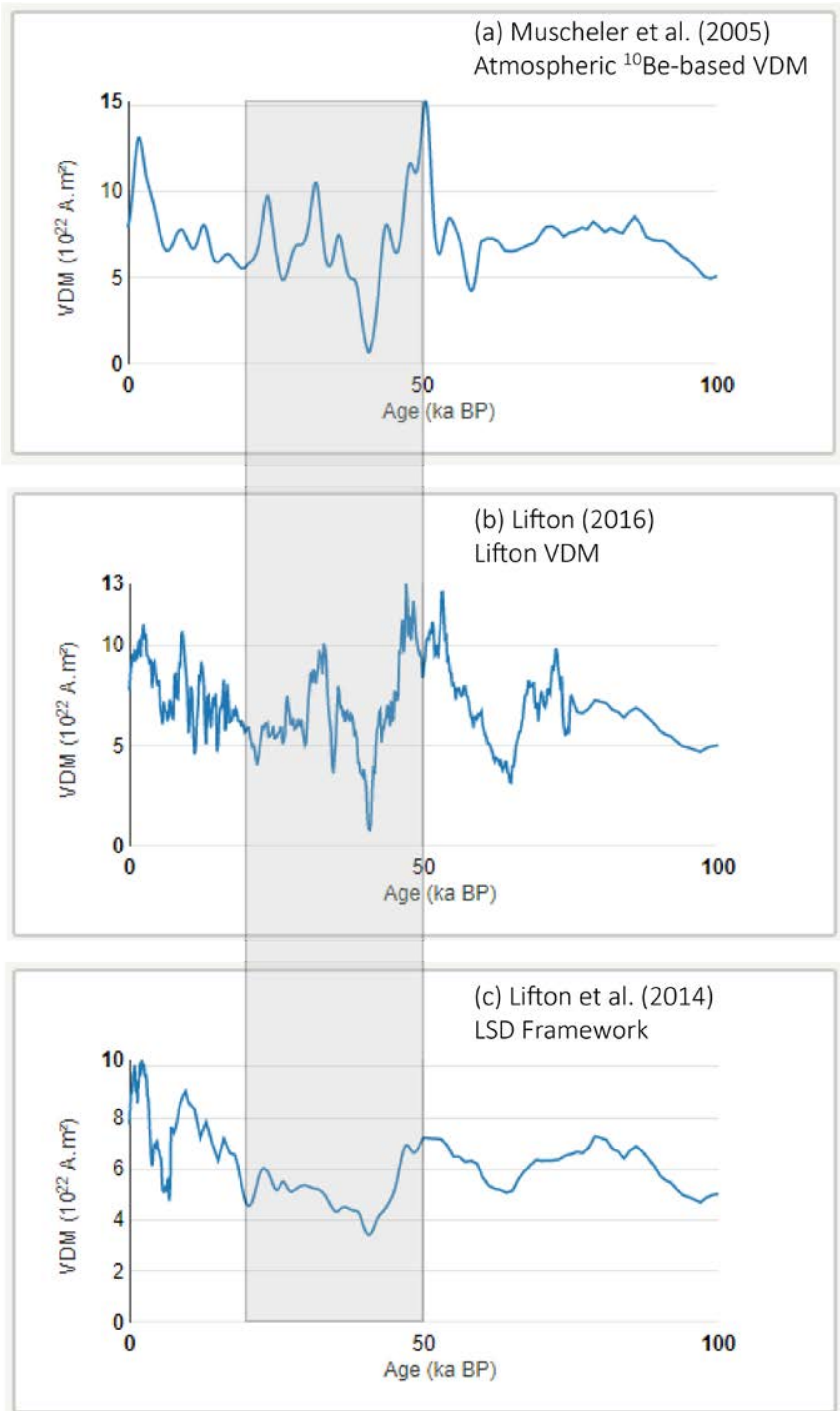

Figure 5. Three virtual dipole moment (VDM) models as displayed on the CREp parameters webpage (https://crep.otelo.univ-lorraine.fr/#/init) (modified from Martin et al., 2017). The transparent gray box indicates the period of increased cosmogenic nuclide production between 20 and 50 ka proposed by Lifton et al. (2014).

4. Current Values of Production Rates for ^{21}Ne, ^{10}Be, and ^{14}C in Quartz

Impressive progress has been made over the past 30 years in determining cosmogenic nuclide production rates, but there still exists a need to refine production rates. Though the ^{10}Be production rate is reasonably well constrained, with data from at least 24 different direct-calibration studies contributing to calculation of the global average SLHL value (Nishiizumi et al., 1989; Gosse et al., 1995; Larsen, 1996; Kubik et al., 1998; Stone et al., 1998; Kubik and Ivy-Ochs, 2004; Farber et al., 2005; Balco et al., 2009; Putnam et al., 2010; Fenton et al., 2011; Kaplan et al., 2011; Ballantyne and Stone, 2012; Briner et al., 2012; Goehring et al., 2012; Blard et al., 2013; Young et al., 2013; Heyman, 2014; Kelly et al., 2015; Small and Fabel, 2015; Stroeven et al., 2015; Lifton et al., 2015; Martin et al., 2015; Borchers et al., 2016; Martin et al., 2017; Putnam et al., 2019), calibration sites at low latitudes and calibration sites older than 20 ka are still needed. Importantly, aside from SPICE data reported in this study, all ^{10}Be production rates contributing to the average global SLHL production rate are based on landform surfaces exposed for less than 20 ka. SLHL ^{21}Ne and ^{14}C production rates are constrained by fewer studies (6 and 4, respectively; Figures 6 and 7). More calibration sites are also needed around the world for more robust calculations of global, average SLHL ^{21}Ne and ^{14}C production rates. While global, average production rates for multiple cosmogenic nuclides have been updated several times over the past 11 years (e.g., Balco et al., 2008; Heyman, 2014; Borchers et al., 2016; Martin et al., 2017), it is useful to think of cosmogenic nuclide production-rate research as a ‘work in progress’, to which the SPICE project is contributing, particularly with regard to ^{21}Ne, ^{10}Be, and ^{14}C production in quartz. The ICE-D calibration database addresses this ‘work in progress’ issue with regular updates to production-rate data when new studies are published (http://calibration.ice-d.org/; Martin et al., 2017). The ICE-D data is linked to the online calculators of Balco et al. (2008) and the CREp calculator of Martin et al. (2017).

Cosmogenic ^{21}Ne, ^{10}Be, and ^{14}C are produced and retained in quartz, one of the most abundant minerals on the Earth's surface. The concentration of ^{21}Ne, a stable nuclide, is limited only by processes such as burial and erosion of a landform's surface. As such, ^{21}Ne is an ideal cosmogenic nuclide for dating surfaces with exposure histories up to $10^6 – 10^7$ years.

Cosmogenic ^{21}Ne in quartz has been used in studies since the 1990s, but it has really grown in popularity since 2000, particularly in multi-nuclide surface-process research (e.g., Phillips et al., 1998; Summerfield et al., 1999; Hetzel et al., 2002; Tschudi et al., 2003; Ivy-Ochs et al., 2006, 2007, Kober et al., 2007, 2011; Strobl et al., 2012; Decker et al., 2013; Balco et al., 2014; Codilean et al., 2014; Matmon et al., 2014; Kounov et al., 2015; Ma et al., 2016; McPhillips et al., 2016; Pavićević et al., 2016). Still, the direct calibration of the cosmogenic ^{21}Ne production rate in quartz remains poorly constrained relative to the direct calibration of the ^{10}Be production rate. Only one published direct calibration of the ^{21}Ne production rate in quartz exists (Niedermann et al., 1994; revised by Niedermann, 2000). That rate is based on two samples (WGS-8 and WGS-12) from a site in the Sierra Nevada (California) exposed by deglaciation during the late Pleistocene. In 2000, new age control at the site resulted in a revision of the production rate to 20.3 ± 3.8 at/g/yr (Niedermann, 2000; *St* scaling). Glacier retreat was originally thought to be at 11 ka, and was then changed to 13 ka, with ^{10}Be and ^{26}Al exposure ages calibrated against radiocarbon data in the study area (Nishiizumi et al., 1989; Clark et al., 1995).

More recently, age control has changed at the site again. Phillips (2016) and Phillips et al. (2016) now conclude glacier retreat occurred at the sample sites at 15.75 ka. Herein, the total reference SLHL ^{21}Ne production rate of Niedermann (2000) is revised to reflect this change in age control at the Sierra Nevada sites. The new total reference ^{21}Ne production rate is 16.8 ± 3.3 at/g/yr (2σ; *St* scaling; Figure 6).

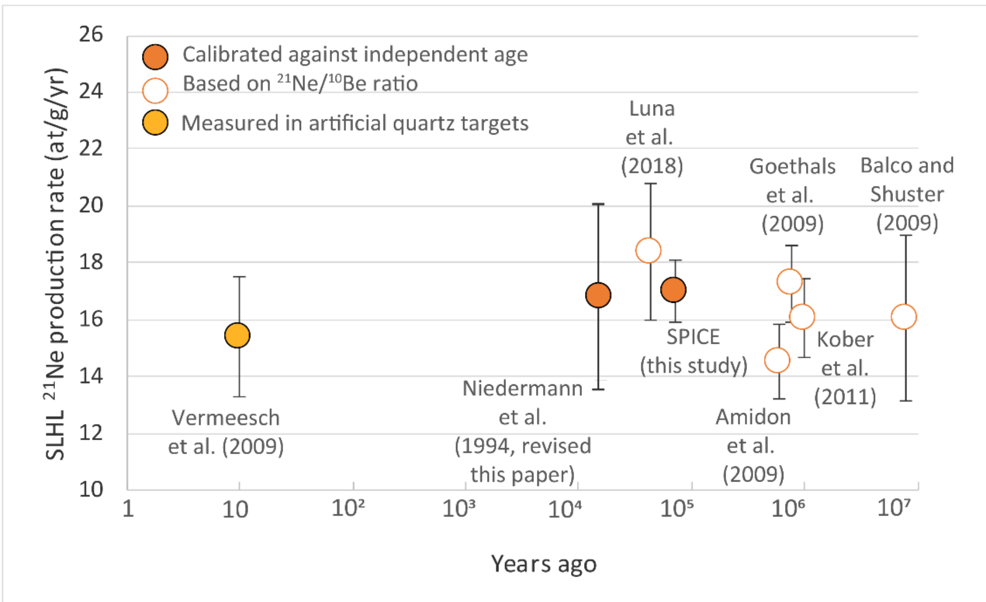

Figure 6. Error-weighted mean total reference SLHL production rate for ^{21}Ne in SPICE quartz samples (17.0±1.1 at/g/yr), and published SLHL ^{21}Ne rates recalculated in this study. The $^{10}Be_{sp}$ production rate of 4.01 at/g/yr (Borchers et al., 2016) is used in combination with published $^{21}Ne/^{10}Be$ values to estimate related ^{21}Ne production rates (white circles). Values are scaled with the *St* method. The production-rate ratios of Luna et al. (2018) incorporate an erosion rate of 1 mm/ka.

The remaining five ^{21}Ne production rates in quartz are indirectly determined and based on $^{21}Ne/^{10}Be$ production-rate ratios at the sample sites, in combination with use of a SLHL ^{10}Be production rate (Amidon et al., 2009; Balco and Shuster, 2009; Goethals et al., 2009; Kober et al., 2011; Luna et al., 2018) such that,

$$P_{21Ne} = \left(\frac{^{21}Ne}{^{10}Be}\right) \times P_{10Be} \qquad \text{[Eq. 4].}$$

The production rate of ^{10}Be (P_{10Be}; Eq. 4) is based on Equation 2. ^{21}Ne and ^{10}Be are measured concentrations of each nuclide, where the measured concentration of ^{10}Be is corrected for the decay of ^{10}Be over time.

The SLHL ^{10}Be production rates used previously by Amidon et al. (2009), Balco and Shuster (2009), Goethals et al. (2009), and Kober et al. (2011) were between 4.23 and 5.01 at/g/yr, depending on the study and whether the study incorporated the new, lower ^{10}Be half-life published by Chmeleff et al. (2010) and Korschinek et al. (2010). The Luna et al. (2018) study uses the SLHL reference production rate in the high, tropical Andes (4.02 ± 0.12 at/g/yr; Kelly et al., 2015 and Martin et al., 2015). Sample sites from Amidon et al. (2009) and Goethals et al. (2009) had independent age control, but the effects of erosion or burial were such that calculating a ^{21}Ne production rate based directly on the independent age would have underestimated the production rate.

More recently, the global, average SLHL spallogenic ^{10}Be production rate (*St*-scaled) has been determined to be 3.99 or 4.01 at/g/yr (*St*; Heyman, 2014; Borchers et al., 2016) or 4.06 - 4.11 at/g/yr (*Lm*-scaled; CREp online calculator; Martin et al., 2017). The ^{10}Be production rate of Borchers et al. (2016) is used here to recalculate published ^{21}Ne production rates determined by the ratio method (Figure 6; Amidon et al., 2009; Balco and Shuster, 2009; Goethals et al., 2009; Kober et al., 2011). Using the spallogenic P_{10Be} of 4.01 at/g/yr, the indirectly determined ^{21}Ne production rates now range from 14.6 to 18.1 at/g/yr, which are in good agreement with the revised value of the directly calibrated spallogenic ^{21}Ne production rate (Niedermann et al., 1994; Niedermann, 2000) of 16.8 ± 3.3 at/g/yr (*St* scaling; this paper) (Figure 6).

The independent ages of the calibration sites in the ^{21}Ne/^{10}Be ratio studies range much farther back in geologic time than do the independent ages for ^{10}Be and ^{14}C production-rate studies. The studies of Amidon et al. (2009), Balco and Shuster (2009), and Goethals et al. (2009) were at sites with ages of 610 ka, >8 Ma, and 760 ka, respectively. Amidon et al. (2009) and Goethals et al. (2009) report significant and observable erosion at their sample sites. That adds a factor of uncertainty to ^{21}Ne/^{10}Be production ratios of Amidon et al. (2009) and Goethals et al. (2009) (3.56±0.16 and 4.31±0.17; 1σ, respectively), even though Goethals et al. (2009) do their best to quantify erosion at their calibration site and consider its effect on the ^{21}Ne production rate.

Balco and Shuster (2009) base their spallogenic ^{21}Ne production rate (recalculated here to be 16.4 ±3.0 at/g/yr; 2σ; *St* scaling) on ~8-14 Ma surfaces in Antarctica, where erosion is quantified by cosmogenic ^{26}Al and ^{10}Be concentrations. Balco and Shuster (2009) report a ^{21}Ne/^{10}Be production ratio of 4.08±0.37 (n = 9), which is nearly identical to that of Kober et al. (2011) of 4.01 ± 0.17 (*St*). Balco and Shuster's (2009) data are used in the CRONUSCalc online calculator (Marrero et al., 2016) and CRONUSCalc documentation lists the spallogenic ^{21}Ne production rates as 16.63 (*St*) and 16.96 at/g/yr (*Sf*) (Table 2).

The Kober et al. (2011) study yields a spallation ^{21}Ne production rate (recalculated here to be 16.1 ± 1.4 at/g/yr; 2σ) based on a statistical analysis of all published ^{21}Ne/^{10}Be data (n=95) produced at ETH Zurich, where all ^{10}Be data was corrected for the new ^{10}Be half-life (1.387 Ma; Chmeleff et al., 2010; Korschinek et al., 2010). Twenty-five percent of the samples have exposure ages younger than 50 ka, and 75% have ages < 1 Ma. The oldest samples (~6 - 10 Ma) are from Antarctica (Schäfer et al., 1999; Di Nicola et al., 2009).

The Luna et al. (2018) study reports a ^{21}Ne production rate (18.1 ± 2.4 at/g/yr; 2σ) based on ^{21}Ne/^{10}Be production ratios measured in 11 quartz samples. Luna et al. (2018) calculate exposure ages of 38.9 to 392 ka for moraines from which the eleven samples were collected. Five of these samples are from moraines with exposure ages ranging from 38.9 to 49.6 ka. These ages fall within the 20-50 ka period of decreased geomagnetic field strength. If these five samples are considered alone, they yield an error-weighted mean ^{21}Ne recalculated production rate of 18.4 ± 2.4 at/g/yr (2σ; plotted in Figure 6), which is only 1.7% greater than the ^{21}Ne production rate of 18.1 ± 1.2 at/g/yr (2σ) Luna et al. (2018) calculated with all 11 samples. The five samples of Luna et al. (2018) from moraines between 38.9 to 49.6 ka do thus not record any significant increase in ^{21}Ne production in quartz (Figure 6).

Table 2. Comparison of spallation production rates in quartz from this study to those reported by Borchers et al. (2016), Niedermann (2000), and Marrero et al. (2016).

Cosmogenic nuclide	SLHL Production Rate *St* (at/g/yr)	SLHL Production Rate *Sf* (at/g/yr)	SLHL Production Rate *Sa* (at/g/yr)
SPICE $^{10}Be_{sp} \pm 2\sigma$ [a]	**3.73 ± 0.26**	**3.43 ± 0.24**	**3.30 ± 0.23**
SPICE $^{10}Be_{sp} \pm 2\sigma_{SD}$ [b]	3.75 ± 0.18	3.45 ± 0.13	3.31 ± 0.16
$^{10}Be_{sp}$ (Borchers et al., 2016)	4.01	4.09	3.92
SPICE $^{14}C_{sp} \pm 2\sigma$ [a, c]	**9.2 ± 0.6**	**9.5 ± 0.6**	**9.5 ± 0.6**
SPICE $^{14}C_{sp} \pm 2\sigma_{SD}$ [b, c]	9.2 ± 1.7	9.5 ± 1.7	9.6 ± 1.7
$^{14}C_{sp}$ (Borchers et al., 2016)	12.24	12.72	12.76
SPICE $^{21}Ne \pm 2\sigma$ [a]	**17.0 ± 1.1**	**15.5 ± 1.0**	--
SPICE $^{21}Ne \pm 2\sigma$ [b]	16.7 ± 2.1	15.3 ± 1.9	--
$^{21}Ne \pm 2\sigma$ (Niedermann et al., 1994; revised in this paper)	16.8 ± 3.3	16.5 ± 3.2	--
^{21}Ne (Marrero et al., 2016)	16.63	16.96	--

Note: SPICE production rates are based on data reported in Tables 3, 4, 5, and SD1, SD2, SD3, SD4. *St* refers to the time-independent scaling method of Lal (1991)/Stone (2000). *Sf* and *Sa* refer to the time-dependent scaling methods of Lifton et al. (2014) for non-nuclide specific and nuclide specific factors, respectively. -- indicates there was no code yet available online to calculate *Sa* scaling factors for ^{21}Ne at SPICE calibration sites, though the documentation for the code of Marrero et al. (2016) lists a *Sa* SLHL production rate for ^{21}Ne. The subscript *sp* refers to a production rate produced by spallation reactions. This includes fast-muon induced spallation reactions included in the ^{21}Ne production rate.

[a] This is the error-weighted mean and standard error of the mean for all samples and includes the uncertainty of the $^{40}Ar/^{39}Ar$ age or ^{14}C half-life.

[b] This is the arithmetical mean and two standard deviations ($2\sigma_{SD}$) of all samples; $2\sigma_{SD}$ does not include uncertainty of the $^{40}Ar/^{39}Ar$ age or radiocarbon half-life.

[c] Time-dependent SLHL production rates for ^{14}C are calculated using *Sf* and *Sa* scaling factors integrated over the past 25 ka. This equates to 4.5 ^{14}C half-lives, at which time quartz in the SP flow reached 95% saturation. Carbon-14 reaches secular equilibrium between 25 and 30 ka (e.g., the decay of ^{14}C atoms ≈ the production of in-situ ^{14}C atoms) (Lifton et al., 2001). Samples SPICE-A7 and –A9 are excluded from mean values presented here.

Lastly, there is one study that measured present-day production of cosmogenic ^{21}Ne in artificial quartz targets placed at high altitude in the Swiss Alps for one year (Vermeesch et al., 2009). The reported SLHL ^{21}Ne production rate (15.4 ± 2.1 at/g/yr) is in excellent agreement with the Sierra Nevada calibration site, as well as with the ratio-determined ^{21}Ne production-rate estimates of Amidon et al. (2009), Balco and Shuster (2009), Goethals et al. (2009), Kober et al. (2011), and Luna et al. (2018).

In summary, SLHL ^{21}Ne spallation production rates in quartz and artificial quartz targets range from 14.6 to 18.1 at/g/yr, and the only primary, geological calibration (Niedermann et al., 1994) of the total reference SLHL ^{21}Ne production rate in quartz is now 16.8 ± 3.3 at/g/yr (*St* scaling; revised this paper; Figure 6).

The estimate for the global, average SLHL ^{10}Be production rate from spallation has decreased by ~20% from 4.96±0.43 at/g/yr (*St*; Balco et al., 2008) to 3.99±0.22 at/g/yr (Heyman, 2014) or 4.01 at/g/yr (no error stated; Borchers et al., 2016) with the addition of new ^{10}Be calibration sites, and with the improved ^{10}Be half-life and standardization studies of Chmeleff et al (2010), Korschinek et al. (2010), and Nishiizumi et al. (2007). Borchers et al. (2016) performed a rigorous statistical analysis of published ^{10}Be calibration data sets and reported a best-fitting spallation ^{10}Be production rate of 4.01 at/g/yr (*St* scaling). This rate, however, does not include ^{10}Be production rates published since 2010 (Putnam et al., 2010; Fenton et al., 2011; Kaplan et al., 2011; Ballantyne and Stone, 2012; Briner et al., 2012; Goehring et al., 2012; Blard et al., 2013; Young et al., 2013; Kelly et al., 2015; Lifton et al., 2015; Martin et al., 2015; Small and Fabel, 2015; Stroeven et al., 2015; Putnam et al., 2019). Heyman (2014), in contrast, includes all above post-2010 publications except Blard et al. (2013), Lifton et al. (2015), Martin et al.

(2015), Small and Fabel (2015), and Putnam et al. (2019) in calculation of his global ^{10}Be production rate. All post-2010 publications point to a spallogenic ^{10}Be production rate (*St*) of ~4 at/g/yr, in agreement with global, average SLHL $^{10}Be_{sp}$ production rates of Heyman (2014), Borchers et al. (2016), and Martin et al. (2017). At the time this paper was written, the CREp online calculator of Martin et al. (2017) reported world-wide mean SLHL total reference ^{10}Be production rates of 4.06 ± 0.38, 4.09 ± 0.38, and 4.11 ± 0.38 at/g/yr (2σ; *Lm* scaling), which vary as a function of the virtual dipole moment database used in calculation of scaling factors (Martin et al., 2017).

Only four production-rate determinations have been made for spallogenic ^{14}C in quartz. These rates range from 11.7 to 12.9 at/g/yr (Figure 7) and are based on radiocarbon ages at calibration sites ranging in age from 9.6 to 17.4 ka. All $^{14}C_{sp}$ values here are reported with 2σ uncertainty and *St* scaling. These four rates incorporate data from New Zealand (11.7±1.8 at/g/yr; Schimmelpfennig et al., 2012), along the Bonneville shoreline in Utah, USA (12.9±1.2 at/g/yr; Lifton et al., 2001; Pigati, 2004; Miller et al., 2006; Dugan, 2008; Dugan et al., 2008; Lifton et al., 2015), from two sample sites, Corrie nan Arr and Maol Chean-dearg, in the Highlands of northwestern Scotland (12.4±3.2 at/g/yr; Dugan et al., 2008), and from West Greenland (12.0±1.8 at/g/yr; Young et al., 2014). Borchers et al. (2016) also performed a statistical evaluation of ^{14}C production rates, and report a *St* scaled value of 12.24 at/g/yr, but again, this value does not include any ^{14}C production rates since 2010, thus excluding the two lower production rates of Schimmelpfennig et al. (2012) and Young et al. (2014). Furthermore, an AMS laboratory intercomparison study (Jull et al., 2015) points out that there is considerable variability within a small number of analyses of in-situ ^{14}C in quartz. Four

AMS laboratories (University of Arizona, Purdue University, ETH Zurich, and Lamont-Doherty Earth Observatory) participated in 23 separate measurements of the ^{14}C quartz reference material (sample A), and results varied by 5-10% between the four labs.

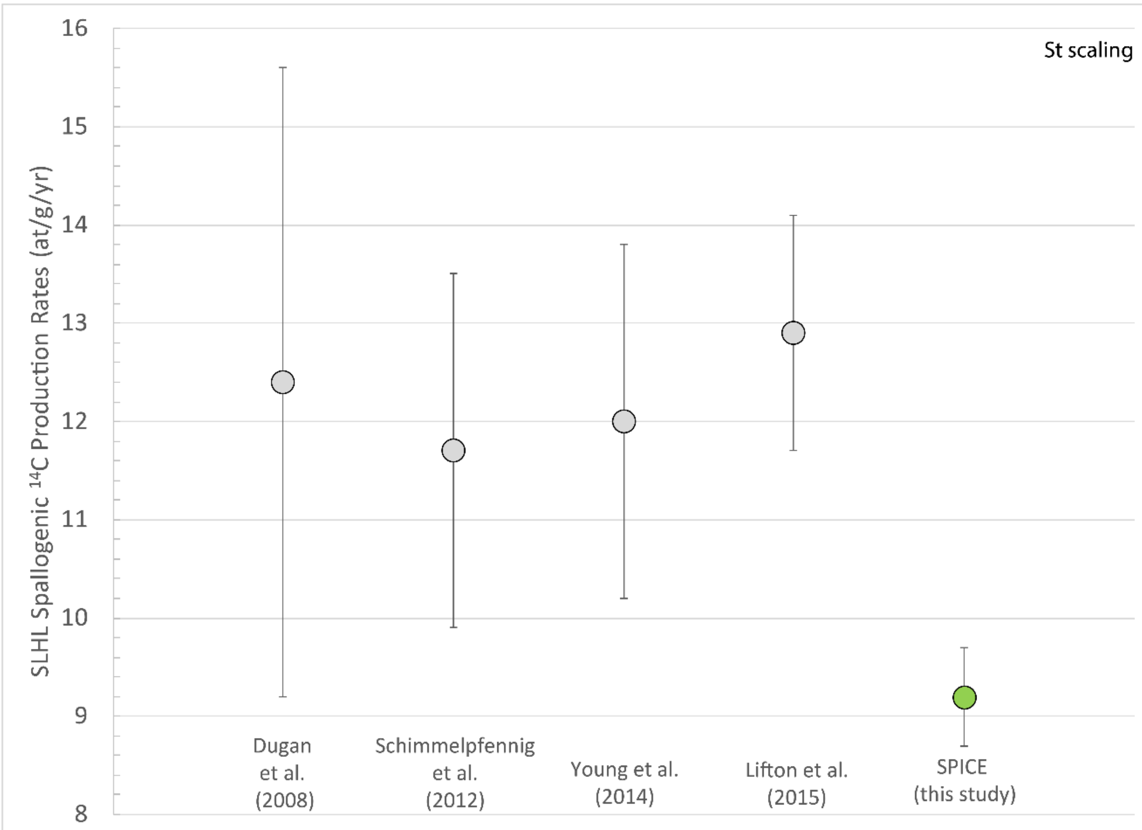

Figure 7. Comparison of published $^{14}C_{sp}$ production rates (gray circles) and the error-weighted mean spallogenic $^{14}C_{sp}$ production rate of the SPICE study (green circle) scaled with the *St* scaling method. Error bars represent 2σ uncertainty.

Only two of these ^{14}C studies determined accompanying $^{10}Be_{sp}$ production rates, and thus average spallogenic $^{14}C_{sp}/^{10}Be_{sp}$ values (Schimmelpfennig et al., 2012; Young et al., 2014). They are 3.0±0.4 and 3.1±0.4 (2σ, *St* scaling). Lifton et al. (2014) suggest the production-rate ratio of $^{14}C/^{10}Be$ may change as both a function of latitude and elevation, and thus the value of the ratio may vary from calibration site to calibration site. The $^{14}C/^{10}Be$ ratios could also be affected by the very different muon contributions to cosmogenic ^{14}C and ^{10}Be and, subsequently, by the different altitude-scaling effects on the spallation and muon-induced reactions producing each nuclide (Heisinger et al., 2002a; 2002b; Lupker et al., 2015). To the best of our knowledge, no spallogenic $^{21}Ne/^{14}C$ values have yet been published.

Table 2 lists spallogenic SLHL ^{21}Ne, ^{10}Be, and ^{14}C production rates of Borchers et al. (2016) scaled with the *St*, *Sf*, and *Sa* methods. These production rates are used in the online calculators of Marrero et al. (2016; CRONUSCalc) and Balco et al. (2008; version 3.0). No uncertainties are reported with the rates. Borchers et al. (2016) state they “cannot infer statistically justifiable production rate uncertainties from the fitting exercise."

5. Methods

5.1 SPICE sample collection, shielding corrections and quartz separation

Surface samples were collected from the SP lava during two field seasons. Samples 10SPC01, 10SPC06, and 10SPC07 were collected in 2010. Unfortunately, the collected masses of basalt were too low to extract enough quartz from these three samples for ^{21}Ne, ^{10}Be, and ^{14}C analysis. The concentration of quartz xenocrysts in the basalt is quite low (<2-3%; Rittenour et al., 2012). Thus, in 2015, between 19 and 31 kg of basalt were collected for samples SPICE-A1 through –A10 (Table 1). All samples were collected from the well-preserved surfaces of pressure ridges on the SP lava flow. Sample elevations ranged from 1778 m to 1876 m, and sample thicknesses ranged from 6 cm to 13 cm (Table 1). Corrections were made to production rates based on topographic shielding and self-shielding (i.e. sample thickness and/or dipping of a boulder surface) according to CosmoCalc (Vermeesch, 2007). A value of 2.3 was used for the exponent *m* in Equation 3 of Vermeesch (2007). Bulk whole-rock densities (2.05-2.45 g/cm^3) were measured and used in calculation of the sample thickness shielding factor (Table 1).

Whole-rock samples were crushed, washed, and sieved. The 90-125, 125-250, 250-500, 500-710 and 710-1000 µm grain size fractions were split into magnetic and non-magnetic fractions using a Frantz magnetic separator. The magnetic fraction concentrated olivine and pyroxene, and the non-magnetic fraction concentrated quartz xenocrysts, some feldspar, and secondary carbonate and zeolites. Diiodomethane (ρ~2.83 g/cm^3), a heavy liquid, was used to separate the mafic minerals from the magnetic fraction. Bromoform (ρ~2.64 g/cm^3) was used to isolate quartz grains from the quartz-bearing, non-magnetic fraction. Quartz xenocrysts sank through the bromoform, creating quartz concentrates (weighing between 5 and 12 g) that contained >75% quartz. Quartz concentrates were treated and purified according to procedures introduced by Kohl and Nishiizumi (1992). Details are in Appendix A.

5.2 Neon gas mass spectrometric analysis

Between 0.46 and 0.86 g of sample from the thirteen quartz samples (Tables 1 and SD1) were analyzed for cosmogenic ^{21}Ne content at the noble-gas laboratory at GeoForschungsZentrum (GFZ) Potsdam. Noble gases were extracted by stepwise heating (at 400, 800, and 1200°C, with an additional 600°C step for two samples) for 20 minutes each. In addition, aliquots of two samples (SPICE-A4 and –A8) were crushed in vacuo to check the isotopic composition of Ne released from fluid inclusions. Further details about the analytical procedures can be found in Niedermann et al. (1997) and in Appendix A.

5.3 Be extraction and AMS analysis

Around two grams of purified quartz was dissolved for each of samples SPICE-A1 to -A10 after being spiked with ca. 250 µg of a commercial beryllium solution (Scharlab, 1000 mg/l, density 1.02 g/cm^3) (Tables 1 and SD2). From four of the samples (SPICE-A3, -A4, -A6 and -A8) there was enough quartz extracted to allow duplicate measurements. Laboratory preparation of the purified quartz as AMS targets was undertaken in two batches of eight, each batch additionally containing two reagent blanks and a CoQtz-N quartz reference sample (Binnie et al., 2019). Target preparation chemistry was performed in the clean laboratory at the University of Cologne using the single-step column approach described by Binnie et al. (2015) and beryllium hydroxide was co-precipitated with Ag, according to Stone et al. (2004), for pressing into AMS targets. Targets for $^{26}Al/^{27}Al$ AMS analysis were similarly prepared by co-precipitation with Ag. Measurement of these targets is still pending.

Determinations of $^{10}Be/^{9}Be$ were undertaken at CologneAMS (Dewald et al., 2013), normalized to the revised standard values reported by Nishiizumi et al. (2007). Details can be found in the footnotes of table SD2. The nominal $^{10}Be/^{9}Be$ standard values of Nishiizumi et al. (2007) were determined independently of the ^{10}Be half-life but are consistent with the 1.387 Myr value measured by Chmeleff et al. (2010) and Korschinek et al. (2010). A ^{10}Be half-life of 1.387 Myr is used in ^{10}Be production-rate calculations in this study.

5.4 In-situ ^{14}C extraction and AMS mass spectrometer analysis

We extracted about 1 g quartz for each sample for ^{14}C analysis. The ^{14}C extraction followed the procedures described in Fülöp et al. (2015) using ^{14}C-dead $CaCO_3$ carrier material mass (carrier added equivalent to between 5 and 20 µg C equivalent). ^{14}C AMS measurements were conducted using the purified CO_2 gas and the gas source at CologneAMS (Stolz et al., 2017). Results are shown in Table SD3.

6. Results

6.1 Neon results

Results from neon analyses are listed in Table SD1. Crushing extractions of two quartz samples (SPICE-A4 and –A8) yielded isotopic compositions that are indistinguishable from air and indicate that Ne trapped in SP-flow quartz is atmospheric in composition ($^{22}Ne/^{20}Ne = 0.1020$, $^{21}Ne/^{20}Ne = 0.002959$; Eberhardt et al., 1965) (Figure 8). Furthermore, the Ne three-isotope diagram provides no indication for the presence of additional Ne components (e.g., nucleogenic Ne). All data points plot along the spallation line for quartz (Niedermann et al., 1993). Thus, the amount of cosmogenic ^{21}Ne in each heating step has been calculated according to the following equation:

$$^{21}Ne_{cosmogenic} = [(^{21}Ne/^{20}Ne)_{measured} - (^{21}Ne/^{20}Ne)_{atmospheric}] * {}^{20}Ne_{measured} \qquad \text{[Eq. 5].}$$

The "classical" atmospheric $^{21}Ne/^{20}Ne$ ratio of Eberhardt et al. (1965) used here is ~1.9% higher than a recent redetermination by Honda et al. (2015; 0.002905). If that value would be used, all ^{21}Ne excesses, as well as the production rates calculated from them, would decrease by 1.9% as well. This is well within uncertainties, and for the time being, we also chose to stay with the old value as to date the vast majority of cosmogenic Ne applications rely on it. Nevertheless, future work applying the Honda et al. (2015) atmospheric $^{21}Ne/^{20}Ne$ ratio should strictly use production rates reduced by 1.9%.

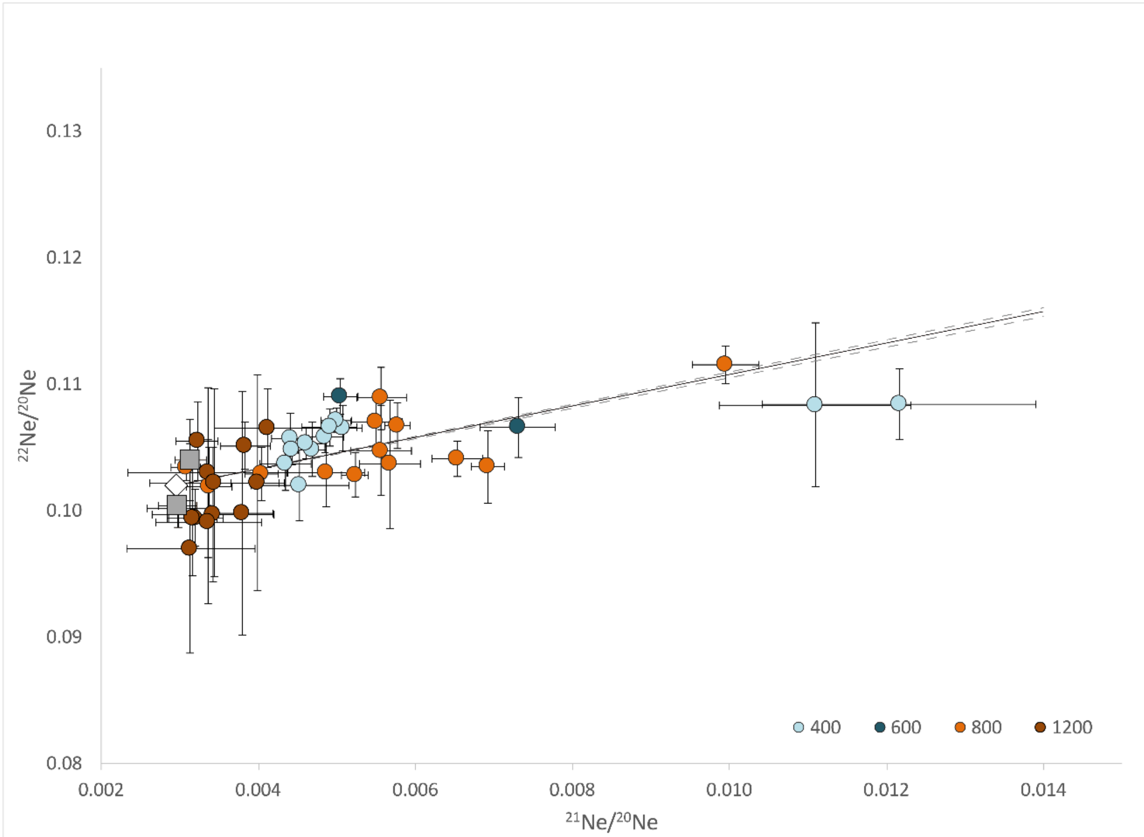

Figure 8. Neon three-isotope plot (after Niedermann et al., 1993). Measurements from all temperature steps (circles) are plotted on the graph, as are the two crush values (gray boxes). Atmospheric neon is represented by the white diamond. The dashed lines show the uncertainty range on the spallation line. Error bars represent 2σ uncertainty.

6.2 Cosmogenic ^{10}Be concentrations

AMS analysis of our SPICE samples yielded $^{10}Be/^{9}Be$ ratios ranging from 1.03×10^{-13} to 1.15×10^{-13} (Table SD2). Both batches of SPICE samples were processed in the laboratory alongside a pair of blanks and these gave measured $^{10}Be/^{9}Be$ values between 1.55×10^{-15} and 3.04×10^{-15}. The arithmetic mean ^{10}Be atoms in each blank pair was subtracted from the ^{10}Be atoms measured in the relevant SPICE sample, resulting in blank subtractions of between 1.7% and 2.2% of the total ^{10}Be atoms measured. ^{10}Be concentration measurements of the in-house quartz reference material, CoQtz-N from each batch were $(2.49 \pm 0.09) \times 10^6$ atoms/g and $(2.63 \pm 0.09) \times 10^6$ atoms/g, in relatively good agreement with the preliminary consensus value estimate for this material $(2.53 \pm 0.09) \times 10^6$ atoms/g at the 95% confidence limit, Binnie et al., 2019). In the case of duplicate samples (SPICE-A3, -A4, -A6 and -A8) the error weighted (pooled) mean ^{10}Be concentration was calculated following Ward and Wilson (1978) and used for the production rate determinations.

6.3 Cosmogenic ^{14}C concentrations

AMS analysis of our samples yielded $^{14}C/^{12}C$ ratios ranging from 0.7×10^{-12} to 1.1×10^{-12} (Table SD3). Process blanks (n = 10; HF-etched, synthetic hydrothermal quartz) prepared alongside the samples gave measured $^{14}C/^{12}C$ values between 5 and 20×10^{-14}. Concentrations of ^{14}C were calculated using the measured amount of carbon (from carrier + sample) released during extraction. Process blanks (n=10) contain $(51\pm15) \times 10^3$ atoms ^{14}C. Samples contain between 200 and 390×10^3 atoms ^{14}C (blank corrected), with a mean of $(323 \pm 46) \times 10^3$ atoms ^{14}C (n=11).

6.4 Calculations of local production rates and production-rate ratios

Two determination methods are used to calculate cosmogenic nuclide production rates over time at the SP flow. Production rates of cosmogenic ^{21}Ne and ^{10}Be are directly calibrated and are based the independent $^{40}Ar/^{39}Ar$ eruption age of the SP flow (72±4 ka; 2σ; Fenton et al., 2013) (Tables 3 and 4). The production rate of ^{14}C is based on the assumption that quartz in the SP flow surface is saturated with respect to ^{14}C. The half-life of ^{14}C is very short compared to the eruption age and exposure history of the SP flow and the nuclide has reached secular equilibrium. Radioactive nuclide saturation (>95%) occurs around 4.5 half-lives, which equates to 25 ka. Thus, the production rates (P_0) of ^{14}C at the SP flow are calculated by rearranging Equation 3, such that $P_0 = \lambda C(t)$, where λ is the ^{14}C decay constant ($\lambda = \ln 2/T_{½}$, with $T_{½}$ = 5730±40 yr) (Table 5).

Tables SD1, SD2, and SD3 list cosmogenic nuclide concentrations in terms of ^{21}Ne atoms/g quartz, ^{10}Be atoms/g quartz, and ^{14}C atoms/g quartz. These values are then corrected for topographic and self-shielding (including sample thickness and variations in whole-rock density). Corrected, local production rates are calculated and listed in Tables 3, 4, 5, 6, and Figure 9.

Each local production rate includes total production of a cosmogenic nuclide (spallation production + muon production) at each sample site and excludes use of scaling factors. Thus, these local production rates are latitude, longitude, and elevation specific. Local production rates for ^{21}Ne range from 52.8 to 64.2 at/g/yr and agree within 2σ uncertainty. Local production rates for ^{10}Be are 12.7-13.8 at/g/yr and agree within 1σ uncertainty. Local ^{14}C production rates are 26.7-52.3 at/g/yr, and aside from samples –A7 and –A9 agree within 2σ uncertainty. As such, samples SPICE-A7 and –A9 are considered outliers for ^{14}C data (Figure 9).

Table SD5 lists production-rate ratios for $^{21}Ne/^{10}Be$, $^{21}Ne/^{14}C$, and $^{14}C/^{10}Be$ based on the local production rates of each cosmogenic nuclide, which are not yet scaled and therefore independent of scaling models. Error-weighted means (±2σ uncertainty) of 4.44 ± 0.32, 1.43± 0.10, and 2.85 ± 0.21 are calculated for $^{21}Ne/^{10}Be$, $^{21}Ne/^{14}C$, and $^{14}C/^{10}Be$, respectively. Uncertainties include those related to measurements, corrections for shielding, the $^{40}Ar/^{39}Ar$ age, and the ^{14}C half-life (where applicable). SP-flow quartz has $^{21}Ne/^{10}Be$ and $^{14}C/^{10}Be$ values that agree with previously published production-rate ratios within 2σ uncertainty (see section 4). Production-rate ratios using SLHL production rates from spallation are also listed in Table SD5. These values are very similar to ratios based solely on local production rates, and agree well with reported ratios in the literature.

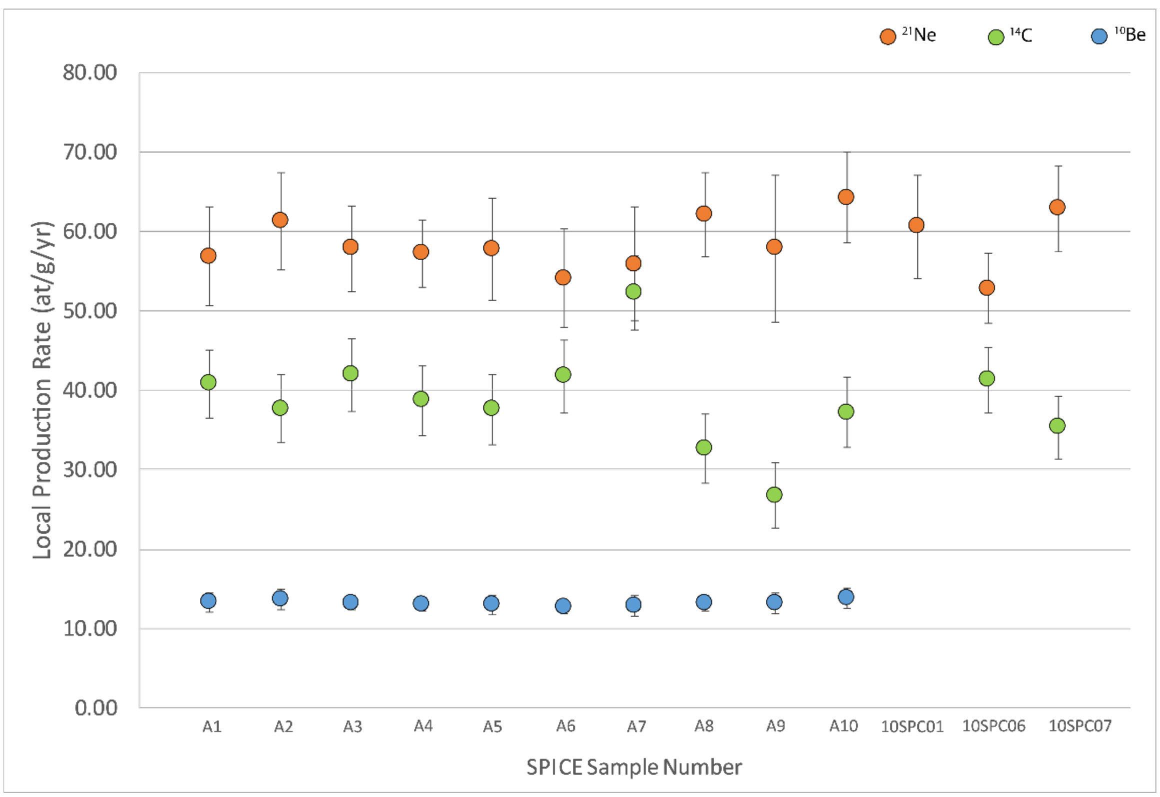

Figure 9. Local ^{21}Ne, ^{10}Be, and ^{14}C production rates for samples SPICE-A1 to –A10, and 10SPC01, -06, and -07. These rates are not scaled to SLHL. Error bars represent 2σ

uncertainty, and do not include the uncertainty associated with the $^{40}Ar/^{39}Ar$ age of the SP lava flow or the ^{14}C half life.

Table 3. Total reference SLHL ^{21}Ne production rates for SPICE quartz samples.

Sample ID	Total cosmogenic ^{21}Ne concentration (10^6 at/g) [a]	2σ uncertainty (10^6 at/g) [a]	Total ^{21}Ne production rate at local sampling elevation (at/g/yr) [b]	2σ uncertainty (at/g/yr) [b]	Total reference ^{21}Ne production rate at SLHL (*St*-scaled) (at/g/yr) [c]	2σ uncertainty (at/g/yr) [c]	Total reference ^{21}Ne production rate at SLHL (*Sf*-scaled) (at/g/yr) [c]	2σ uncertainty (at/g/yr) [c]
SPICE-A1	4.09	0.45	56.8	6.2	16.2	1.8	14.7	1.6
SPICE-A2	4.41	0.44	61.3	6.2	17.8	1.8	16.2	1.6
SPICE-A3	4.17	0.39	57.9	5.4	16.8	1.6	15.3	1.4
SPICE-A4	4.12	0.31	57.2	4.3	16.7	1.2	15.2	1.1
SPICE-A5	4.16	0.46	57.7	6.4	16.8	1.9	15.4	1.7
SPICE-A6	3.90	0.45	54.1	6.2	16.0	1.8	14.6	1.7
SPICE-A7	4.02	0.52	55.9	7.2	16.3	2.1	14.9	1.9
SPICE-A8	4.47	0.39	62.1	5.4	18.4	1.6	16.8	1.5
SPICE-A9	4.17	0.66	57.9	9.2	16.8	2.7	15.3	2.4
SPICE-A10	4.62	0.41	64.2	5.7	18.7	1.7	17.1	1.5
10SPC01	4.36	0.47	60.6	6.5	16.8	1.8	15.2	1.6
10SPC06	3.80	0.31	52.8	4.4	15.4	1.3	14.1	1.2
10SPC07	4.52	0.39	62.8	5.4	18.5	1.6	16.9	1.4
					Average	**17.0 ± 1.1** [d]	**Average**	**15.5 ± 1.0** [d]

Note: Table SD1 contains the raw data from mass spectrometer analysis of SP-flow quartz. Scaling factors are listed in Table SD4.

[a] Total concentrations of ^{21}Ne are corrected for total shielding. Uncertainties include the analytical uncertainty of mass spectrometer measurements and uncertainty related to total shielding (2.8%).

[b] Local production rates are calculated by dividing the total cosmogenic ^{21}Ne concentrations by 72 ka. Uncertainties do not include the uncertainty on the $^{40}Ar/^{39}Ar$ age.

[c] Total reference SLHL ^{21}Ne production rates are derived by scaling them to sea-level, high latitude using *St* and *Sf* scaling factors (Table SD4). The scaling factors are determined using CRONUSCalc (Marrero et al., 2016). Uncertainties do not include the uncertainty on the $^{40}Ar/^{39}Ar$ age.

[d] This is an error-weighted mean of all thirteen samples. The 2σ uncertainty includes the uncertainty on the $^{40}Ar/^{39}Ar$ age.

Table 4. Muogenic portions, spallogenic portions, and total reference SLHL ^{10}Be production rates for SPICE quartz samples.

Sample ID	Total cosmogenic ^{10}Be concentration (10^5 at/g) [a]	2σ uncertainty (10^5 at/g) [a]	Total ^{10}Be production rate at local sampling elevation (at/g/yr) [b]	2σ uncertainty (at/g/yr) [b]	^{10}Be production rate from negative muon capture at local sampling elevation (at/g/yr) [c]	2σ uncertainty (at/g/yr) [c]	Spallogenic ^{10}Be production rate at SLHL (*St*-scaled) (at/g/yr) [d,e]	2σ uncertainty (at/g/yr)	Muogenic ^{10}Be production rate at SLHL (*St*-scaled) (at/g/yr) [e]	2σ uncertainty (at/g/yr)	Total reference ^{10}Be production rate at SLHL (*St*-scaled) (at/g/yr)	2σ uncertainty (at/g/yr)
SPICE-A1	9.38	0.86	13.3	1.2	0.191	0.046	3.67	0.49	0.10	0.02	3.77	0.49
SPICE-A2	9.64	0.94	13.6	1.3	0.189	0.045	3.85	0.54	0.10	0.02	3.96	0.54
SPICE-A3	9.36	0.87	13.2	1.2	0.188	0.045	3.73	0.50	0.10	0.02	3.83	0.50
SPICE-A4	9.25	0.88	13.1	1.2	0.188	0.045	3.71	0.51	0.10	0.02	3.81	0.51
SPICE-A5	9.17	0.87	13.0	1.2	0.187	0.045	3.68	0.51	0.10	0.02	3.78	0.51
SPICE-A6	9.01	0.87	12.7	1.2	0.186	0.044	3.67	0.51	0.10	0.02	3.77	0.51
SPICE-A7	9.09	0.87	12.9	1.2	0.187	0.045	3.64	0.51	0.10	0.02	3.75	0.51
SPICE-A8	9.36	0.90	13.2	1.3	0.186	0.044	3.81	0.53	0.10	0.02	3.91	0.53
SPICE-A9	9.31	0.89	13.2	1.3	0.188	0.045	3.71	0.51	0.10	0.02	3.81	0.51
SPICE-A10	9.75	0.92	13.8	1.3	0.187	0.045	3.92	0.53	0.10	0.02	4.02	0.53
						Average [f]	**3.73**	**0.26**	**0.10**	**0.01**	**3.84**	**0.27**

Table 4.(continued). Scaled with *Sf* and *Sa* scaling factors

Sample ID	Spallogenic ^{10}Be production rate at SLHL (*Sf*-scaled) (at/g/yr) [d]	2σ uncertainty (at/g/yr)	Muogenic ^{10}Be production rate at SLHL (*Sf*-scaled) (at/g/yr) [e]	2σ uncertainty (at/g/yr)	Total reference ^{10}Be production rate at SLHL (*Sf*-scaled) (at/g/yr) [e,]	2σ uncertainty (at/g/yr)	Spallogenic ^{10}Be production rate at SLHL (*Sa*-scaled) (at/g/yr) [d,e]	2σ uncertainty (at/g/yr)	Muogenic ^{10}Be production rate at SLHL (*Sa*-scaled) (at/g/yr) [e]	2σ uncertainty (at/g/yr)	Total reference ^{10}Be production rate at SLHL (*Sa*-scaled) (at/g/yr)	2σ uncertainty (at/g/yr)
SPICE-A1	3.36	0.45	0.07	0.02	3.43	0.45	3.23	0.43	0.07	0.02	3.30	0.43
SPICE-A2	3.54	0.50	0.07	0.02	3.61	0.50	3.40	0.48	0.07	0.02	3.47	0.48
SPICE-A3	3.42	0.46	0.07	0.02	3.50	0.34	3.29	0.44	0.07	0.02	3.36	0.44
SPICE-A4	3.40	0.47	0.07	0.02	3.47	0.35	3.27	0.45	0.07	0.02	3.34	0.45
SPICE-A5	3.38	0.47	0.07	0.02	3.45	0.47	3.25	0.45	0.07	0.02	3.32	0.45
SPICE-A6	3.37	0.47	0.07	0.02	3.45	0.35	3.24	0.45	0.07	0.02	3.31	0.45
SPICE-A7	3.35	0.47	0.07	0.02	3.42	0.47	3.22	0.45	0.07	0.02	3.29	0.45
SPICE-A8	3.50	0.49	0.07	0.02	3.58	0.36	3.37	0.47	0.07	0.02	3.44	0.47
SPICE-A9	3.41	0.47	0.07	0.02	3.48	0.47	3.27	0.45	0.07	0.02	3.34	0.45
SPICE-A10	3.60	0.49	0.07	0.02	3.67	0.49	3.45	0.47	0.07	0.02	3.52	0.47
Average [f]	**3.43**	**0.24**	**0.07**	**0.01**	**3.50**	**0.25**	**3.30**	**0.23**	**0.07**	**0.01**	**3.36**	**0.24**

[a] Total concentrations of ^{10}Be are corrected for total shielding. Uncertainties include the uncertainty of AMS measurements and uncertainty related to total shielding (2.8%).

[b] Local production rates are calculated by dividing the total cosmogenic ^{10}Be concentrations by 72 ka. Uncertainties do not include the uncertainty on the ^{40}Ar/^{39}Ar age. Total ^{10}Be concentrations are corrected for decay using the ^{10}Be half-life of 1.387 Myr (Chmeleff et al., 2010; Korschinek et al., 2010).

[c] Production of ^{10}Be from negative muon capture corrected for sample thickness and scaled for elevation, according to Heisinger et al. (2002a) and Lal (1991)/Stone (2000), respectively; muogenic production rates determined here are independent of the calibration sample measurements, and only rely on literature values.Scaling factors are listed in Table SD4. Uncertainty includes 7% and 10% relative uncertainties on the production rates from negative muon capture and on scaling factors for negative muon capture (Heisinger et al., 2002a; 2002b).

[d] The spallogenic ^{10}Be production rates are derived by (1) subtracting the ^{10}Be production rates resulting from negative muon capture from the total ^{10}Be production rate at the corresponding sample elevation for each sample, and then (2) scaling the resultant spallogenic ^{10}Be production rate to SLHL. The spallation production rate includes the production from fast-muon induced spallation, following Lal(1991)/Stone (2000) and Dunai (2000). Uncertainty includes the uncertainty related to negative muon capture (column 7), as well as 14% relative uncertainty on production rates from fast muon induced spallation (Heisinger et al., 2002a; 2002b) and uncertainty associated with total cosmogenic ^{10}Be concentrations (column 3).

[e] SLHL production rates are derived by scaling them to sea-level, high latitude using *St*, *Sf* and *Sa* scaling factors (Table SD4). The scaling factors are determined using CRONUSCalc (Marrero et al., 2016). Uncertainties do not include the uncertainty on the ^{40}Ar/^{39}Ar age.

[f] This is an error-weighted mean of all ten samples. The 2σ uncertainty is the standard error on the mean and includes the uncertainty on the $^{40}Ar/^{39}Ar$ age.

Table 5. Muogenic portions, spallogenic portions, and total reference SLHL ^{14}C production rates for SPICE quartz samples.

Sample ID	Total cosmogenic ^{14}C concentration (10^5 at/g) [a]	2σ uncertainty (10^5 at/g) [a]	Total ^{14}C production rate at local sampling elevation (at/g/yr) [b]	2σ uncertainty (at/g/yr) [b]	^{14}C production rate from negative muon capture at local sampling elevation (at/g/yr) [c]	2σ uncertainty (at/g/yr) [c]	Spallogenic ^{14}C production rate at SLHL (*St*-scaled) (at/g/yr) [d,e]	2σ uncertainty (at/g/yr)	Muogenic ^{14}C production rate at SLHL (*St*-scaled) (at/g/yr) [e]	2σ uncertainty (at/g/yr)	Total reference ^{14}C production rate at SLHL (*St*-scaled) (at/g/yr)	2σ uncertainty (at/g/yr)
SPICE-A1	3.37	0.36	40.8	4.3	6.1	1.5	9.6	1.8	1.97	0.47	11.6	1.9
SPICE-A2	3.12	0.35	37.7	4.3	6.0	1.4	9.0	1.8	1.98	0.47	10.9	1.9
SPICE-A3	3.47	0.38	42.0	4.6	6.0	1.4	10.2	1.9	1.97	0.47	12.2	2.0
SPICE-A4	3.20	0.37	38.7	4.4	6.0	1.4	9.3	1.9	1.97	0.47	11.3	2.0
SPICE-A5	3.11	0.37	37.6	4.4	6.0	1.4	9.0	1.9	1.97	0.47	11.0	1.9
SPICE-A6	3.45	0.38	41.8	4.6	5.9	1.4	10.4	2.0	1.98	0.48	12.4	2.0
SPICE-A7	4.32	0.39	52.3	4.7	6.0	1.4	13.3	2.0	1.97	0.47	15.2	2.0
SPICE-A8	2.70	0.36	32.7	4.3	5.9	1.4	7.7	1.9	1.98	0.48	9.7	1.9
SPICE-A9	2.21	0.34	26.7	4.1	6.0	1.4	5.8	1.8	1.97	0.47	7.7	1.8
SPICE-A10	3.07	0.37	37.2	4.4	6.0	1.4	8.9	1.9	1.97	0.47	10.8	2.0
10SPC06	3.41	0.34	41.3	4.1	6.0	1.4	10.1	1.8	1.98	0.48	12.1	1.8
10SPC07	2.92	0.33	35.3	4.0	6.0	1.4	8.4	1.7	1.99	0.48	10.4	1.8
						Average [f]	**9.2**	**0.5**	**1.97**	**0.3**	**11.2**	**0.6**

Table 5. (continued). Scaled with *Sf* and *Sa* scaling factors

Sample ID	Spallogenic ^{14}C production rate at SLHL (*Sf*-scaled) (at/g/yr) [d]	2σ uncertainty (at/g/yr)	Muogenic ^{14}C production rate at SLHL (*Sf*-scaled) (at/g/yr) [e]	2σ uncertainty (at/g/yr)	Total reference ^{14}C production rate at SLHL (*Sf*-scaled) (at/g/yr) [e]	2σ uncertainty (at/g/yr)	Spallogenic ^{14}C production rate at SLHL (*Sa*-scaled) (at/g/yr) [d,e]	2σ uncertainty (at/g/yr)	Muogenic ^{14}C production rate at SLHL (*Sa*-scaled) (at/g/yr) [e]	2σ uncertainty (at/g/yr)	Total reference ^{14}C production rate at SLHL (*Sa*-scaled) (at/g/yr)	2σ uncertainty (at/g/yr)
SPICE-A1	9.9	1.7	1.44	0.35	11.3	1.8	9.9	1.7	1.45	0.35	11.4	1.8
SPICE-A2	9.2	1.8	1.46	0.35	10.7	1.8	9.3	1.8	1.47	0.35	10.8	1.8
SPICE-A3	10.4	1.9	1.46	0.35	11.9	1.9	10.5	1.9	1.46	0.35	11.9	1.9
SPICE-A4	9.5	1.8	1.46	0.35	11.0	1.9	9.6	1.8	1.47	0.35	11.1	1.9
SPICE-A5	9.3	1.8	1.46	0.35	10.7	1.9	9.3	1.8	1.47	0.35	10.8	1.9
SPICE-A6	10.6	1.9	1.48	0.35	12.1	2.0	10.7	1.9	1.49	0.36	12.2	2.0
SPICE-A7	13.4	1.9	1.46	0.35	14.9	2.0	13.5	1.9	1.47	0.35	15.0	2.0
SPICE-A8	8.0	1.8	1.48	0.35	9.5	1.9	8.0	1.8	1.49	0.36	9.5	1.9
SPICE-A9	6.1	1.7	1.46	0.35	7.6	1.7	6.1	1.7	1.46	0.35	7.6	1.7
SPICE-A10	9.1	1.8	1.46	0.35	10.6	1.9	9.2	1.8	1.47	0.35	10.7	1.9
10SPC06	10.3	1.7	1.47	0.35	11.8	1.7	10.4	1.7	1.48	0.35	11.9	1.7
10SPC07	8.7	1.6	1.47	0.33	10.2	1.7	8.7	1.6	1.49	0.36	10.2	1.7
Average [f]	**9.5**	**0.5 [c]**	**1.46**	**0.10**	**10.9**	**0.5**	**9.5**	**0.6 [c]**	**1.47**	**0.10**	**11.0**	**0.5**

[a] Total concentrations of ^{14}C are corrected for total shielding. Uncertainties include the uncertainty of AMS measurements and uncertainty related to total shielding (2.8%).

[b] Local production rates are calculated by multiplying the total cosmogenic ^{14}C concentration in a sample ($C(t)$) by the decay constant for ^{14}C. Uncertainties do not include the uncertainty on of the radiocarbon decay constant.

[c] Production of ^{14}C from negative muon capture corrected for sample thickness and scaled for elevation, according to Heisinger et al. (2002a) and Lal (1991)/Stone (2000), respectively; muogenic production rates determined here are independent of the calibration sample measurements, and only rely on literature values. Scaling factors are listed in Table SD4. Uncertainty includes 7% and 10% relative uncertainties on the production rates from negative muon capture and on scaling factors for negative muon capture (Heisinger et al., 2002a; 2002b).

[d] The spallogenic ^{14}C production rates are derived by (1) subtracting the ^{14}C production rates resulting from negative muon capture from the total ^{14}C production rate at the corresponding sample elevation for each sample, and then (2) scaling the resultant spallogenic ^{14}C production rate to SLHL. The spallation production rate includes the production from fast-muon induced spallation, following Lal(1991)/Stone (2000) and Dunai (2000). Uncertainty includes the uncertainty related

to negative muon capture (column 7), as well as 57% relative uncertainty on production rates from fast muon induced spallation (Heisinger et al., 2002a; 2002b) and uncertainty associated with total cosmogenic ^{14}C concentrations (column 3).

[e] SLHL production rates are derived by scaling them to sea-level, high latitude using *St*, *Sf*, and *Sa* scaling factors (Table SD4). The scaling factors are determined using CRONUSCalc (Marrero et al., 2016). Uncertainties do not include the uncertainty on the ^{14}C decay constant.

[f] This is an error-weighted mean of all twelve samples. The 2σ uncertainty is the standard error on the mean and includes the uncertainty on the radiocarbon decay constant (0.7%).

Table 6. Total reference SLHL ^{10}Be production rates for SPICE quartz samples (*Lm*-scaled) calculated with three virtual dipole moment (VDM) databases in the CREp online calculator (https://crep.otelo.univ-lorraine.fr/#/init; Martin et al., 2017).

Sample ID	Total cosmogenic ^{10}Be concentration (10^5 at/g) [a]	2σ uncertainty (10^5 at/g) [a]	VDM 1 Integrated *Lm* scaling factor (sample-site specific)	**VDM 1 Atmospheric ^{10}Be-based VDM** [b] total reference ^{10}Be production rate at SLHL (at/g/yr)	2σ uncertainty (at/g/yr)	VDM 2 Integrated *Lm* scaling factor (sample-site specific)	**VDM 2 Lifton VDM 2016** [c] total reference ^{10}Be production rate at SLHL (at/g/yr)	2σ uncertainty (at/g/yr)	VDM 3 Integrated *Lm* scaling factor (sample-site specific)	**VDM 3 LSD Framework** [d] total reference ^{10}Be production rate at SLHL (at/g/yr)	2σ uncertainty (at/g/yr)
SPICE-A1	9.38	0.86	3.600	3.68	0.40	3.651	3.63	0.40	3.865	3.43	0.36
SPICE-A2	9.64	0.94	3.532	3.86	0.44	3.578	3.81	0.42	3.786	3.6	0.40
SPICE-A3	9.36	0.87	3.540	3.73	0.40	3.585	3.69	0.40	3.794	3.48	0.38
SPICE-A4	9.25	0.88	3.523	3.71	0.42	3.568	3.66	0.40	3.776	3.46	0.38
SPICE-A5	9.17	0.87	3.516	3.68	0.40	3.561	3.64	0.40	3.769	3.44	0.38
SPICE-A6	9.01	0.87	3.464	3.68	0.42	3.508	3.63	0.40	3.712	3.43	0.38
SPICE-A7	9.09	0.87	3.516	3.65	0.40	3.561	3.61	0.40	3.769	3.41	0.38
SPICE-A8	9.36	0.90	3.464	3.81	0.42	3.509	3.77	0.42	3.713	3.56	0.40
SPICE-A9	9.31	0.89	3.540	3.72	0.42	3.585	3.67	0.40	3.794	3.47	0.38
SPICE-A10	9.75	0.92	3.516	3.92	0.42	3.561	3.87	0.42	3.769	3.65	0.40
Average [e]				**3.74**	**0.25**		**3.69**	**0.24**		**3.49**	**0.23**

Note: Scaling factors that account for time-dependent variations in geomagnetic field strength were calculated using three different Virtual Dipole Moment (VDM) databases within the CREp calculator. ERA40 atmospheric model of Uppala et al. (2005) was used with each VDM database.

[a] Total concentrations of ^{10}Be are corrected for total shielding. Uncertainties include the uncertainty of AMS measurements and uncertainty related to total shielding (2.8%).

[b] VDM 1 is the database based on Muscheler et al. (2005) and Valet et al. (2005).

[c] VDM 2 is the database based on Laj et al. (2004), Ziegler et al. (2011), Pavón-Carrasco et al. (2014), and Lifton (2016).

[d] VDM 3 is the database based on Lifton et al. (2014).

[e] This is an error-weighted mean of all ten samples. The 2σ uncertainty includes the uncertainty on the ^{40}Ar/^{39}Ar age.

6.5 Scaling methods and SLHL production rates

Scaling factors are used to calculate total SLHL reference production rates, spallation production rates, and muon-induced production rates for ^{21}Ne, ^{10}Be, and ^{14}C in SPICE quartz samples. *St*, *Sf*, *Sa*, and *Lm* scaling models are employed to scale cosmogenic nuclide data (Tables 3, 4, 5, 6, and SD4). *St* scaling factors are calculated using the CRONUSCalc online calculator (Marrero et al., 2016). *Sf* and *Sa* scaling factors were calculated in Matlab using the mmc1 code of Lifton et al. (2014). *Lm* scaling factors are calculated for ^{10}Be within the CREp online calculator and final integrated values for each sample are reported (Table 6). Individual *Lm* scaling factors for each time step, such as those produced from the mmc1 code (Lifton et al., 2014), are not reported for ^{10}Be calculations. CREp does not yet provide capabilities for calculating cosmogenic ^{21}Ne or ^{14}C production rates or exposure ages.

Time-dependent *Sf* and *Sa* scaling factors are integrated over 72 ka for ^{21}Ne and ^{10}Be production rates, and over 25 ka for ^{14}C production rates. The mmc1 code of Lifton et al. (2014) does yet not provide the possibility of calculating *Sa* scaling factors for ^{21}Ne. *Sf* and *Sa* scaling factors are also integrated over 8270 a (Table SD4), which is the integration time (t_{int}) of Blard et al. (2019; based on equation 7 therein) for in-situ ^{14}C. Integration time is equal to $1/\lambda$ (Blard et al., 2019), when the exposure time of a surface, such as the SP lava flow (72 ka), is much greater than the half-life of the cosmogenic nuclide (5730 a for ^{14}C); many of the ^{14}C atoms produced in the first 25 ka of exposure at the SP flow have decayed.

To illustrate numerical differences between time-dependent scaling factors calculated with various scaling methods, *Sf*, *Sa*, and *Lm* scaling factors for ^{10}Be at the SPICE-A1 site are compared with the time independent St scaling factor calculated for the same SPICE-A1 site. The SP lava flow surface has been exposed to cosmic rays for the past 72 ka, which includes a proposed period of higher cosmic-ray flux between 20 and 50 ka, when the Earth's magnetic field was weaker than it is now (Figure 10; Lifton et al., 2014). *Sf* and *Sa* scaling factors calculated for ^{10}Be at the SPICE-A1 site are 3.861 and 4.021, respectively (Table SD4). In contrast, *Sf* and *Sa* factors averaged over only the past 20 ka at the SPICE-A1 site are 3.499 and 3.363, respectively. The 72-ka-averaged factors are significantly higher than the 20-ka-averaged factors. In addition, the 20-ka-averaged *Sf* and *Sa* factors are only 0.5% lower and 3.4% higher than the constant *St* factor (3.515) at the SPICE-A1 site, whereas the 72-ka-averaged *Sf* and *Sa* factors are 9.9% and 14.4% higher than the *St* factor. This is because the *Sf* and *Sa* factors account for the proposed weak geomagnetic field between 20 and 50 ka (Lifton et al., 2014) (Figure 10).

Lm scaling factors calculated for ^{10}Be at the SPICE-A1 site are averaged over the past 72 ka, and are 3.600, 3.651, and 3.865 for VDM 1, VDM 2, and VDM 3, respectively (Table 6). These factors are 2.4 – 9.9% greater than the *St* scaling factor for sample SPICE-A1 (3.515). Each of the three VDM models corrects for geomagnetic field strength, but the correction is greatest for VDM 3 (the LSD Framework; Lifton et al., 2014). *Lm* scaling factors calculated within the VDM 1 and VDM 2 models are only 2.4% and 3.8% higher than the *St* scaling factor for sample SPICE-A1 (3.515). *Lm*-scaled SLHL production rates at the SP flow and based on VDM 1 and VDM 2 are thus less than *St*-scaled SLHL production rates, but greater than SLHL production rates scaled with *Lm* (VDM 3), *Sf*, or *Sa* scaling factors.

Ten samples (SPICE-A1 to -A10) are used in the calculations of all SLHL ^{21}Ne, ^{10}Be, and ^{14}C production rates. In addition, ^{21}Ne production rates include data from samples 10SPC01, 10SPC06, and 10SPC07, and ^{14}C production rates include data from samples 10SPC06 and 10SPC07 (Figures 11, 12, 13, 14 and 15). All uncertainties are reported as 2σ unless otherwise noted.

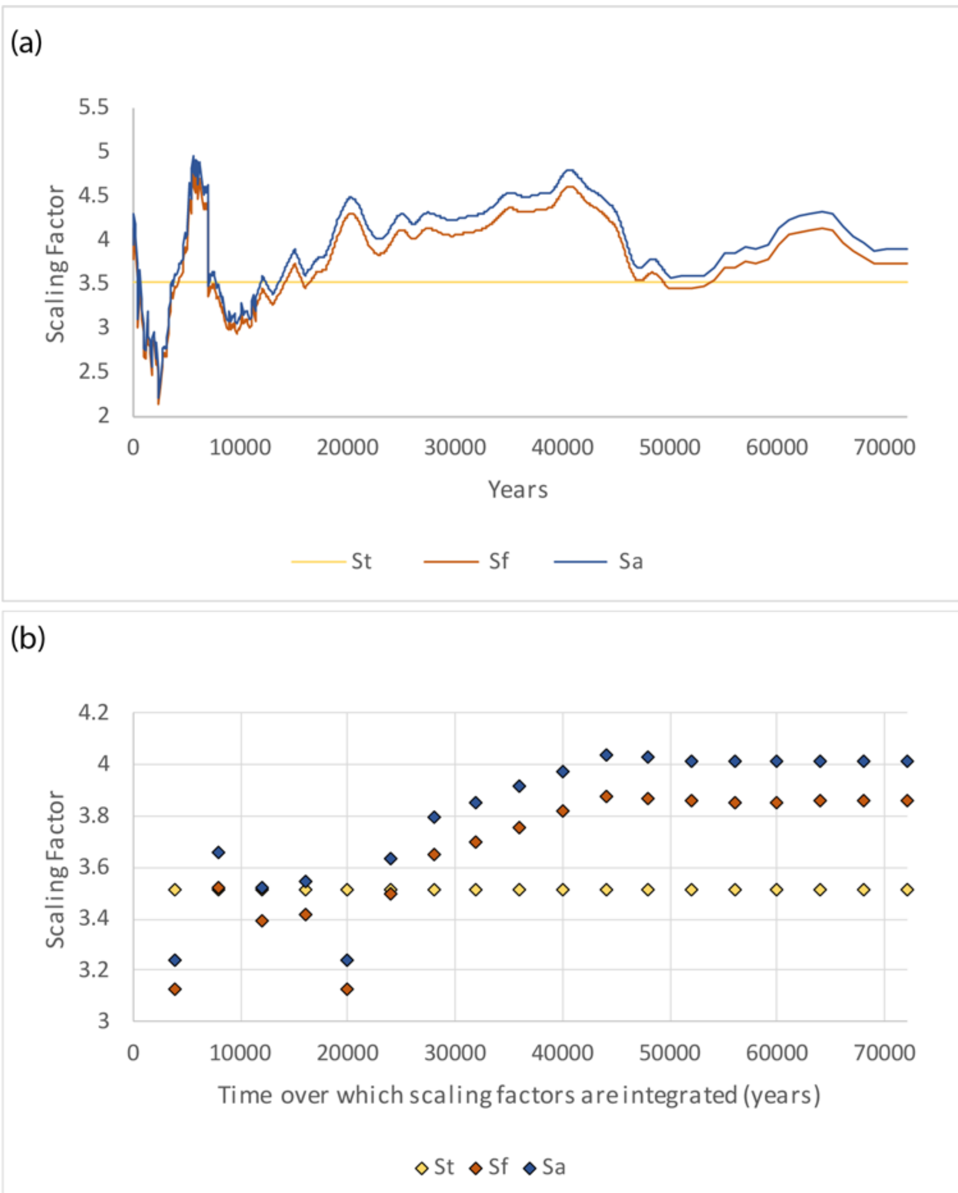

Figure 10. Time-independent *St* and time-dependent *Sf* and *Sa* scaling factors for ^{10}Be at the SPICE-A1 sample site (a) calculated for a point in time, and (b) averaged over a period of time.

6.5.1 Total reference SLHL production rates

Total reference SLHL production rates sum spallogenic and muogenic contributions to production rates for each nuclide (see footnotes Tables 3, 4, and 5). Using time-independent *St* scaling factors yields error-weighted mean total reference SLHL production rates for ^{21}Ne (n=13), ^{10}Be (n=10), and ^{14}C (n=12) of 17.0 ± 1.1 at/g/yr, 3.84 ± 0.27 at/g/yr, and 11.2 ± 0.6 at/g/yr, respectively. Using the time-dependent *Sf* scaling method decreases these SLHL values to 15.5 ± 1.0 at/g/yr, 3.50 ± 0.25 at/g/yr, and 10.9 ± 0.5 at/g/yr, respectively. Similarly, the nuclide-specific, time-dependent *Sa* scaling factors modify the SLHL values to 3.36 ± 0.24 at/g/yr and 11.0 ± 0.5 at/g/yr for ^{10}Be and ^{14}C, respectively (Tables 3, 4, and 5).

Total reference SLHL ^{10}Be production rates are also calculated using the CREp online calculator (Martin et al., 2017; https://crep.otelo.univ-lorraine.fr/#/init). The CREp calculator does not yet have the capability to calculate ^{21}Ne or ^{14}C production rates or exposure ages. CREp produces error-weighted mean total reference SLHL production rates (*Lm*) for ^{10}Be (n=10) of 3.74 ± 0.25, 3.69 ± 0.24, and 3.49 ± 0.23 at/g/yr (2σ; Tables 6 and 8) for VDM 1, VDM 2, and VDM 3 databases, respectively (Figure 11). The two highest mean production rates were determined using the VDM1 and VDM2 (Muscheler et al., 2005; Valet et al., 2005; Lifton, 2016). Both of these rates overlap the *Lm*-scaled world-wide mean total reference SLHL ^{10}Be production rate (4.11 ± 0.38 at/g/yr; VDM 1) within 2σ uncertainty (Table 8; Figure 11). The lowest value (3.49 ± 0.23 at/g/yr) was determined using the VDM 3 database (Lifton et al., 2014) and is essentially identical to the mean *Sf*-scaled total reference SLHL ^{10}Be production rate calculated in this study (3.50 ± 0.25 at/g/yr; Table 4). The lowest production rate (VDM 3-based) does not overlap the *Lm*-scaled world-wide mean total reference SLHL ^{10}Be production rate within uncertainty.

Both error-weighted mean total reference SLHL ^{21}Ne production rates (with *St* and *Sf* scaling) agree within 2σ uncertainty (Figure 13). The *Sf*-scaled total reference SLHL ^{10}Be production rate overlaps both *St*-scaled and *Sa*-scaled ^{10}Be production rates within 2σ uncertainty, however the *Sa*-scaled total reference SLHL ^{10}Be production rate is notably lower than the *St*-scaled total reference SLHL ^{10}Be production rate. The former and the latter do not overlap within 2σ uncertainty. All three *Lm*-scaled production rates overlap the *St*-scaled error-weighted mean total reference SLHL production rates for ^{10}Be (3.84 ± 0.27 at/g/yr) within 2σ uncertainty (Table 8; Figure 11).

Table 8. Comparison of total reference SLHL production rates in SPICE quartz as calculated with one time-independent scaling model (*St*) and various time-dependent scaling models (*Sf*, *Sa*, and *Lm*)

SPICE Quartz Total reference SLHL ^{10}Be production rate (2σ; at/g/yr)	Abbreviation of scaling method used to calculate production rates	Online calculator or code used to calculate SPICE production rates
3.84 ± 0.27	*St*	CRONUScalc (Marrero et al., 2016)
3.74 ± 0.25	*Lm*	CREp calculator atmospheric ^{10}Be-based VDM [a]
3.69 ± 0.24	*Lm*	CREp calculator Lifton VDM 2016 [a] (Lifton, 2016)
3.49 ± 0.23	*Lm*	CREp calculator LSD Framework [a] (Lifton et al., 2014)
3.50 ± 0.25	*Sf*	mmc1 Matlab code of Lifton et al. (2014)
3.36 ± 0.24	*Sa*	mmc1 Matlab code of Lifton et al. (2014)

Note: Production rates are reported with 2σ uncertainty**.** *St* refers to the time-independent scaling method of Lal (1991)/Stone (2000). *Sf* and *Sa* refer to the scaling methods of Lifton et al. (2014) for non-nuclide specific and nuclide specific factors, respectively. *Lm* refers to the time dependent scaling method of Lal (1991)/Stone (2000) as corrected for paleomagnetic field variations described in Nishiizumi et al. (1989) and denoted as *Lm* by Balco et al. (2008).

[a] Calculations on the CREp calculator were made in June 2019; information about the specific version of the calculator was not found on the website.

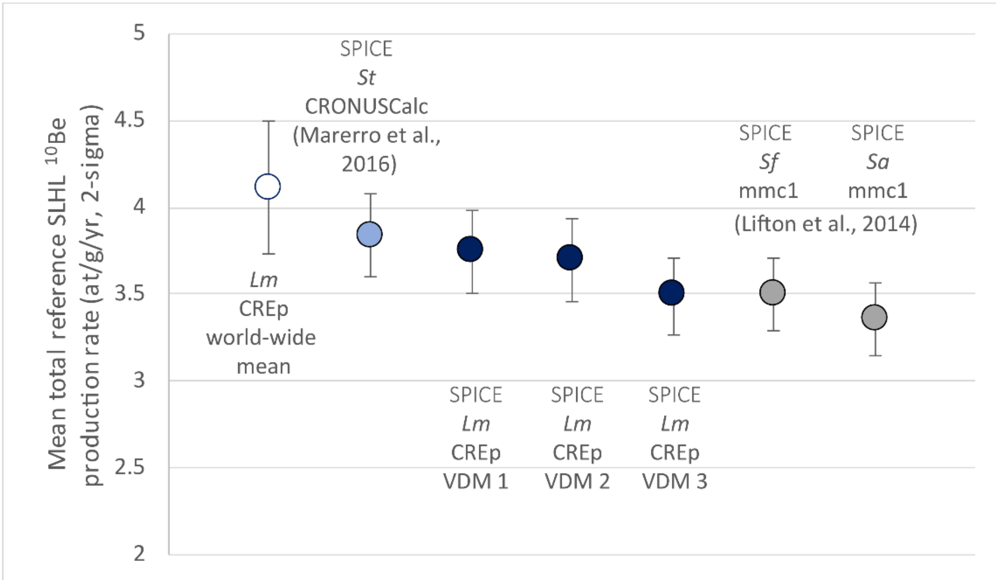

Figure 11. Comparison of SPICE *Lm*-scaled total reference SLHL ^{10}Be production rates determined with the CREp online calculator (Martin et al., 2017) with SPICE *St*-, *Sf*-, and *Sa*-scaled total reference SLHL ^{10}Be production rates calculated in this study based on scaling factors from Marerro et al. (2016) and Lifton et al. (2014; mmc1 code). The CREp world-wide mean ^{10}Be production rate shown here is calculated with VDM 1 (see section 6.5).

All error-weighted mean total reference SLHL ^{14}C production rates agree within 2σ uncertainty when scaled with *St*, *Sf*, and *Sa* scaling methods (Table 5). If samples SPICE-A7 and –A9 are excluded as outliers from calculation of total reference SLHL ^{14}C production rates, the error-weighted mean values (n=10) are 11.2 ± 0.6, 10.9 ± 0.6, and 11.0 ± 0.6 at/g/yr for *St*, *Sf*, and *Sa* scaling, respectively. Averages and standard deviations ($2\sigma_{SD}$) are also reported for the total reference SLHL ^{14}C production rates (n=10): 11.2 ± 1.7, 11.0 ± 1.7, and 11.0 ± 1.7 at/g/yr for *St*, *Sf*, and *Sa* scaling, respectively. It is not clear why samples SPICE-A7 and –A9 produce outlier ^{14}C data. There is no quantifiable erosion or burial recorded in cosmogenic ^{21}Ne or ^{10}Be concentrations in –A9 quartz, thus, the lower ^{14}C concentration is not explained by geological processes. Similarly, there is no observation of anomalously higher cosmogenic ^{21}Ne or ^{10}Be concentrations in –A7 quartz. Samples –A7 and –A9 only produce outlier ^{14}C data. It should be noted that extraction of in situ ^{14}C from quartz is a challenging process, and carbon contamination and/or carbon loss can occur.

6.5.2 SLHL production rates from muons and spallation

This study reports only total reference SLHL production rates for ^{21}Ne, because these rates includes the fast-muon induced spallation contribution to ^{21}Ne. Total reference SLHL ^{21}Ne production rates (*St*) are shown in Figures 12 and 13. Figure 12 also illustrates the SLHL <u>spallation</u> production rates (*St*) of ^{10}Be and ^{14}C in SPICE quartz. Muogenic contributions to ^{10}Be and ^{14}C production rates at SPICE sample sites include production from both fast and slow muons and are calculated using the methods described and discussed in Heisinger et al. (2002a; 2002b). Production rates of muogenic ^{10}Be and ^{14}C determined here are independent of SPICE calibration sample measurements, and rely only on literature values in Heisinger et al. (2002a; 2002b).

Spallation production rates of ^{10}Be and ^{14}C are derived by (1) subtracting the production rates resulting from negative muon capture from the total reference ^{10}Be or ^{14}C production rate at the corresponding sample elevation for each sample, and then (2) scaling the resultant spallogenic ^{10}Be and ^{14}C production rates to SLHL. The spallation production rate thus includes the production from fast-muon induced spallation, following Lal (1991)/Stone (2000) and Dunai (2000).

Production rates by muons for ^{10}Be and ^{14}C are listed in Tables 4 and 5. *St*, *Sf*, and *Sa* scaling factors give muogenic ^{10}Be SLHL production rates of 0.10, 0.07, and 0.07 at/g/yr, respectively. Using *St*, *Sf*, and *Sa* scaling factors gives muogenic ^{14}C SLHL production-rates of ~2.0, 1.5, and 1.5 at/g/yr, respectively.

Spallogenic ^{10}Be contributes ~98% to total reference ^{10}Be production rates, whereas spallogenic ^{14}C contributes approximately 80% to the total reference ^{14}C production rate at sea level (Balco et al., 2008; Kober et al., 2011; Lupker et al., 2015). Time-independent *St* scaling factors yield error-weighted mean spallation (*sp*) SLHL production rates for $^{10}Be_{sp}$ (n=10) and $^{14}C_{sp}$ (n=10) of 3.73 ± 0.26 at/g/yr and 9.2 ± 0.6 at/g/yr, respectively (Figure 12). Using the time-dependent *Sf* scaling method, these SLHL values are 3.43 ± 0.24 at/g/yr and 9.5 ± 0.5 at/g/yr, respectively. Lastly, the nuclide-specific, time-dependent *Sa* scaling factors change the SLHL values to 3.30 ± 0.23 at/g/yr and 9.5 ± 0.6 at/g/yr, respectively. The *Sf* and *Sa* scaling methods result in an overall shift of data points in a graph similar to that in Figure 12, but the individual positions of data points relative to one another do not change.

Spallation SLHL production rates for $^{14}C_{sp}$ (n=10) were also determined using the integration time (t_{int}) of Blard et al. (2019). In this case, *Sf* and *Sa* scaling factors calculated in the mmc1 code of Lifton et al. (2014) were integrated over the past 8270 yr. Using t_{int} and the time-dependent *Sf* and *Sa* scaling methods, the error-weighted mean spallation SLHL production rates for $^{14}C_{sp}$ are 9.7 ± 0.6 at/g/yr and 9.8 ± 0.6 at/g/yr (2σ), respectively. These are indistinguishable from SLHL $^{14}C_{sp}$ production rates (9.5 ± 0.5 at/g/yr *and* 9.5 ± 0.6 at/g/yr; *Sf* and *Sa*) in SPICE quartz integrated over the past 25 ka.

All error-weighted mean SLHL spallogenic ^{10}Be production rates scaled with *St*, *Sf*, and *Sa* scaling methods agree within 2σ uncertainty (Table 4; Figure 14). The same holds true for all three error-weighted SLHL spallogenic ^{14}C production rates (Table 5). To illustrate the statistical variation in ^{14}C production rates, the arithmetical means and standard deviations ($2\sigma_{SD}$) are also reported for the total reference SLHL ^{14}C production rates (n=10): 9.2 ± 1.7, 9.5 ± 1.7, and 9.6 ± 1.7 at/g/yr for *St*, *Sf*, and *Sa* scaling, respectively (Table 2). These means and standard deviations are plotted in Figure 15.

St-scaled and *Lm*-scaled production rates for ^{21}Ne, $^{10}Be_{sp}$, and $^{14}C_{sp}$ can also be calculated in the online calculator of Balco et al. (2008; https://hess.ess.washington.edu/math/v3/v3_cal_in.html). The calculator does not report total reference ^{10}Be or ^{14}C production rates in the output file. The CREp calculator was not used to calculate spallation production rates, because the CREp calculator only reports total reference production rates. The Balco online calculator yielded mean *St*-scaled spallation SLHL production rates of 16.5 ± 2.0, 3.73 ± 0.20, and 9.1 ± 3.4 at/g/yr ($2\sigma_{SD}$; two standard deviations) for cosmogenic ^{21}Ne, ^{10}Be, and ^{14}C, respectively, in SPICE quartz (Table 9). Online documentation (Balco, 2017) states “that the best-fitting reference production rates for *St* and *Lm* scaling are also not comparable to similar values generated by other code.” This indicates there is expected to be a small degree of variation amongst production-rate values determined by various online calculators of Balco et al. (2008), Marrero et al. (2016), and Martin et al. (2017). The Balco-calculator production rates, however, are in excellent agreement with *St*-scaled arithmetical mean values calculated for *St*-scaled cosmogenic ^{21}Ne, ^{10}Be, and ^{14}C in this study (16.7 ± 2.1, 3.75 ± 0.18, and 9.2 ± 1.7 at/g/yr, respectively; $2\sigma_{SD}$; Table 2). Mean *Lm*-scaled spallation SLHL production rates from the Balco calculator are 16.0 ± 2.0, 3.61 ± 0.20, and 9.6 ± 3.6 at/g/yr (2σ) for cosmogenic ^{21}Ne, ^{10}Be, and ^{14}C, respectively, in SPICE quartz. These *Lm*-scaled production rates overlap both the *St*-scaled determined for

SPICE quartz in the Balco et al. (2008) calculator and the *St*-scaled values calculated in this study well within uncertainty (Tables 2, 3, 4, and 5; Figures 13, 14, and 15).

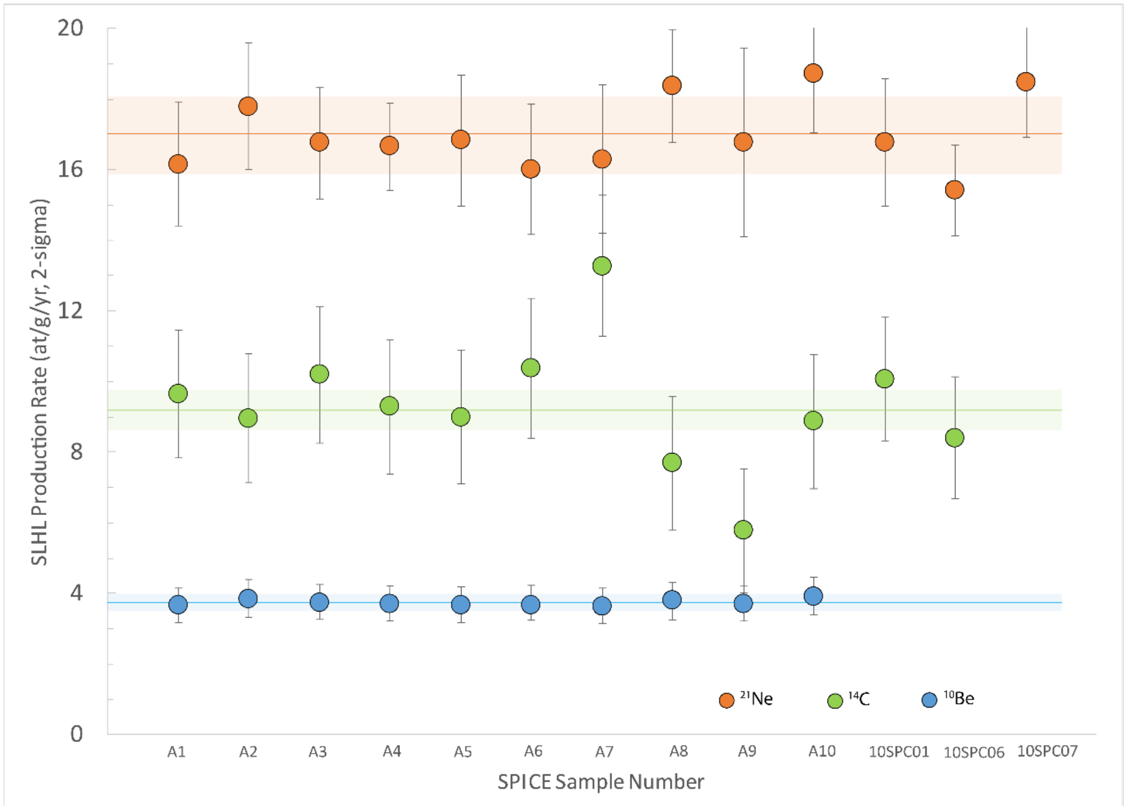

Figure 12. Total reference SLHL production rate for ^{21}Ne and spallation (*sp*) SLHL production rates for ^{10}Be and ^{14}C for samples SPICE-A1 to –A10, and 10SPC01, -06, and -07. Rates are scaled with the *St* scaling method. Solid lines represent the error-weighted mean production rates for each nuclide. Samples SPICE-A7 and –A9 are included in calculation of the error-weighted mean spallogenic ^{14}C production rate represented by the green line. Shaded rectangles represent 2σ uncertainty of each mean, and include the uncertainty associated with the ^{40}Ar/^{39}Ar age of the SP lava flow. Error bars on the circles represent 2σ uncertainty, and do not include the uncertainty of the ^{40}Ar/^{39}Ar age.

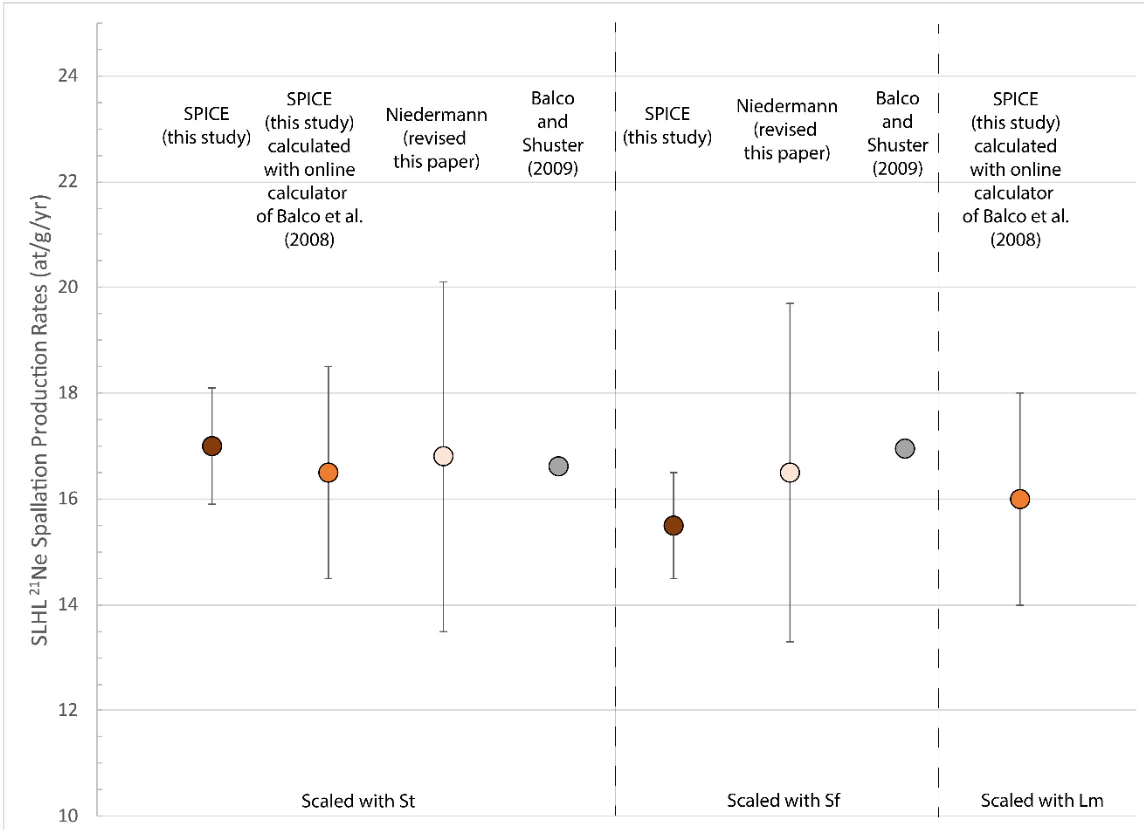

Figure 13. Comparison of the error-weighted mean ^{21}Ne production rates of the SPICE study (brown circles) with Niedermann et al.'s (1994) revised ^{21}Ne production rate (light orange), and Balco and Shuster's (2009) $^{21}Ne_{sp}$ production rate (light gray circle) scaled with *St* (on left), *Sf* (in the middle), and *Lm* (on the right) scaling methods. Also included is the SPICE ^{21}Ne production as calculated within the Balco et al. (2008) calculator (orange circles). Error bars represent 2σ uncertainty. Balco and Shuster's (2009) production rates are those as scaled and reported by Marrero et al. (2016) and Borchers et al. (2016). No uncertainties are reported with those rates. Borchers et al. (2016) state they "cannot infer statistically justifiable production rate uncertainties from the fitting exercise".

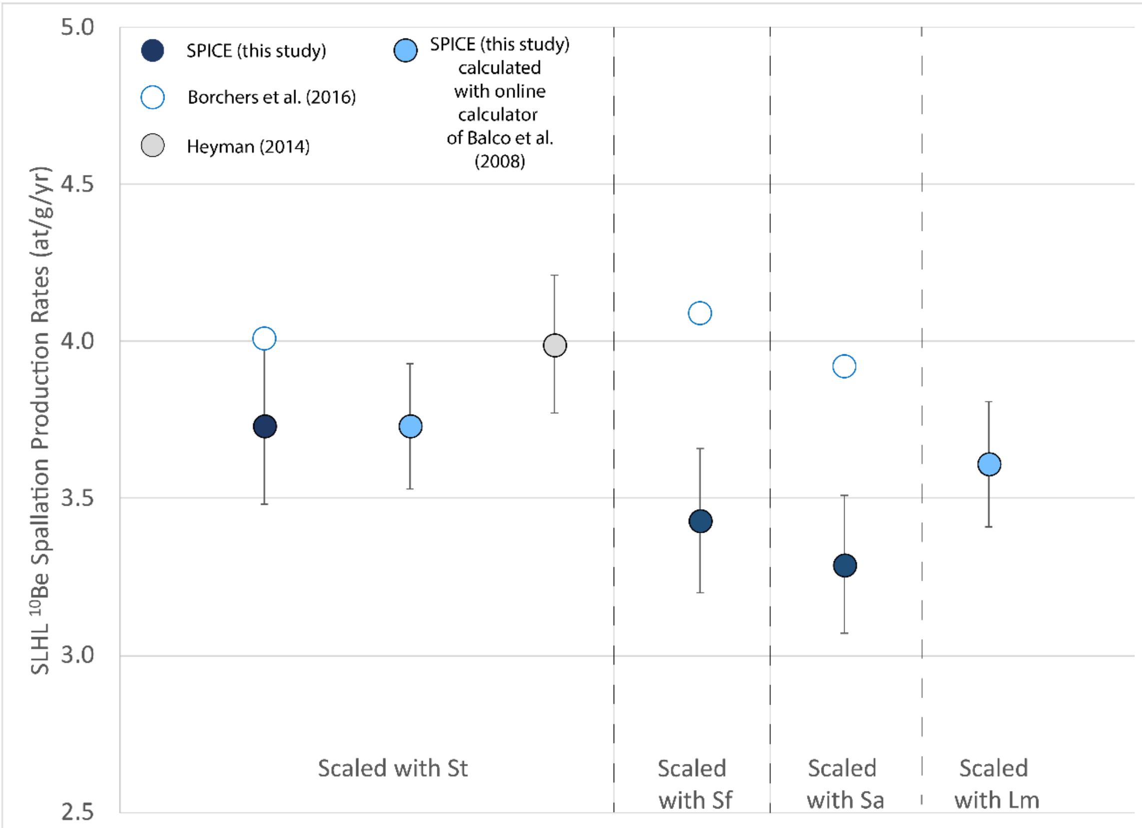

Figure 14. Comparison of the error-weighted mean spallogenic $^{10}Be_{sp}$ production rates of the SPICE study (blue circles) with Borchers et al. (2016) (white circles) scaled with *St*, *Sf*, *Sa*, and *Lm* scaling methods and the spallogenic $^{10}Be_{sp}$ production rate of Heyman (2014) (gray circle; *St* scaling). Error bars represent 2σ uncertainty.

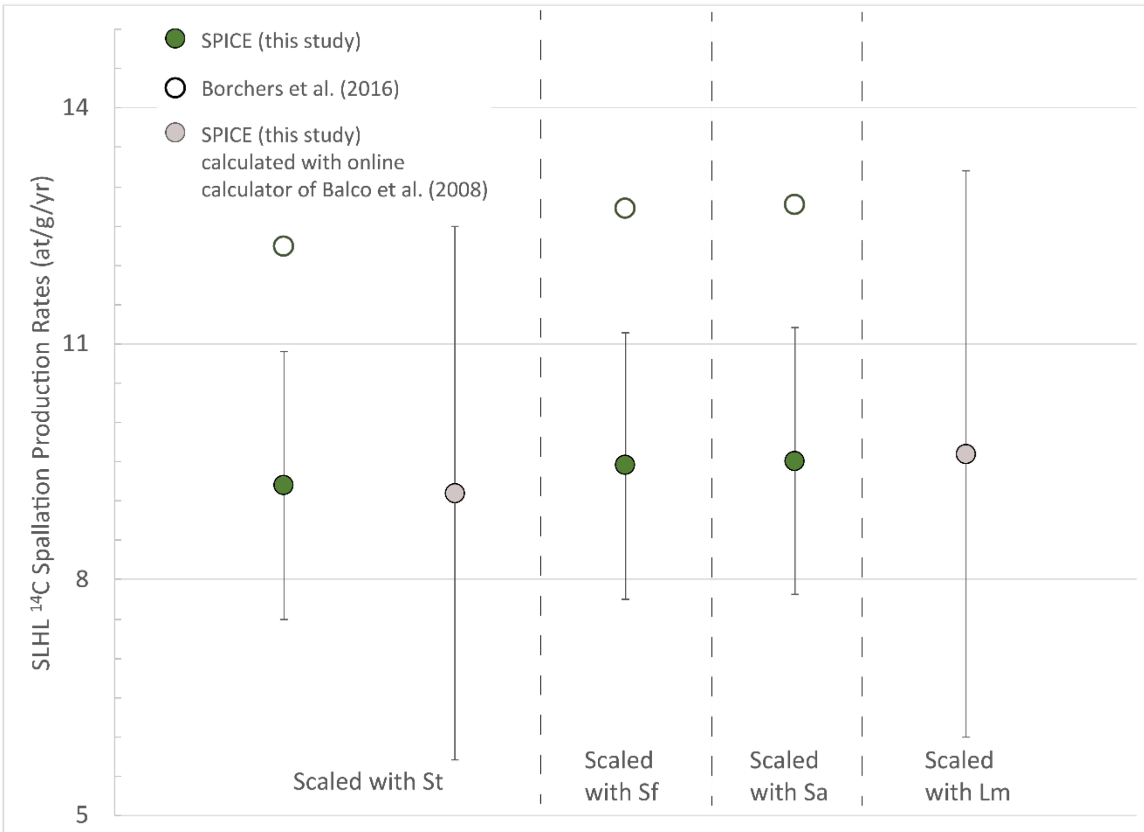

Figure 15. Comparison of the error-weighted mean spallogenic $^{14}C_{sp}$ production rates of the SPICE study (dark green, light green, and gray circles) and Borchers et al. (2016) (white circles) scaled with *St*, *Sf*, *Sa*, and *Lm* scaling methods. Error bars represent two standard deviations (Table 2), because they are much greater than the uncertainties associated with the error-weighted means.

Table 9. Comparison of spallation production rates in SPICE quartz as calculated in the online calculator of Balco et al. (2008)

Cosmogenic nuclide	SLHL Production Rate *St* online calculator of Balco et al. (2008)[a] (at/g/yr)	SLHL Production Rate *Lm* online calculator of Balco et al. (2008)[a] (at/g/yr)
SPICE $^{10}Be_{sp}$	3.73 ± 0.20	3.61 ± 0.20
SPICE $^{14}C_{sp}$	9.1 ± 3.4	9.6 ± 3.6
SPICE ^{21}Ne	16.5 ± 2.0	16.0 ± 2.0

Note: Uncertainty is reported here as two standard deviations ($2\sigma_{SD}$) according to online documentation (Balco, 2017).The subscript *sp* refers to a production rate produced by spallation reactions. *St* refers to the time-independent scaling method of Lal (1991)/Stone (2000). *Lm* refers to the time dependent scaling method of Lal (1991)/Stone (2000) as corrected for paleomagnetic corrections described in Nishiizumi et al. (1989) and denoted as *Lm* by Balco et al. (2008).

[a] Version 3 of production-rate calibration code: wrapper 3.0.2; get_age 3.0.2; muons 1A, alpha = 1; validate_v3_input.m – 3.0; consts 3.0.4

7. Discussion

7.1 Local production rates: predicted vs measured

We hypothesize that if increased cosmogenic nuclide production between 20 and 50 ka was significant (e.g., measureable at the precision of AMS and noble gas mass spectrometry available at the moment), the SP flow surface should contain a concentration of cosmogenic nuclides that would be higher than predicted by the time-independent *St* scaling method. This would mean that unscaled, calibrated (measured) <u>local</u> production rates would be higher than rates predicted by scaling global SLHL production rates calibrated on surfaces that are <20 ka with *St* scaling factors. *St* scaling factors do not include a correction for temporal fluctuations in geomagnetic field strength.

To test this hypothesis, we compare <u>predicted</u> local production rates scaled to SPICE sample sites with *St*, *Sf*, and *Sa* scaling methods to <u>unscaled, calibrated</u> local production rates, based on the measured inventories of cosmogenic ^{21}Ne, ^{10}Be, and ^{14}C in SP flow quartz. Predicted production rates based on the *Lm*-scaling method were not directly tested in this study, because (1) the mmc1 code of Lifton et al. (2014) only calculates *Sf* and *Sa* scaling factors; (2) the online calculators of Balco et al. (2008) and Martin et al. (2017) do not report separate scaling factors for spallogenic and muogenic contributions to total nuclide production, nor do the calculators list scaling factors for each time step within the 72-ka exposure history at the SP flow; and (3) it is not possible to specify an exact time (e.g., 72 ka or 25 ka) in the CRONUSCalc calculator over which time-integrated scaling factors for spallation or muon-induced production should be calculated. *Lm* scaling factors, however, are greater than *St* scaling factors and less than *Sf* scaling factors (see section 6.5), thus, it can be inferred that *Lm*-scaled production rates will be less than *St*-scaled rates and greater than *Sf*-scaled rates.

Predicted local production rates plotted in Figures 16, 17, and 18 are based on the updated SLHL ^{21}Ne production rate of Niedermann (this paper; 16.8 (*St*) and 16.5 (*Sf*) at/g/yr; Table 2) and the global, average SLHL ^{10}Be and ^{14}C production rates used in the CRONUSCalc calculator (Table 2; Borchers et al., 2016; Marrero et al., 2016). Table SD4 lists the *St* and *Sf* scaling factors used to calculate the predicted local ^{21}Ne production rates. Predicted local ^{10}Be and ^{14}C production rates are calculated by the online CRONUSCalc calculator using the scaling factors and SLHL production rates therein (Marrero et al., 2016). In Figures 16, 17, and 18, all predicted *Sf*-scaled and *Sa*-scaled local production rates are greater than predicted *St*-scaled local production rates.

Figure 16 shows the predicted local ^{21}Ne production rates (*St* and *Sf*) and measured ^{21}Ne local production rates for SP flow quartz. Eight of thirteen samples have calibrated local ^{21}Ne production rates (within 2σ uncertainty) that plot directly on or below predicted *St* local production rates. Calibrated production rates from five of these samples also overlap their predicted *Sf* local production rates within 2σ uncertainty. Sample 10SPC06 plots significantly below its predicted *St* and *Sf* local production rates, failing to overlap either within 2σ uncertainty. Of the four remaining samples, samples SPICE–A2, –A8, -A10, and 10SPC07 overlap *Sf*- scaled predicted local production rates within 2σ uncertainty; however only calibrated local production rates of samples –A2 and –A8 also overlap the *St*-scaled predicted local production rates within 2σ uncertainty.

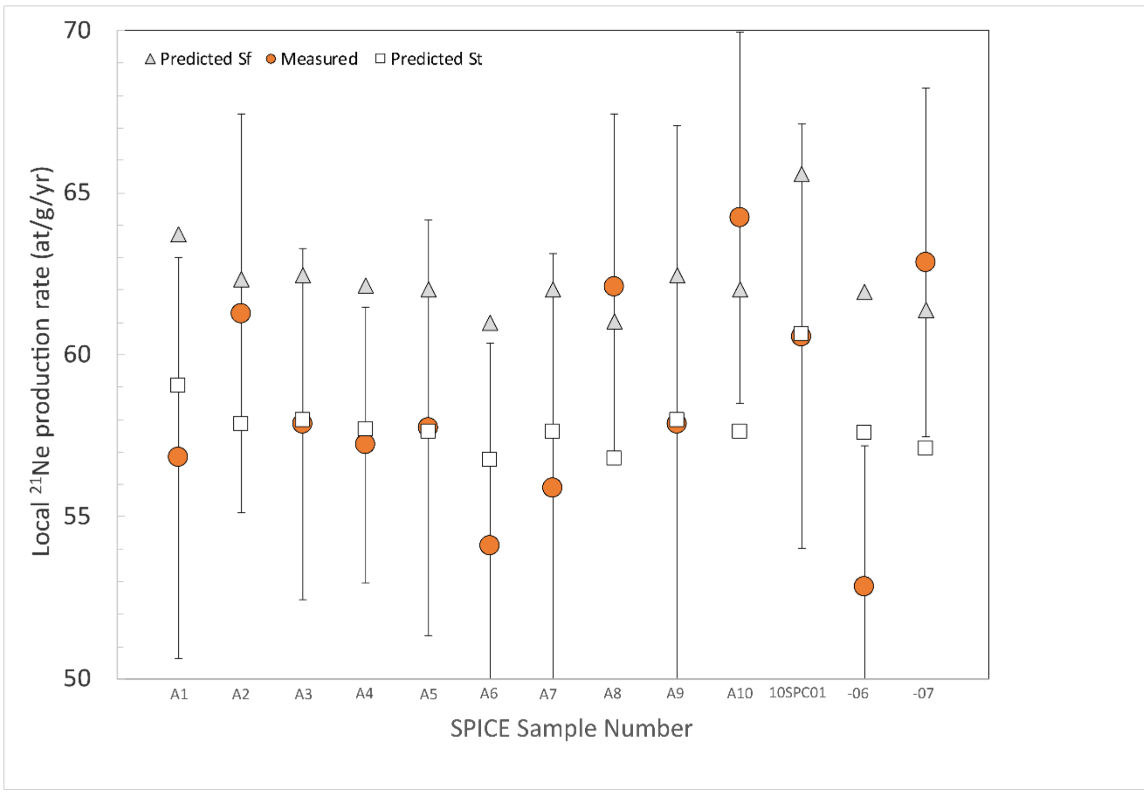

Figure 16. Comparison of the predicted local ^{21}Ne production rates and the unscaled local production rates measured in SP flow quartz. Error bars are on measured values (orange circles), represent 2σ uncertainty, and do not include uncertainty on the ^{40}Ar/^{39}Ar age.

In summary, ten of thirteen quartz samples have calibrated local ^{21}Ne production rates that agree with predicted *St* local ^{21}Ne production rates at the SP flow. Only three samples plot statistically above or below predicted *St* local production rates. This indicates that production of cosmogenic ^{21}Ne over the past 72 ka is not significantly greater than cosmogenic ^{21}Ne production rates integrated over the past 15.75 ka (Figures 6 and 13). Assuming *St* scaling factors are accurate, the strong agreement between the predicted (*St*) and measured local ^{21}Ne production rates also supports field evidence of negligible erosion at SPICE sample sites.

Figure 17 shows the predicted local ^{10}Be production rates (*St*, *Sf,* and *Sa)* and calibrated (measured) ^{10}Be local production rates for SP flow quartz. Except for sample SPICE-A1, measured local ^{10}Be production rates are all systematically, nominally higher than the predicted local ^{10}Be production rates scaled with the *St* method. Even so, measured production rates agree very well with predicted *St* production rates, and overlap predicted values within 2σ uncertainty. Measured local ^{10}Be production rates for six samples (SPICE-A2, -A3, -A4, -A8, -A9, and -A10) agree with predicted local *Sf* ^{10}Be production rates within 2σ uncertainty. Three of these samples (SPICE-A2, -A8, and -A10) also overlap with predicted local *Sa* ^{10}Be production rates within 2σ uncertainty.

All ten quartz samples have calibrated local ^{10}Be production rates that agree with predicted *St* local ^{10}Be production rates at the SP flow. None of the samples plot statistically above or below predicted *St* local production rates. This indicates that production of cosmogenic ^{10}Be over the past 72 ka is not significantly greater than *St*-scaled cosmogenic ^{10}Be production rates integrated over the past 20 ka. Just as with agreement between ^{21}Ne production rates at the SP flow, the strong agreement between the predicted (*St*) and measured local ^{10}Be production rates also supports field observations of negligible erosion at SPICE sample sites.

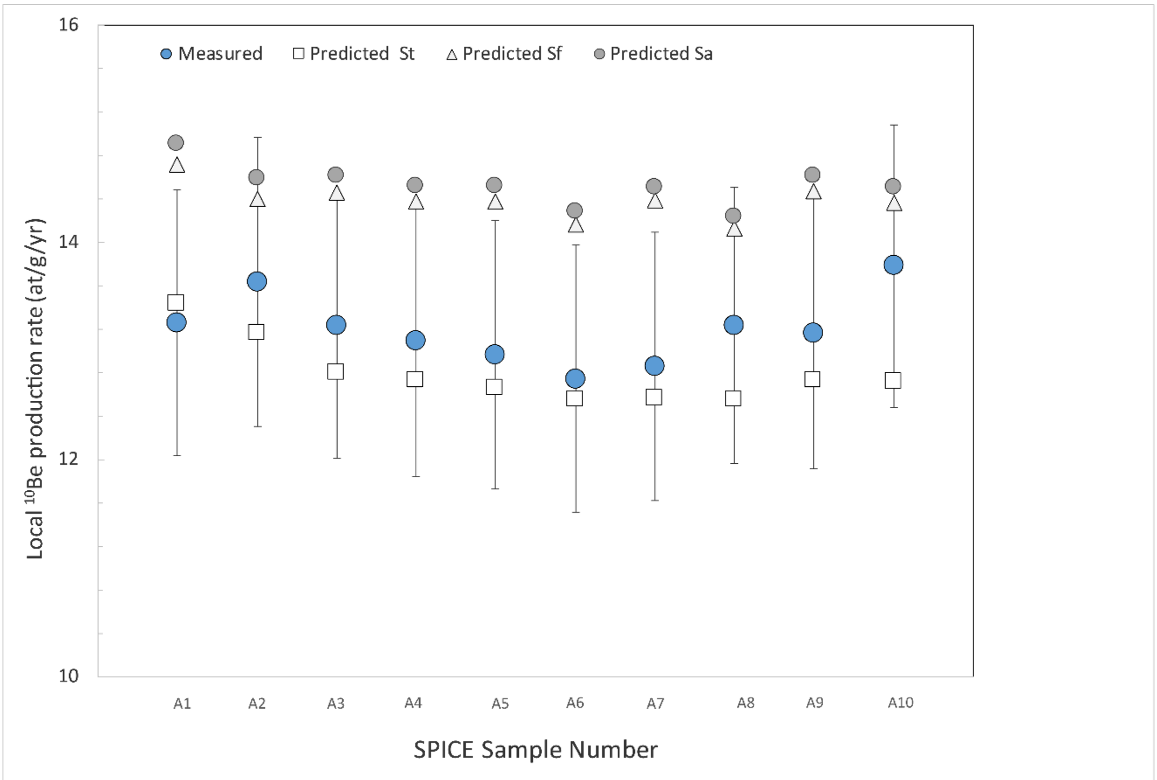

Figure 17. Comparison of the predicted local ^{10}Be production rates and the unscaled local production rates measured in SP flow quartz. Error bars are on measured values (blue circles), represent 2σ uncertainty, and do not include uncertainty on the $^{40}Ar/^{39}Ar$ age.

Figure 18 shows the predicted local ^{14}C production rates (*St* and *Sa)* and measured ^{14}C local production rates for SP flow quartz. In order to simplify the graph, predicted local production rates are not shown for the *Sf* scaling method. These rates fall between the predicted local ^{14}C production rates scaled with *St* and *Sa* methods.

All calibrated (measured) local ^{14}C production rates, except for sample SPICE-A7 (outlier), are systematically lower than the predicted local ^{14}C production rates scaled with both *St* and *Sa* methods. Only two samples (SPICE-A3 and –A6) overlap with predicted local ^{14}C production rates (*St* scaling) within 2σ uncertainty. None of the samples overlap predicted *Sa*-scaled local ^{14}C production rates.

Predicted local ^{14}C production rates (*St* scaling) were calculated by the CRONUSCalc calculator, using the ^{14}C production rate (12.24 at/g/yr; *St* scaling) of Borchers et al. (2016). This SLHL ^{14}C production rate is based only on two pre-2010 production-rate publications at sites <17.4 ka in age, excluding the lower SLHL ^{14}C production rates reported in Schimmelpfennig et al. (2012) and Young et al. (2014). It is possible that the SP flow is affected by erosion, or that quartz in the SP flow records in-situ cosmogenic ^{14}C production rates that are lower at this set of latitudes, longitudes, and elevations.

Erosional effects on ^{14}C concentrations must be considered. The low ^{14}C concentrations in SP flow quartz might indicate that the pressure-ridge surfaces are not original, primary flow surfaces. Sims et al. (2007) report an erosion rate of 1.7 mm/ka for a 60 ka basalt in New Mexico, which has weathered in a similar arid environment to that of the SP flow. Calculations indicate that much higher erosion rates of 15 to 53 mm/ka, or 108 to 310 cm of total erosion, would be required over the past 72 ka to explain the disparity between the SPICE ^{14}C production rate (*St*) and the ^{14}C production rate of Borchers et al. (2016; *St*; Figures 15 and 18). Based on field observations alone (Figures S1-S13), it is unrealistic this much erosion has occurred on the SP flow at SPICE sample sites. Furthermore, if erosion rates on the SP-flow surface were 15 to 53 mm/ka, we would also expect much lower cosmogenic ^{21}Ne and ^{10}Be concentrations in the same quartz samples in which ^{14}C was also measured. Measured ^{21}Ne and ^{10}Be concentrations measured in this study do not reflect this decrease (Figures 13 and 14). To explain the small differences between SPICE ^{21}Ne production rates (*St*) and the ^{21}Ne production rate of Borchers et al. (2016; 16.63 at/g/yr), the surfaces of sample sites would require 1.4 to

11 cm of total erosion rates of 0.2 to 1.5 mm/ka over 72 ka. Similarly, to explain the small differences between SPICE ^{10}Be production rates (*St*) and the ^{10}Be production rate of Borchers et al. (2016; 4.01 at/g/yr), sample sites would require 3 to 14 cm of total erosion at erosion rates of 0.5 to 1.9 mm/ka over 72 ka. While these ^{21}Ne and ^{10}Be erosion rates (0.2 - 1.9 mm/ka) are realistic and do, in some cases, overlap the erosion rate of Sims et al. (2007), field evidence does not support erosion of the SP-flow surface on the order of 10^1- 10^2 cm over the past 72 ka.

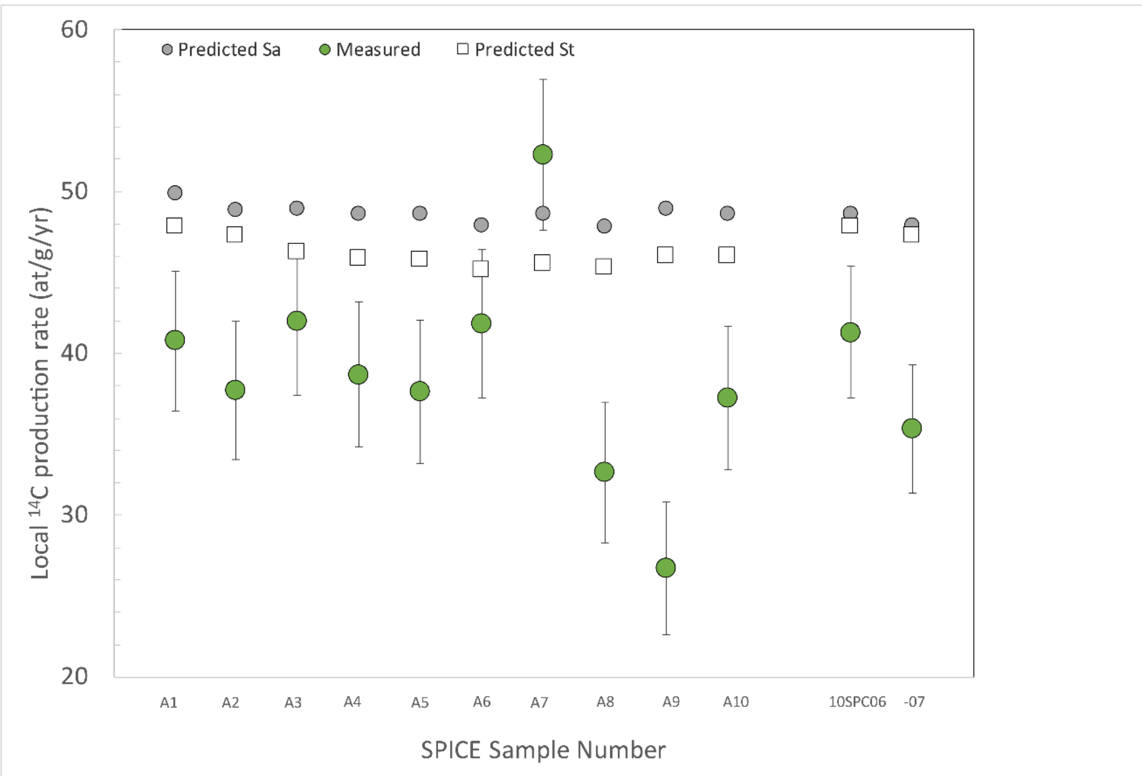

Figure 18. Comparison of the predicted local ^{14}C production rates and the unscaled local production rates measured in SP flow quartz. Error bars are on measured values (green circles), represent 2σ uncertainty, and do not include uncertainty on the radiocarbon half-life.

7.2 Production rates from spallation

New SPICE ^{21}Ne production rates in quartz agree very well with other ^{21}Ne production rates in the literature (Figures 6 and 13). The error-weighted mean SLHL total reference ^{21}Ne production rate from the SPICE study (17.0 ± 1.1 at/g/yr; *St* scaling) is in excellent agreement with both the Sierra Nevada SLHL ^{21}Ne production rate (Niedermann et al., 1994) updated in this paper (16.8 ± 3.3 at/g/yr; 2σ; *St* scaling) and the Antarctica SLHL ^{21}Ne production rate (Balco and Shuster, 2009) used in the calculator of Marrero et al. (2016) (16.63 at/g/yr; *St* scaling).

When SLHL ^{21}Ne production rates from SPICE samples are scaled with the *Sf* scaling method, agreement of the SPICE and Sierra Nevada production rates with the Antarctica rate is not as strong. The *Sf* scaling method yields SLHL $^{21}Ne_{sp}$ production rates for both the SPICE study (15.5 ± 1.0 at/g/yr) and the updated Sierra Nevada study (16.5 ± 3.2 at/g/yr) that are lower than the rates calculated with *St* scaling factors, but still overlap within 2σ uncertainty. The lower rate (15.5 ± 1.0 at/g/yr) is nominally less than the Antarctica SLHL^{21}Ne production rate (16.96 at/g/yr; *Sf* scaled), but the disagreement is not notably large. Recall that uncertainties are not reported with the production rates reported in Borchers et al. (2016). It is possible that the *Sf* –scaled Antarctica SLHL and SPICE SLHL ^{21}Ne production rates would overlap within uncertainty if it were reported.

Small differences in *Sf* scaled SLHL ^{21}Ne production rates are possibly due to significant age differences at the separate sample sites. The SPICE and Sierra Nevada sample sites are 72 ka and 15.75 ka, respectively, whereas the Antarctica sites have exposure histories ranging from 8 to 14 Ma. The agreement in SLHL ^{21}Ne production rates for a given scaling method (*St* or *Sf*) at the three different sites (SP flow, Sierra Nevada, and Antarctica) and with other indirectly determined rates in the literature (*St* scaling; Figure 6), however, indicates the integrated production rate of cosmogenic ^{21}Ne has not varied much between ~14 Ma and 15.75 ka. The agreement in rates also confirms the lack of measureable erosion at the SP flow sample sites, regardless of scaling method (*St* or *Sf*).

Notable differences in SPICE SLHL spallogenic $^{10}Be_{sp}$ production rates are obtained with the three *St*, *Sf*, *Sa*, and *Lm* scaling methods, particularly when compared to the global, average SLHL $^{10}Be_{sp}$ production rates of Heyman (2014) and Borchers et al. (2016). The SPICE project's error-weighted mean SLHL spallogenic $^{10}Be_{sp}$ production rate, when scaled with the *St* scaling method, is 7% lower than both the $^{10}Be_{sp}$ production rates of Borchers et al. (2016) and Heyman (2014), but still overlaps the two rates within 2σ uncertainty (Figure 14). There is very little variation between the SLHL $^{10}Be_{sp}$ production rates of Borchers et al. (2016; 3.92 - 4.09 at/g/yr) when scaled with *St*, *Sf*, and *Sa* scaling methods. In strong contrast, SPICE SLHL $^{10}Be_{sp}$ production rates show a systematic decrease with different scaling methods, changing from 3.73 ± 0.26 at/g/yr (*St*) to 3.43 ± 0.24 at/g/yr (*Sf*) and, lastly, to 3.30 ± 0.23 at/g/yr (*Sa*). The *St* scaled and *Sa* scaled SLHL $^{10}Be_{sp}$ production rates from SPICE quartz just overlap within 2σ uncertainty (Figure 14). The mean *Lm*-scaled SLHL spallogenic $^{10}Be_{sp}$ production rate calculated for SPICE quartz in Balco et al.'s (2008) online calculator is 3.61 ± 0.20 at/g/yr; 2σ). This rate is nominally greater than $^{10}Be_{sp}$ rates scaled with the *Sf* and *Sa* methods, and nominally less than *St*-scaled SLHL $^{10}Be_{sp}$ production rates (Figure 14). The *Lm*-scaled mean SLHL spallogenic $^{10}Be_{sp}$ production rate agrees with *St*, *Sf*, and *Sa*-scaled rates within uncertainty.

The time periods over which *Sf* and *Sa* scaling factors are averaged have different effects on the ^{10}Be production rate values of Borchers et al (2016) and those of the SPICE study. The $^{10}Be_{sp}$ production rates included in the Borchers et al. (2016) value are all from sample sites with independent ages less than 20 ka, thus, the different time-independent (*St*) and time-dependent (*Sf* and *Sa*) scaling methods are going to produce very similar scaling factors and, thus, very similar production rates (3.92 - 4.09 at/g/yr). Recall the similarities between *St*, *Sf*, and *Sa* scaling factors calculated for the past 20 ka at the SPICE-A1 sample site (section 6.5, Figure 10). The past ~20 ka incorporates periods of time when the Earth's magnetic field was both weaker and stronger, and thus created conditions for both increased and decreased cosmogenic nuclide production at the Earth's surface (Lifton et al., 2014). The magnitude of these changes in production rates, more or less, balances each other out when scaled with time-dependent *Sf* and *Sa* scaling factors (Figure 10). In contrast, the exposure history of the SP flow (over the past 72 ka) includes the proposed period of time between 20 and 50 ka when the Earth's magnetic field was weaker (Lifton et al., 2014), and thus, it is hypothesized, there was increased cosmogenic nuclide production (Figure 10). This period of proposed increased nuclide production was not 'balanced out' by a period of equally decreased nuclide production, thus, the time-dependent *Sf* and *Sa* scaling factors over the past 72 ka at the SP flow are significantly higher than the time-independent *St* scaling factors. For these reasons, the *St*-scaled SLHL $^{10}Be_{sp}$ production rate (3.73 ± 0.26 at/g/yr) determined from SPICE samples overlaps the production rates of Borchers et al. (2016) and Heyman (2014) within 2σ uncertainty, but *Sf*- and *Sa*- scaled SPICE ^{10}Be production rates do not agree with the *St*, *Sf* and *Sa* scaled rates of Borchers et al. (2016) and Heyman (2014) (Figure 14). Time-dependent SLHL $^{10}Be_{sp}$ production rates of 3.43 ± 0.24 at/g/yr (*Sf*) and 3.30 ± 0.23 at/g/yr (*Sa*) are significantly lower, based on *Sf* and *Sa* scaling factors at the SP flow that are 9-10% and 13-14% higher than time-independent *St* scaling factors.

It is important to point out these differences in values, because the popular online calculators of Balco et al. (2008) and Marrero et al. (2016) use the SLHL ^{10}Be production rates published in Borchers et al. (2016), and yet the calculators are used to determine exposure ages for surfaces with exposures histories greater than 20 ka. The *Sa* and *Sf* scaled ^{10}Be production rates (4.09 and 3.92 at/g/yr, respectively) of Borchers et al. (2016) are significantly higher than *Sa* and *Sf* scaled ^{10}Be production rates determined in the SPICE study (3.43 and 3.29). The CREp online calculator reports world-wide mean total reference SLHL ^{10}Be production rates of 4.11± 0.38, 4.09 ± 0.38, and 4.06 ± 0.38 at/g/yr (2σ; *Lm* scaling with VDM 1, VDM 2, and VDM 3, respectively). These rates are in agreement with, but nominally higher than, the total reference SLHL ^{10}Be production rates calibrated in SPICE quartz for VDM 1, VDM 2, and VDM 3 geomagnetic corrections (3.74 ± 0.25, 3.69 ± 0.24 at/g/yr, and 3.49 ± 0.23 at/g/yr, respectively; 2σ; *Lm* scaling).

If the higher ^{10}Be SLHL production rates (~4 at/g/yr) are scaled with *Sf*, *Sa*, or *Lm* methods to calculate an exposure age at a ~70 ka landform, the resultant exposure age could be erroneously too young. For example, using the CRONUSCalc ^{26}Al/^{10}Be Exposure Age Calculator (v 2.0) of Marrero et al. (2016) and ^{10}Be concentrations in quartz from SP flow quartz samples, mean exposure ages of 70.6 ± 4.2 ka, 67.1 ± 4.1 ka, and 67.1 ± 3.8 ka (error-weighted means; 2σ) were calculated using *St*, *Sf*, and *Sa* scaling, respectively. *St* scaled ^{10}Be exposure ages best match the ^{40}Ar/^{39}Ar age of the SP lava flow (72 ± 4 ka; 2σ). Though all three mean exposure ages overlap within 2σ uncertainty, *Sf* and *Sa* scaled mean ^{10}Be exposure ages are 4.9% lower than the mean *St*-scaled ^{10}Be exposure ages. The CREp calculator yields mean *Lm*-scaled exposure ages of 65.1 ± 2.6

ka, 64.7 ± 2.4 ka, and 61.7 ± 2.4 ka (error-weighted means; 2σ) when calculated using VDM 1, VDM 2, and VDM 3 geomagnetic correction models and the total reference SLHL ^{10}Be production rates of 4.11 ± 0.38, 4.09 ± 0.38, and 4.06 ± 0.38 at/g/yr, respectively, of Martin et al. (2017). These ages are 7.8 to 12.6% lower than the *St*-scaled ^{10}Be exposure age (70.6 ka) produced within the CRONUSCalc calculator.

Simply stated, a cosmogenic nuclide concentration divided by a production rate that is too high will result in an exposure age that is too young, which may make it seem that a landform has experienced quantifiable erosion and/or burial, even when that is not the case and no field evidence supports it.

SLHL spallogenic ^{14}C production rates from the SPICE project and other SLHL ^{14}C production rates in the literature are integrated over similar time periods (25 ka and <17.4 ka), thus we expect more similar variations in *St*, *Sf* and *Sa* scaled production rates than are observed when comparing spallogenic ^{10}Be as discussed above (Figure 7). *Sf* and *Sa* scaling factors for SPICE sample sites average over the past 25 ka, and *Sf* and *Sa* scaling factors used by Borchers et al (2016) are over the past 17.4 ka or less.

The error-weighted mean SLHL spallogenic ^{14}C production rate of the SPICE study is 9.2 ± 0.6 at/g/yr (*St*). The arithmetical mean SLHL spallogenic ^{14}C production rate with two standard deviations is 9.2 ± 1.7 at/g/yr (*St*). The SLHL $^{14}C_{sp}$ production rate is nominally lower than other previously published SLHL $^{14}C_{sp}$ production rates, but the SPICE production rate does overlap the rate of Dugan et al. (2008; 12.4 ± 3.2 at/g/yr (*St*)) within 2σ uncertainty (Figure 7). If arithmetical means with two standard deviations are used to assess the data, the mean SLHL spallogenic ^{14}C production rate in SPICE quartz also overlaps the ^{14}C production rates of Schimmelpfennig et al. (2012) and Young et al.

(2014). The Balco et al. (2008) calculator yields mean SLHL spallogenic ^{14}C production rates in SPICE quartz of 9.1 ± 3.4 at/g/yr (*St*) and 9.6 ± 3.6 at/g/yr (*Lm*) with uncertainty reported here as two standard deviations ($2\sigma_{SD}$). These Balco-calculator ^{14}C rates overlap those calculated in this study (9.2 – 9.5 at/g/yr) and the ^{14}C rates of Borchers et al. (2016) determined with *St*, *Sf*, and *Sa* scaling methods (Figure 15).

The ^{14}C SPICE data set and the ^{14}C data set of Borchers et al. (2016) each show small ranges in production rates with changes in scaling methods, because geomagnetic field corrections for the 25 ka and <17.4 ka time periods are small. Time-dependent (*Sf* and *Sa*) scaling factors for SPICE ^{14}C production rates are integrated over the past 25 ka. These spallogenic ^{14}C production rates calculated with time-dependent *Sf* and *Sa* scaling factors at the SP flow are only ~2% higher than the spallogenic ^{14}C production rate scaled with *St* scaling factors (Figure 15). The three SLHL spallogenic $^{14}C_{sp}$ production rates calculated with the *St*, *Sf*, and *Sa* scaling factors range from 9.2 at/g/yr (*St*) to 9.5 at/g/yr (*Sf* and *Sa*), and are indistinguishable from one another within 2σ uncertainty, regardless of scaling method.

Muogenic ^{14}C SLHL production rates in SPICE quartz are 12 to 20% of total reference ^{14}C production rates.While Lupker et al. (2015) obtained very similar muon-production rate parameters to those reported in Heisinger et al. (2002a; 2002b), the parameters of Lupker et al. (2015) were calculated using a SLHL ^{14}C spallation production rate of 12.3 at/g/yr. The proportion of muon production relative to total ^{14}C production found in the Lupker et al. (2015) study would likely be higher if a lower spallation production rate (e.g., SPICE $^{14}C_{sp}$ of 9.2 - 9.5 at/g/yr) was used.

Comparison of error-weighted mean and arithmetical mean SLHL $^{14}C_{sp}$ production rates of the SPICE study (*St*, *Sf*, and *Sa* scaling) to the $^{14}C_{sp}$ production rates of Borchers et al. (2016) also scaled with *St*, *Sf*, and *Sa* scaling methods shows that mean SPICE values (9.2 – 9.5 at/g/yr) are systematically lower than those of Borchers et al. (2016) (12.24 – 12.76 at/g/yr; Table 2; Figures 15 and 18). The three production-rate values of Borchers et al. (2016) also exhibit little variation (4%) in comparison to one another.

Although the SPICE SLHL cosmogenic $^{14}C_{sp}$ production rates (8.6 – 10.1 at/g/yr, including 2σ uncertainty) are nominally lower than the previously reported $^{14}C_{sp}$ production rates of Dugan et al. (2008), Schimmelpfennig et al. (2012), and Young et al. (2014), SPICE rates do overlap these three rates within two standard deviations (Table 2; Figure 7), and add to a growing database of calibrated ^{14}C production rates around the world.

8. Conclusions

The SPICE study has generated a robust dataset of cross-calibrated production rates of cosmogenic ^{21}Ne, ^{10}Be, and ^{14}C in quartz samples extracted from the basaltic SP lava flow. Cosmogenic ^{21}Ne and ^{10}Be production rates are calibrated to the independent $^{40}Ar/^{39}Ar$ age of the lava flow (72 ± 4 ka; 2σ). Cosmogenic ^{14}C rates are calculated based on the assumption that quartz in the SP flow has reached saturation with respect to in situ ^{14}C. Cosmogenic ^{21}Ne production rates (n=13) and ^{10}Be production rates (n=10) for each SPICE quartz sample agree within 2σ uncertainty. Cosmogenic ^{14}C production rates (n=12) for each SPICE quartz sample agree within 2σ uncertainty, except for ^{14}C data from samples SPICE-A7 and –A9. These samples are considered outliers for ^{14}C data and removed from calculations of error-weighted means.

Cosmogenic ^{21}Ne and ^{10}Be concentrations in SP flow quartz strongly support field evidence for negligible erosion and/or burial on pressure ridges where samples were collected. Error-weighted mean SLHL total reference ^{21}Ne and ^{10}Be production rates at the SP flow are 17.0 ± 1.1 at/g/yr and 3.84 ± 0.27 at/g/yr (2σ; *St* scaling), respectively. These SPICE production rates agree very well and within 2σ uncertainty with *St* scaled SLHL total reference ^{21}Ne and spallogenic ^{10}Be production rates reported in the literature (Figures 6, 11, and 13). The *St* scaled SLHL total reference ^{21}Ne production rate determined for 72 ka SP flow quartz is in excellent agreement with the newly revised (this paper) total reference ^{21}Ne production rate of Niedermann et al. (1994) of 16.8 ± 3.3 at/g/yr (2σ; *St*). The error-weighted mean SLHL spallogenic ^{10}Be production rate of 3.73 ± 0.26 at/g/yr (2σ; *St* scaling) determined for SP flow quartz is nominally lower but overlaps the global, average $^{10}Be_{sp}$ production rates of Borchers et al. (2016; 4.01 at/g/yr (*St*)) and Heyman (2014; 3.99 at/g/yr (*St*)) within 2σ uncertainty. The total reference ^{10}Be production rates calibrated in SPICE quartz for the CREp calculator's VDM 1, VDM 2, and VDM 3 geomagnetic corrections are 3.74 ± 0.25, 3.69 ± 0.24, and 3.49 ± 0.23 at/g/yr, respectively (2σ; *Lm* scaling). The rates are nominally lower, but in agreement with, the world-wide mean total reference SLHL ^{10}Be production rate of 4.11 ± 0.38, 4.09 ± 0.38, and 4.06 ± 0.38 at/g/yr (2σ; *Lm* scaling with VDM 1, VDM 2, and VDM 3, respectively) used in the CREp calculator (Martin et al., 2017). The global average ^{10}Be rates of Heyman (2014), Borchers et al. (2016), and Martin et al. (2017) are calibrated on surfaces younger than 20 ka. If SPICE samples were affected by significant erosion and/or burial, reduced production of cosmogenic ^{21}Ne and ^{10}Be would be recorded in quartz samples and rates would not agree so well with other ^{21}Ne and ^{10}Be in the literature. The SPICE study shows there is variation in SLHL ^{21}Ne and ^{10}Be production rates mainly due to numerical differences in various scaling time-independent and time-dependent methods, but there is no measureable difference between the *St* scaled production rates of cosmogenic ^{21}Ne and ^{10}Be at the SP flow over the past 20 ka and rates over the past 72 ka. This could mean that ^{21}Ne and ^{10}Be production rates in quartz were not significantly greater during the proposed period of decreased magnetic field strength from 20 to 50 ka. It could also mean that increased nuclide production during this period is not recorded in SP flow quartz at a concentration that is detectable with current precision and technology of AMS and noble gas mass spectrometry.

The SPICE study also suggests that production of cosmogenic ^{14}C in SP flow quartz may have been lower over the past 25 ka than production of cosmogenic ^{14}C at other global locations with ages between 9.6 and 17.4 ka. The error-weighted mean SLHL total reference and spallogenic ^{14}C production rates are 11.2 ± 0.6 at/g/yr and 9.2 ± 0.6 at/g/yr (2σ; *St* scaling), respectively. This latter rate is lower than the *St*-scaled SLHL spallogenic ^{14}C production rate of Borchers et al. (2016; 12.24, no error reported) but this rate does overlap one of the four SLHL spallogenic ^{14}C production rates (*St* scaling) reported in the literature (9.2 – 15.6 at/g/yr, including 2σ uncertainty; Dugan, 2008).

Borchers et al. (2016) conclude there is no significant, statistical difference between SLHL ^{21}Ne, ^{10}Be, and ^{14}C production rates calibrated and scaled over the past ~20 ka using either *St*, *Sf*, or *Sa* scaling factors (Table 2). The SPICE study also shows very little variation in ^{14}C production rates integrated over the past 25 ka using these three scaling methods (9.2 ± 0.6 at/g/yr, 9.5 ± 0.6 at/g/yr, and 9.5 ± 0.6 at/g/yr, respectively). Over the past 72 ka, however, SPICE SLHL production rates of ^{21}Ne (15.5 ± 1.0 at/g/yr; *Sf* scaling) and spallogenic ^{10}Be (3.43 ± 0.24 and 3.30 ± 0.23 at/g/yr; *Sf* and *Sa* scaling, respectively) show nominal deviation from the SLHL ^{21}Ne and $^{10}Be_{sp}$ production rates (17.0 ± 1.1 and 3.73 ± 0.26 at/g/yr (2σ)) calculated with time-independent *St* scaling factors.

The SPICE study suggests that the *St*-scaled production rates of cosmogenic ^{21}Ne and ^{10}Be can be used to calculate accurate exposure ages and erosion rates even on surfaces between 20 and 70 ka in age. If future exposure studies calculate erosion rates and exposure ages using the time-dependent *Sf*, *Sa*, or *Lm* scaling methods, particularly for landforms that are ~70 ka, then *Sf*-, *Sa*-, or *Lm*-scaled SLHL ^{21}Ne, and ^{10}Be production rates from the SPICE quartz study should be used as reference SLHL rates for these calculations. Use of the time-dependent *Sf* and *Sa* scaling methods in concert with the *Sf* and *Sa* SLHL $^{10}Be_{sp}$ production rates of Borchers et al. (2016; 4.09 and 3.92 at/g/yr), or the *Lm* scaling method in concert with the *Lm* SLHL $^{10}Be_{sp}$ production rates (CREp; 4.06 - 4.11 at/g/yr), could result in underestimated exposure ages and interpretations of erosional and/or burial effects where none are present.

Acknowledgements

We gratefully acknowledge field, laboratory, and technical support from Hella Wittmann-Oelze, Marina Ospald, Hartmut Liep, Juliane Herwig, Johannes Glodny, Shasta Marrero, Simon Merrall and Enzio Schnabel. We also thank CRONUS-EU and CRONUS-Earth colleagues, Pierre-Henri Blard, Martin Lupker, Lawrence S. Jones, and an anonymous reviewer for very helpful critical discussions and reviews. This study was funded by the Deutsche Forschungsgemeinschaft (DFG Project Reference Number FE 1418/1-1) and by GFZ Potsdam.

References

Amidon, W.H., Rood, D.H., Farley, K.A., 2009. Cosmogenic ^{3}He and ^{21}Ne production rates calibrated against ^{10}Be in minerals from the Coso volcanic field. Earth Planet. Sci. Lett. 280, 194–204. doi:10.1016/j.epsl.2009.01.031

Baksi, A. K., 1974. K–Ar study of the SP flow. Can. J. Earth Sci. 11(10), 1350-1356. doi: 10.1139/e74-131

Balco, G., 2011. Contributions and unrealized potential contributions of cosmogenic-nuclide exposure dating to glacier chronology, 1990–2010. Quat. Sci. Rev. 30(1-2), 3-27. doi: 10.1016/j.quascirev.2010.11.003

Balco, G., 2017. Feb 23, Documentation -- v3 exposure age calculator. Retrieved from https://sites.google.com/a/bgc.org/v3docs/home

Balco, G., Blard, P.-H., Shuster, D. L., Stone, J. O. H., Zimmermann, L., 2019. Cosmogenic and nucleogenic ^{21}Ne in quartz in a 28-meter sandstone core from the McMurdo Dry Valleys, Antarctica. Quat. Geochron. 52, 63-76.

Balco, G., Shuster, D.L., 2009. Production rate of cosmogenic ^{21}Ne in quartz estimated from ^{10}Be, ^{26}Al, and ^{21}Ne concentrations in slowly eroding Antarctic bedrock surfaces. Earth Planet. Sci. Lett. 281, 48–58. doi:10.1016/j.epsl.2009.02.006

Balco, G., Stone, J.O., Lifton, N.A., Dunai, T.J., 2008. A complete and easily accessible means of calculating surface exposure ages or erosion rates from ^{10}Be and ^{26}Al measurements. Quat. Geochronol. 3, 174–195. doi:10.1016/j.quageo.2007.12.001

Balco, G., Briner, J., Finkel, R.C., Rayburn, J.A., Ridge, J.C., Schaefer, J.M., 2009. Regional beryllium-10 production rate calibration for late-glacial northeastern North America. Quat. Geochronol. 4, 93–107. doi:10.1016/j.quageo.2008.09.001

Balco, G., Stone, J.O.H., Sliwinski, M.G., Todd, C., 2014. Features of the glacial history of the Transantarctic Mountains inferred from cosmogenic ^{26}Al, ^{10}Be and ^{21}Ne concentrations in bedrock surfaces. Antarct. Sci. 26, 708–723. doi:10.1017/S0954102014000261

Ballantyne, C.K., Stone, J.O., 2012. Did large ice caps persist on low ground in north-west Scotland during the Lateglacial Interstade? J. Quat. Sci. 27, 297–306. doi:10.1002/jqs.1544

Billingsley, G.H., Priest, S.S., Felger, T.J., 2007. Geologic Map of the Cameron 30' x 60' Quadrangle, Coconino County, Northern Arizona. U.S. Geol. Surv. Scientific Investigations.

Binnie, S.A., Dewald, A., Heinze, S., Voronina, E., Hein, A., Wittmann, H., von Blanckenburg, F., Hetzel, R., Christl, M., Schaller, M., Léanni, L., ASTER Team, Hippe, K., Vockenhuber, C., Ivy-Ochs, S., Maden, C., Fülöp, R.-H., Fink, D., Wilcken, K. M., Fujioka, T., Fabel, D., Freeman, S.P.H.T., Xu, S., Fifield, L.K., Akçar, N., Spiegel C., Dunai, T.J., 2019. Preliminary results of CoQtz-N: A quartz reference material for terrestrial cosmogenic ^{10}Be and ^{26}Al measurements. Nucl. Instr. Meth. Phys. Res. B. doi: 10.1016/j.nimb.2019.04.073

Binnie, S.A., Dunai, T.J., Voronina, E., Goral, T., Heinze, S., Dewald, A., 2015. Separation of Be and Al for AMS using single-step column chromatography. Nucl. Instr. Meth. Phys. Res. B 361, 397-401.

Blard, P.-H., Braucher, R., Lavé, J., Bourlès, D., 2013. Cosmogenic ^{10}Be production rate calibrated against ^{3}He in the high Tropical Andes (3800–4900 m, 20–22° S). Earth Planet. Sci. Lett. 382, 140–149. doi:10.1016/j.epsl.2013.09.010

Blard, P.-H., Lupker, M., Rousseau, M., 2019. Paired-cosmogenic nuclide paleoaltimetry. Earth Planet. Sci. Lett. 515, 271–282.

Borchers, B., Marrero, S., Balco, G., Caffee, M., Goehring, B., Lifton, N., Nishiizumi, K., Phillips, F., Schaefer, J., Stone, J., 2016. Geological calibration of spallation production rates in the CRONUS-Earth project. Quat. Geochronol. 31, 188–198. doi:10.1016/j.quageo.2015.01.009

Briner, J.P., Young, N.E., Goehring, B.M., Schaefer, J.M., 2012. Constraining Holocene ^{10}Be production rates in Greenland. J. Quat. Sci. 27, 2–6. doi:10.1002/jqs.1562

Cerling, T.E., Craig, H., 1994. Cosmogenic ^{3}He production rates from 39º N to 46º N latitude, western USA and France. Geochim. Cosmochim. Acta 58, 249-255.

Chmeleff, J., von Blanckenburg, F., Kossert, K., Jakob, D., 2010. Determination of the ^{10}Be half-life by multicollector ICP-MS and liquid scintillation counting. Nucl. Instr. Meth. Phys. Res. B 268, 192–199. doi:10.1016/j.nimb.2009.09.012

Clark, D.H., Bierman, P.R., Larsen, P., 1995. Improving in situ cosmogenic chronometers. Quat. Res. 44, 367–377. doi:10.1006/qres.1995.1081

Codilean, A.T., Fenton, C.R., Fabel, D., Bishop, P., Xu, S., 2014. Discordance between cosmogenic nuclide concentrations in amalgamated sands and individual fluvial pebbles in an arid zone catchment. Quat. Geochronol. 19, 173–180. doi:10.1016/j.quageo.2012.04.007

Decker, J.E., Niedermann, S., de Wit, M.J., 2013. Climatically influenced denudation rates of the southern African plateau: Clues to solving a geomorphic paradox. Geomorphology 190, 48–60. doi:10.1016/j.geomorph.2013.02.007

Desilets, D., Zreda, M., 2003. Spatial and temporal distribution of secondary cosmic-ray nucleon intensities and applications to in situ cosmogenic dating. Earth Planet. Sci. Lett. 206, 21–42. doi:10.1016/S0012-821X(02)01088-9

Desilets, D., Zreda, M., Prabu, T., 2006. Extended scaling factors for in situ cosmogenic nuclides: New measurements at low latitude. Earth Planet. Sci. Lett. 246, 265–276. doi:10.1016/j.epsl.2006.03.051

Dewald, A., Heinze, S., Jolie, J., Zilges, A., Dunai, T., Rethemeyer, J., Melles, M., Staubwasser, M., Kuczewski, B., Richter, J., Radtke, U., von Blanckenburg, F., Klein, M., 2013. CologneAMS, a dedicated center for accelerator mass spectrometry in Germany. Nucl. Instr. Meth. Phys. Res. B 294, 18-23.

Di Nicola, L., Strasky, S., Schlüchter, C., Salvatore, M.C., Akçar, N., Kubik, P.W., Christl, M., Kasper, H.U., Wieler, R., Baroni, C., 2009. Multiple cosmogenic nuclides document complex Pleistocene exposure history of glacial drifts in Terra Nova Bay (northern Victoria Land, Antarctica). Quat. Res. 71, 83–92. doi:10.1016/j.yqres.2008.07.004

Dugan, B., 2008. New production rate estimates for in situ cosmogenic ^{14}C from Lake Bonneville, Utah, and northwestern Scotland (Doctoral dissertation, University of Arizona).

Dugan, B., Lifton, N., Jull, A. J. T., 2008. New production rate estimates for in situ cosmogenic ^{14}C. Geochim. Cosmochim. Acta 72, A231.

Dunai, T.J., 2000. Scaling factors for production rates of in situ produced cosmogenic nuclides: a critical reevaluation. Earth Planet. Sci. Lett. 176, 157–169. doi:10.1016/S0012-821X(99)00310-6

Dunai, T.J., 2001. Influence of secular variation of the geomagnetic field on production rates of in situ produced cosmogenic nuclides. Earth Planet. Sci. Lett. 193, 197–212. doi:10.1016/S0012-821X(01)00503-9

Eberhardt, P., Eugster, O., Marti, K., 1965. A redetermination of the isotopic composition of atmospheric neon. Z. Naturforschung 20a, 623-624.

Farber, D.L., Hancock, G.S., Finkel, R.C., Rodbell, D.T., 2005. The age and extent of tropical alpine glaciation in the Cordillera Blanca, Peru. J. Quat. Sci. 20, 759–776. doi:10.1002/jqs.994

Fenton, C. R., Niedermann, S., 2014. Surface exposure dating of young basalts (1–200 ka) in the San Francisco volcanic field (Arizona, USA) using cosmogenic ^{3}He and ^{21}Ne. Quat. Geochronol. 19, 87-105. doi: 10.1016/j.quageo.2012.10.003

Fenton, C. R., Niedermann, S., Goethals, M. M., Schneider, B., Wijbrans, J., 2009. Evaluation of cosmogenic ^{3}He and ^{21}Ne production rates in olivine and pyroxene from two Pleistocene basalt flows, western Grand Canyon, AZ, USA. Quat. Geochronol. 4(6), 475-492. doi: 10.1016/j.quageo.2009.08.002

Fenton, C.R., Hermanns, R.L., Blikra, L.H., Kubik, P.W., Bryant, C., Niedermann, S., Meixner, A., Goethals, M.M., 2011. Regional ^{10}Be production rate calibration for the past 12 ka deduced from the radiocarbon-dated Grøtlandsura and Russenes rock avalanches at 69° N, Norway. Quat. Geochronol. 6, 437–452. doi:10.1016/j.quageo.2011.04.005

Fenton, C. R., Mark, D. F., Barfod, D. N., Niedermann, S., Goethals, M. M., Stuart, F. M., 2013. ^{40}Ar/^{39}Ar dating of the SP and Bar Ten lava flows AZ, USA: laying the foundation for the SPICE cosmogenic nuclide production-rate calibration project. Quat. Geochronol. 18, 158-172. doi: 10.1016/j.quageo.2013.01.007

Fülöp, R.-H., Wacker, L., Dunai, T. J., 2015. Progress report on a novel in situ ^{14}C extraction scheme at the University of Cologne. Nucl. Instr. Meth. Phys. Res. B 361, 20-24.

Gibbon, R. J., Granger, D. E., Kuman, K., Partridge, T. C., 2009. Early Acheulean technology in the Rietputs Formation, South Africa, dated with cosmogenic nuclides. J. of Hum. Evol. 56, 152-160. doi: 10.1016/j.jhevol.2008.09.006

Gibbon, R. J., Pickering, T. R., Sutton, M. B., Heaton, J. L., Kuman, K., Clarke, R. J., Brain, C.K., Granger, D. E., 2014. Cosmogenic nuclide burial dating of hominin-bearing Pleistocene cave deposits at Swartkrans, South Africa. Quat. Geochronol. 24, 10-15. doi: 10.1016/j.quageo.2014.07.004

Goehring, B. M., Kurz, M. D., Balco, G., Schaefer, J. M., Licciardi, J., Lifton, N., 2010. A reevaluation of in situ cosmogenic ^{3}He production rates. Quat. Geochronol. 5(4), 410-418. doi: 10.1016/j.quageo.2010.03.001

Goehring, B.M., Lohne, Ø.S., Mangerud, J., Svendsen, J.I., Gyllencreutz, R., Schaefer, J., Finkel, R., 2012. Late Glacial and Holocene ^{10}Be production rates for western Norway. J. Quat. Sci. 27, 89–96. doi:10.1002/jqs.1517

Goethals, M.M., Hetzel, R., Niedermann, S., Wittmann, H., Fenton, C.R., Kubik, P.W., Christl, M., von Blanckenburg, F., 2009. An improved experimental determination of cosmogenic ^{10}Be/^{21}Ne and ^{26}Al/^{21}Ne production ratios in quartz. Earth Planet. Sci. Lett. 284, 187–198. doi:10.1016/j.epsl.2009.04.027

Gosse, J. C., Phillips, F. M., 2001. Terrestrial in situ cosmogenic nuclides: theory and application. Quat. Sci. Rev. 20(14), 1475-1560. doi: 10.1016/S0277-3791(00)00171-2

Gosse, J.C., Evenson, E.B., Klein, J., Lawn, B., Middleton, R., 1995. Precise cosmogenic ^{10}Be measurements in western North America: Support for a global Younger Dryas cooling event. Geology 23, 877–880. doi:10.1130/0091-7613(1995)023<0877:PCBMIW>2.3.CO;2

Heisinger, B., Lal, D., Jull, A.J.T., Kubik, P., Ivy-Ochs, S., Knie, K., Nolte, E., 2002a. Production of selected cosmogenic radionuclides by muons: 2. Capture of negative muons. Earth Planet. Sci. Lett. 200 (3–4), 357–369. doi: 10.1016/S0012-821X(02)00641-6

Heisinger, B., Lal, D., Jull, A.J.T., Kubik, P., Ivy-Ochs, S., Neumaier, S., Knie, K., Lazarev, V., Nolte, E., 2002b. Production of selected cosmogenic radionuclides by muons 1. Fast muons. Earth Planet. Sci. Lett. 200 (3–4), 345–355. doi: 10.1016/S0012-821X(02)00640-4

Hetzel, R., Niedermann, S., Ivy-Ochs, S., Kubik, P. W., Tao, M., Gao, B., 2002. ^{21}Ne versus ^{10}Be and ^{26}Al exposure ages of fluvial terraces: the influence of crustal Ne in quartz. Earth Planet. Sci. Lett. 201, 575-591.

Heyman, J., 2014. Paleoglaciation of the Tibetan Plateau and surrounding mountains based on exposure ages and ELA depression estimates. Quat. Sci. Rev. 91, 30–41. doi:10.1016/j.quascirev.2014.03.018

Honda, M., Zhang, X., Phillips, D., Hamilton, D., Deerberg, M., Schwieters, J. B., 2015. Redetermination of the ^{21}Ne relative abundance of the atmosphere, using a high resolution, multi-collector noble gas mass spectrometer (HELIX-MC Plus). Int. J. Mass Spectrom. 387, 1-7.

Ivy-Ochs, S., Kerschner, H., Reuther, A., Maisch, M., Sailer, R., Schaefer, J., Kubik, P.W., Synal, H.-A., Schlüchter, C., 2006. The timing of glacier advances in the northern European Alps based on surface exposure dating with cosmogenic ^{10}Be, ^{26}Al, ^{36}Cl, and ^{21}Ne. Geol. Soc. Am. Spec. Pap. 415, 43–60. doi:10.1130/2006.2415(04)

Ivy-Ochs, S., Kober, F., Alfimov, V., Kubik, P.W., Synal, H.-A., 2007. Cosmogenic ^{10}Be, ^{21}Ne and ^{36}Cl in sanidine and quartz from Chilean ignimbrites. Nucl. Instr. Meth. Phys. Res. B 259, 588–594. doi:10.1016/j.nimb.2007.03.001

Jull, A. T., Scott, E. M., Bierman, P., 2015. The CRONUS-Earth inter-comparison for cosmogenic isotope analysis. Quat. Geochron. 26, 3-10.

Kaplan, M.R., Strelin, J.A., Schaefer, J.M., Denton, G.H., Finkel, R.C., Schwartz, R., Putnam, A.E., Vandergoes, M.J., Goehring, B.M., Travis, S.G., 2011. In-situ cosmogenic ^{10}Be production rate at Lago Argentino, Patagonia: Implications for late-glacial climate chronology. Earth Planet. Sci. Lett. 309, 21–32. doi:10.1016/j.epsl.2011.06.018

Kelly, M.A., Lowell, T.V., Applegate, P.J., Phillips, F.M., Schaefer, J.M., Smith, C.A., Kim, H., Leonard, K.C., Hudson, A.M., 2015. A locally calibrated, late glacial ^{10}Be production rate from a low-latitude, high-altitude site in the Peruvian Andes. Quat. Geochronol. 26, 70–85. doi:10.1016/j.quageo.2013.10.007

Kober, F., Ivy-Ochs, S., Schlunegger, F., Baur, H., Kubik, P. W., Wieler, R., 2007. Denudation rates and a topography-driven rainfall threshold in northern Chile: Multiple cosmogenic nuclide data and sediment yield budgets. Geomorphology 83, 97-120.

Kober, F., Alfimov, V., Ivy-Ochs, S., Kubik, P.W., Wieler, R., 2011. The cosmogenic ^{21}Ne production rate in quartz evaluated on a large set of existing ^{21}Ne–^{10}Be data. Earth Planet. Sci. Lett. 302, 163–171. doi:10.1016/j.epsl.2010.12.008

Kohl, C. P., Nishiizumi, K., 1992. Chemical isolation of quartz for measurement of in situ-produced cosmogenic nuclides. Geochim. Cosmochim. Acta 56, 3583-3587.

Korschinek, G., Bergmaier, A., Faestermann, T., Gerstmann, U.C., Knie, K., Rugel, G., Wallner, A., Dillmann, I., Dollinger, G., Lierse von Gostomski, C., Kossert, K., Maiti, M., Poutivtsev, M., Remmert, A., 2010. A new value for the half-life of ^{10}Be by Heavy-Ion Elastic Recoil Detection and liquid scintillation counting. Nucl. Instr. Meth. Phys. Res. B 268, 187–191. doi:10.1016/j.nimb.2009.09.020

Kounov, A., Niedermann, S., de Wit, M.J., Codilean, A.T., Viola, G., Andreoli, M., Christl, M., 2015. Cosmogenic ^{21}Ne and ^{10}Be reveal a more than 2 Ma alluvial fan flanking the Cape Mountains, South Africa. South Afr. J. Geol. 118, 129–144. doi:10.2113/gssajg.118.2.129

Kubik, P.W., Ivy-Ochs, S., 2004. A re-evaluation of the 0–10 ka ^{10}Be production rate for exposure dating obtained from the Köfels (Austria) landslide. Nucl. Instr. Meth. Phys. Res. B 223–224, 618–622. doi:10.1016/j.nimb.2004.04.114

Kubik, P.W., Ivy-Ochs, S., Masarik, J., Frank, M., Schlüchter, C., 1998.^{10}Be and ^{26}Al production rates deduced from an instantaneous event within the dendro-calibration curve, the landslide of Köfels, Ötz Valley, Austria. Earth Planet. Sci. Lett. 161, 231-241.

Laj, C., Kissel, C., Beer, J., 2004. High resolution global paleointensity stack since 75 kyr (GLOPIS-75) calibrated to absolute values. Timescales Paleomagn. F. Geophys. Monogr. Ser. 145, 255-265. doi: 10.1029/145GM19

Lal, D., 1991. Cosmic ray labeling of erosion surfaces: in situ nuclide production rates and erosion models. Earth Planet. Sci. Lett. 104, 424–439. doi:10.1016/0012-821X(91)90220-C

Larsen, P., 1996. In-situ production rates of cosmogenic ^{10}Be and ^{26}Al over the past 21,500 years determined from the terminal moraine of the Laurentide Ice Sheet, north-central New Jersey. PhD thesis, University of Vermont.

Lifton, N.A., 2016. Implications of two Holocene time-dependent geomagnetic models for cosmogenic nuclide production rate scaling. Earth Planet. Sci. Lett. 433, 257-268. doi: 10.1016/j.epsl.2015.11.006

Lifton, N.A., Jull, A.J.T, Quade, J., 2001. A new extraction technique and production rate estimate for in situ cosmogenic ^{14}C in quartz. Geochim. Cosmochim. Acta 65, 1953-1969.

Lifton, N.A., Bieber, J.W., Clem, J.M., Duldig, M.L., Evenson, P., Humble, J.E., Pyle, R., 2005. Addressing solar modulation and long-term uncertainties in scaling secondary cosmic rays for in situ cosmogenic nuclide applications. Earth Planet. Sci. Lett. 239, 140–161. doi:10.1016/j.epsl.2005.07.001

Lifton, N., Sato, T., Dunai, T.J., 2014. Scaling in situ cosmogenic nuclide production rates using analytical approximations to atmospheric cosmic-ray fluxes. Earth Planet. Sci. Lett. 386, 149–160. doi:10.1016/j.epsl.2013.10.052

Lifton, N., Caffee, M., Finkel, R., Marrero, S., Nishiizumi, K., Phillips, F.M., Goehring, B., Gosse, J., Stone, J., Schaefer, J., Theriault, B., Jull, A.J.T., Fifield, K., 2015. In situ cosmogenic nuclide production rate calibration for the CRONUS-Earth project from Lake Bonneville, Utah, shoreline features. Quat. Geochronol. 26, 56–69. doi:10.1016/j.quageo.2014.11.002

Luna, L. V., Bookhagen, B., Niedermann, S., Rugel, G., Scharf, A., Merchel, S., 2018. Glacial chronology and production rate cross-calibration of five cosmogenic nuclide and mineral systems from the southern Central Andean Plateau. Earth Planet. Sci. Lett. 500, 242-253.

Lupker, M., Hippe, K., Wacker, L., Kober, F., Maden, C., Braucher, R., Bourlès, D., Vidal Romani, J.R., Wieler, R., 2015. Depth-dependence of the production rate of in situ ^{14}C in quartz from the Leymon High core, Spain. Quat. Geochronol. 28, 80-87. doi: 10.1016/j.quageo.2015.04.004

Ma, Y., Wu, Y., Li, D., Zheng, D., Zheng, W., Zhang, H., Pang, J., Wang, Y., 2016. Erosion rate in the Shapotou area, northwestern China, constrained by in situ-produced cosmogenic ^{21}Ne in long-exposed erosional surfaces. Quat. Geochronol. 31, 3–11. doi:10.1016/j.quageo.2015.10.001

Marrero, S. M., Phillips, F. M., Borchers, B., Lifton, N., Aumer, R., Balco, G., 2016. Cosmogenic nuclide systematics and the CRONUScalc program. Quat. Geochronol. 31, 160-187. doi: 10.1016/j.quageo.2015.09.005

Martin, L.C.P., Blard, P.-H., Lavé, J., Braucher, R., Lupker, M., Condom, T., Charreau, J., Mariotti, V., ASTER Team, Davy, E., 2015. In situ cosmogenic ^{10}Be production rate in the High Tropical Andes. Quat. Geochronol. 30, 54–68. doi:10.1016/j.quageo.2015.06.012

Martin, L. C. P., Blard, P.-H., Balco, G., Lavé, J., Delunel, R., Lifton, N., Laurent, V., 2017. The CREp program and the ICE-D production rate calibration database: a fully parameterizable and updated online tool to compute cosmic-ray exposure ages. Quat. Geochronol. 38, 25-49. doi: 10.1016/j.quageo.2016.11.006

Matmon, A., Fink, D., Davis, M., Niedermann, S., Rood, D., Frumkin, A., 2014. Unraveling rift margin evolution and escarpment development ages along the Dead Sea fault using cosmogenic burial ages. Quat. Res. 82, 281–295. doi:10.1016/j.yqres.2014.04.008

McFadden, L. D., McDonald, E. V., Wells, S. G., Anderson, K., Quade, J., Forman, S. L., 1998. The vesicular layer and carbonate collars of desert soils and pavements: formation, age and relation to climate change. Geomorphology 24, 101-145. doi: 10.1016/S0169-555X(97)00095-0

McPhillips, D., Hoke, G.D., Liu-Zeng, J., Bierman, P.R., Rood, D.H., Niedermann, S., 2016. Dating the incision of the Yangtze River gorge at the First Bend using three-nuclide burial ages. Geophys. Res. Lett. 43, 101-110. doi:10.1002/2015GL066780

Miller, G. H., Briner, J. P., Lifton, N. A., Finkel, R. C., 2006. Limited ice-sheet erosion and complex exposure histories derived from in situ cosmogenic ^{10}Be, ^{26}Al, and ^{14}C on Baffin Island, Arctic Canada. Quat. Geochronol. 1, 74-85. doi: 10.1016/j.quageo.2006.06.011

Muscheler, R., Beer, J., Kubik, P. W., Synal, H. A., 2005. Geomagnetic field intensity during the last 60,000 years based on ^{10}Be and ^{36}Cl from the Summit ice cores and ^{14}C. Quat. Sci. Rev. 24, 1849-1860. doi: 10.1016/j.quascirev.2005.01.012

Niedermann, S., 2000. The ^{21}Ne production rate in quartz revisited. Earth Planet. Sci. Lett. 183, 361–364. doi:10.1016/S0012-821X(00)00302-2

Niedermann, S., 2002. Cosmic-ray-produced noble gases in terrestrial rocks: Dating tools for surface processes. Rev. Mineral. Geochem. 47, 731–784. doi:10.2138/rmg.2002.47.16

Niedermann, S., Graf, T., Marti, K., 1993. Mass spectrometric identification of cosmic-ray-produced neon in terrestrial rocks with multiple neon components. Earth Planet. Sci. Lett. 118, 65-73.

Niedermann, S., Graf, T., Kim, J.S., Kohl, C.P., Marti, K., Nishiizumi, K., 1994. Cosmic-ray-produced ^{21}Ne in terrestrial quartz: The neon inventory of Sierra Nevada quartz separates. Earth Planet. Sci. Lett. 125, 341–355.

Niedermann, S., Bach, W., Erzinger, J., 1997. Noble gas evidence for a lower mantle component in MORBs from the southern East Pacific Rise: decoupling of helium and neon isotope systematics. Geochim. Cosmochim. Acta 61, 2697–2715.

Nishiizumi, K., Winterer, E.L., Kohl, C.P., Klein, J., Middleton, R., Lal, D., Arnold, J.R., 1989. Cosmic ray production rates of ^{10}Be and ^{26}Al in quartz from glacially polished rocks. J. Geophys. Res. 94, 17907–17915. doi:10.1029/JB094iB12p17907

Nishiizumi, K., Imamura, M., Caffee, M.W., Southon, J.R., Finkel, R.C., McAninch, J., 2007. Absolute calibration of ^{10}Be AMS standards. Nucl. Instr. Meth. Phys. Res. B 258, 403–413. doi:10.1016/j.nimb.2007.01.297

Pavićević, M.K., Cvetković, V., Niedermann, S., Pejović, V., Amthauer, G., Boev, B., Bosch, F., Aničin, I., Henning, W.F., 2016. Erosion rate study at the Allchar deposit (Macedonia) based on radioactive and stable cosmogenic nuclides (^{26}Al, ^{36}Cl, ^{3}He, and ^{21}Ne). Geochem. Geophys. Geosyst. 17, 410–424. doi:10.1002/2015GC006054

Pavón-Carrasco, F.J., Osete, M.L., Torta, J.M., De Santis, A., 2014. A geomagnetic field model for the Holocene based on archaeomagnetic and lava flow data. Earth Planet. Sci. Lett. 388, 98-109.

Phillips, F. M., 2016. Cosmogenic nuclide data sets from the Sierra Nevada, California, for assessment of nuclide production models: I. Late Pleistocene glacial chronology. Quat. Geochronol. 35, 119-129. doi:10.1016/j.quageo.2015.12.003

Phillips, F.M., Argento, D.C., Bourlès, D.L., Caffee, M.W., Dunai, T.J., Goehring, B., Gosse, J.C., Hudson, A.M., Jull, A.J.T., Kelly, M., Lifton, N., Marrero, S.M., Nishiizumi, K., Reedy, R.C., Stone, J.O.H., 2016. Where now? Reflections on future directions for cosmogenic nuclide research from the CRONUS Projects. Quat. Geochronol. 31, 155–159. doi:10.1016/j.quageo.2015.04.010

Phillips, W.M., McDonald, E.V., Reneau, S.L., Poths, J., 1998. Dating soils and alluvium with cosmogenic ^{21}Ne depth profiles: case studies from the Pajarito Plateau, New Mexico, USA. Earth Planet. Sci. Lett. 160, 209–223. doi:10.1016/S0012-821X(98)00076-4

Pigati, J. S., 2004. Experimental developments and application of carbon-14 and in situ cosmogenic nuclide dating techniques. Doctoral dissertation, University of Arizona.
Putnam, A.E., Schaefer, J.M., Barrell, D.J.A., Vandergoes, M., Denton, G.H., Kaplan, M.R., Finkel, R.C., Schwartz, R., Goehring, B.M., Kelley, S.E., 2010. In situ cosmogenic ^{10}Be production-rate calibration from the Southern Alps, New Zealand. Quat. Geochronol. 5, 392–409. doi:10.1016/j.quageo.2009.12.001
Putnam, A. E., Bromley, G. R., Rademaker, K., Schaefer, J. M., 2019. In situ ^{10}Be production-rate calibration from a ^{14}C-dated late-glacial moraine belt in Rannoch Moor, central Scottish Highlands. Quaternary Geochronology, 50, 109-125.
Renne, P. R., Mundil, R., Balco, G., Min, K., Ludwig, K. R., 2010. Joint determination of ^{40}K decay constants and ^{40}Ar*/^{40}K for the Fish Canyon sanidine standard, and improved accuracy for ^{40}Ar/^{39}Ar geochronology. Geochim. Cosmochim. Acta 74, 5349-5367.
Rittenour, T. M., Riggs, N. R., Kennedy, L. E., 2012. Application of single-grain OSL to date quartz xenocrysts within a basalt flow, San Francisco volcanic field, northern Arizona, USA. Quat. Geochronol. 10, 300-307. doi: 10.1016/j.quageo.2012.02.002
Schäfer, J.M., Ivy-Ochs, S., Wieler, R., Leya, I., Baur, H., Denton, G.H., Schlüchter, C., 1999. Cosmogenic noble gas studies in the oldest landscape on earth: surface exposure ages of the Dry Valleys, Antarctica. Earth Planet. Sci. Lett. 167, 215–226. doi:10.1016/S0012-821X(99)00029-1
Schimmelpfennig, I., Schaefer, J.M., Goehring, B.M., Lifton, N., Putnam, A.E., Barrell, D.A., 2012. Calibration of the in situ cosmogenic ^{14}C production rate in New Zealand's Southern Alps. J. Quat. Sci. 27, 671-674. doi: 10.1016/j.quageo.2011.05.002
Sims, K.W., Ackert Jr, R.P., Ramos, F.C., Sohn, R.A., Murrell, M.T., DePaolo, D.J., 2007. Determining eruption ages and erosion rates of Quaternary basaltic volcanism from combined U-series disequilibria and cosmogenic exposure ages. Geology 35, 471-474.
Small, D., Fabel, D., 2015. A Lateglacial ^{10}Be production rate from glacial lake shorelines in Scotland. J. Quat. Sci. 30, 509-513.
Stolz, A., Dewald, A., Altenkirch, R., Herb, S., Heinze, S., Schiffer, M., Dunai, T., 2017. Radiocarbon measurements of small gaseous samples at CologneAMS. Nucl. Instr. Meth. Phys. Res. B 406, 283-286.
Stone, J.O., 2000. Air pressure and cosmogenic isotope production. J. Geophys. Res. 105, 23753–23759. doi:10.1029/2000JB900181
Stone, J.O., Ballantyne, C.K., Fifield, L.K., 1998. Exposure dating and validation of periglacial weathering limits, northwest Scotland. Geology 26, 587–590. doi:10.1130/0091-7613(1998)026<0587:EDAVOP>2.3.CO;2
Stone, J., Fifield, K., Beer, J., Vonmoos, M., Obrist, C., Grajcar, M., Kubik, P., Muscheler, R., Finkel, R., Caffee, M., 2004. Co-precipitated silver–metal oxide aggregates for accelerator mass spectrometry of ^{10}Be and ^{26}Al. Nucl. Instr. Meth. Phys. Res. B 223-224, 272–277.
Strobl, M., Hetzel, R., Niedermann, S., Ding, L., Zhang, L., 2012. Landscape evolution of a bedrock peneplain on the southern Tibetan Plateau revealed by in situ-produced cosmogenic ^{10}Be and ^{21}Ne. Geomorphology 153–154, 192–204. doi:10.1016/j.geomorph.2012.02.024

Stroeven, A.P., Heyman, J., Fabel, D., Björck, S., Caffee, M.W., Fredin, O., Harbor, J.M., 2015. A new Scandinavian reference ^{10}Be production rate. Quat. Geochronol. 29, 104–115. doi:10.1016/j.quageo.2015.06.011

Summerfield, M.A., Stuart, F.M., Cockburn, H.A.P., Sugden, D.E., Denton, G.H., Dunai, T., Marchant, D.R., 1999. Long-term rates of denudation in the Dry Valleys, Transantarctic Mountains, southern Victoria Land, Antarctica based on in-situ-produced cosmogenic ^{21}Ne. Geomorphology 27, 113–129. doi:10.1016/S0169-555X(98)00093-2

Tschudi, S., Schäfer, J.M., Zhao, Z., Wu, X., Ivy-Ochs, S., Kubik, P.W., Schlüchter, C., 2003. Glacial advances in Tibet during the Younger Dryas? Evidence from cosmogenic ^{10}Be, ^{26}Al, and ^{21}Ne. J. Asian Earth Sci. 22, 301–306. doi:10.1016/S1367-9120(03)00035-X

Uppala, S. M., Kållberg, P. W., Simmons, A. J., Andrae, U., Bechtold, V. D. C., Fiorino, M., et al., 2005. The ERA-40 re- analysis. Q. J. Royal Meteorol. Soc. 131, 2961-3012.

Valet, J. P., Meynadier, L., Guyodo, Y., 2005. Geomagnetic dipole strength and reversal rate over the past two million years. Nature 435, 802-805.

Vermeesch, P., 2007. CosmoCalc: An Excel add-in for cosmogenic nuclide calculations. Geochem. Geophys. Geosyst. 8(8). doi: 10.1029/2006GC001530

Vermeesch, P., Baur, H., Heber, V.S., Kober, F., Oberholzer, P., Schaefer, J.M., Schlüchter, C., Strasky, S., Wieler, R., 2009. Cosmogenic ^{3}He and ^{21}Ne measured in quartz targets after one year of exposure in the Swiss Alps. Earth Planet. Sci. Lett. 284, 417–425. doi:10.1016/j.epsl.2009.05.007

Ward, G. K.,Wilson, S. R., 1978. Procedures for comparing and combining radiocarbon age determinations: a critique. Archaeometry 20, 19-31.

Young, N. E., Schaefer, J. M., Briner, J. P., Goehring, B. M., 2013. A ^{10}Be production-rate calibration for the Arctic. J. Quat. Sci. 28(5), 515-526. doi: 10.1002/jqs.2642

Young, N.E., Schaefer, J.M., Goehring, B., Lifton, N., Schimmelpfennig, I., Briner, J.P., 2014. West Greenland and global in situ ^{14}C production-rate calibrations. J. Quat. Sci. 29, 401–406. doi:10.1002/jqs.2717

Ziegler, L.B., Constable, C.G., Johnson, C.L., Tauxe, L., 2011. PADM2M: a penalized maximum likelihood model of the 0-2 Ma palaeomagnetic axial dipole moment. Geophys. J. Int. 184, 1069-1089. doi: 10.1111/j.1365-246X.2010.04905.x

Appendix A

A. Methods

A1. Acid-etching and concentration of quartz separates

Quartz concentrates were initially treated without heat in 100 ml 10% HNO_3, to dissolve any carbonate that was still present. This step was followed by several leaching steps in dilute HF/HNO_3 in Nalgene bottles. The quartz samples were gently rolled in bottles placed on hot-dog rollers, kept at room temperature or heated up to 80°C. These leaching steps remove feldspars, zeolites, and meteoric ^{10}Be from quartz surfaces and reduce contributions of nucleogenic ^{21}Ne, which may be produced when alpha particles are ejected from neighboring U/Th-rich minerals and react with ^{18}O in the quartz (e.g. Niedermann, 2002).

Acid-etching continued until >25% of the original quartz mass was dissolved, and Al concentrations were <100 ppm, indicating most, if not all, Al-bearing minerals had been removed from the quartz samples. For samples that contained enough quartz mass, three separate aliquots were taken from each of the “purified” quartz samples. The aliquots were then used for ^{10}Be, in-situ ^{14}C, and ^{21}Ne analyses (by AMS or noble gas mass spectrometry). Samples were also prepared for ^{26}Al AMS analysis; measurements are still pending.

A2. Ne extraction and noble gas mass spectrometric analysis

Prior to loading for mass spectrometric analysis, most quartz samples were ground to ~100 μm in an agate mill in order to open part of the fluid inclusions, thereby reducing the contribution of trapped Ne. For 10SPC01 and 10SPC06 the 125-500 μm fraction was used without further crushing. Samples of 0.46 to 0.81 g (Table 1) were then washed in acetone, dried by heating at ~90°C overnight, wrapped in Al foil, and finally loaded into the sample carrousel above the extraction furnace. The carrousel was baked at 100°C for approximately one week. Noble gases were extracted by stepwise heating (at 400, 800, and 1200°C, with an additional 600°C step for samples SPICE-A3 and 10SPC07) for 20 minutes each. In addition, aliquots of samples SPICE-A4 and –A8 were crushed in vacuo to determine the isotopic composition of Ne released from fluid inclusions; the crushed material was afterwards retrieved and used for stepwise heating extraction. After gas extraction by either heating or crushing, chemically active gases were removed in two Ti sponge and two SAES (ZrAl) getters, Ar, Kr and Xe were trapped in either an activated charcoal trap at 77 K or on a stainless steel frit at 50 K, and He and Ne were separated from each other in an activated charcoal cryogenic adsorber at 35 K. Noble gas concentrations and isotopic compositions were determined in a VG5400 sector field mass spectrometer, and were corrected for isobaric interferences, instrumental mass fractionation, and analytical blanks.

Table SD1. ^{4}He and ^{20}Ne concentrations (cm^3 STP/g), Ne isotope ratios and excess ^{21}Ne ($^{21}Ne_{ex}$) concentrations (10^6 at/g) for stepwise heating extractions of quartz samples from SP Flow, Arizona. Data from crushing extractions of samples SPICE-A4 and –A8 are shown as well. Error limits are 2σ.

Sample Weight	T *°C*	^{4}He *10^{-8} cm^3/g*	^{20}Ne *10^{-12} cm^3/g*	^{22}Ne/^{20}Ne *10^{-2}*	^{21}Ne/^{20}Ne *10^{-2}*	$^{21}Ne_{ex}$[a] *10^6 at/g*
SPICE-A1	400	-	44.1	10.67	0.516	2.60
0.48040 g			±2.5	±0.19	±0.025	±0.32
	800	-	40.6	10.30	0.412	1.27
			±2.5	±0.22	±0.022	±0.25
	1200	-	0.43	9.1	0.71	0.047
			$^{+0.56}_{-0.43}$	±4.9	±0.55	±0.022
	Total	-	85.1	10.49	0.467	3.87
			±3.6	±0.15	±0.017	±0.41
SPICE-A2	400	-	37.4	10.50	0.477	1.82
0.47372 g			±2.2	±0.23	±0.020	±0.22
	800	-	31.3	10.76	0.576	2.35
			±2.1	±0.24	±0.038	±0.34
	1200	-	0.31	11.0	0.59	0.024
			$^{+0.65}_{-0.31}$	±5.3	$^{+0.98}_{-0.59}$	$^{+0.063}_{-0.024}$
	Total	-	69.0	10.62	0.522	4.17
			±3.1	±0.17	±0.021	±0.40
SPICE-A3	400	0.0126	51.9	10.74	0.508	2.95
0.48278 g		±0.0014	±2.8	±0.10	±0.021	±0.32
	600	0.0286	4.67	10.87	0.92	0.786
		±0.0021	±0.72	±0.35	±0.11	±0.097
	800	0.0059	4.29	10.19	0.367	0.082
		±0.0013	±0.92	±0.53	±0.053	±0.059
	1200	0.0018	1.17	11.5	0.42	0.101
		$^{+0.0045}_{-0.0018}$	±0.66	±1.1	±0.24	±0.060
	Total	0.0489	62.0	10.73	0.528	3.82
		$^{+0.0053}_{-0.0034}$	±3.1	±0.10	±0.021	±0.34
SPICE-A4	Crushed	0.01505	5.84	10.41	0.315	-
1.00778 g		±0.00092	±0.34	±0.34	±0.022	
0.80032 g	400	-	0.55	19.5	8.4	1.20
			±0.39	±6.5	±5.7	±0.16
	800	-	11.93	11.30	1.098	2.57
			±0.87	±0.18	±0.059	±0.21
	1200	-	7.28	10.63	0.328	0.063
			±0.60	±0.37	±0.032	±0.063
	Total	-	19.8	11.28	1.02	3.77
			±1.1	±0.30	±0.22	±0.26

Table SD1 (cont.)

Sample Weight	T *°C*	^{4}He *10^{-8} cm^3/g*	^{20}Ne *10^{-12} cm^3/g*	^{22}Ne/^{20}Ne *10^{-2}*	^{21}Ne/^{20}Ne *10^{-2}*	^{21}Ne$_{ex}$ *10^6 at/g*
SPICE-A5	400	-	44.0	10.59	0.447	1.78
0.48470 g			±2.5	±0.21	±0.025	±0.31
	800	-	25.7	10.97	0.588	2.01
			±1.7	±0.28	±0.037	±0.27
	1200	-	0.14	7	1.0	0.026
			$^{+0.63}_{-0.14}$	$^{+19}_{-7}$	$^{+3.6}_{-1.0}$	$^{+0.043}_{-0.026}$
	Total	-	69.8	10.72	0.500	3.80
			±3.1	±0.18	±0.023	±0.41
SPICE-A6	400	0.0096	50.4	10.60	0.492	2.66
0.48494 g		±0.0017	±2.7	±0.13	±0.026	±0.37
	800	0.857	10.2	10.56	0.635	0.92
		±0.043	±1.1	±0.47	±0.058	±0.15
	1200	0.262	0.39	10.3	0.55	0.068
		±0.014	$^{+0.66}_{-0.39}$	±5.4	±0.49	±0.024
	Total	1.129	61.0	10.59	0.516	3.56
		±0.045	±3.0	±0.14	±0.024	±0.40
SPICE-A7	400	0.0062	64.2	10.54	0.466	2.94
0.47508 g		±0.0018	±3.4	±0.13	±0.025	±0.45
	800	0.674	6.54	10.45	0.699	0.71
		±0.034	±0.99	±0.76	±0.078	±0.11
	1200	0.0120	0.56	10.3	0.28	0.035
		±0.0022	$^{+0.66}_{-0.56}$	±3.6	$^{+0.45}_{-0.28}$	$^{+0.059}_{-0.035}$
	Total	0.692	71.3	10.53	0.486	3.65
		±0.034	±3.6	±0.14	±0.024	±0.46
SPICE-A8	Crushed	0.0753	23.6	10.04	0.297	-
1.00802 g		±0.0039	±1.8	±0.17	±0.025	
0.80998 g	400	-	1.10	11.5	1.93	0.483
			±0.40	±1.4	±0.61	±0.080
	800	-	57.7	10.29	0.530	3.62
			±3.1	±0.19	±0.017	±0.33
	1200	-	19.3	9.93	0.321	0.13
			±1.1	±0.24	±0.038	$^{+0.20}_{-0.13}$
	Total	-	78.1	10.22	0.498	4.11
			±3.3	±0.15	±0.020	±0.34
SPICE-A9	400	0.0148	55.8	10.68	0.498	3.03
0.46248 g		±0.0019	±3.0	±0.15	±0.036	±0.56
	800	1.167	11.8	10.34	0.539	0.77
		±0.059	±1.2	±0.35	±0.064	±0.20
	1200	0.0215	0.81	9.1	0.38	0.032
		±0.0029	±0.68	±2.5	±0.26	$^{+0.054}_{-0.032}$
	Total	1.203	68.4	10.60	0.504	3.80
		±0.059	±3.3	±0.14	±0.032	±0.60

Table SD1 (cont.)

Sample Weight	T *°C*	^{4}He *10^{-8} cm^3/g*	^{20}Ne *10^{-12} cm^3/g*	^{22}Ne/^{20}Ne *10^{-2}*	^{21}Ne/^{20}Ne *10^{-2}*	^{21}Ne$_{ex}$ *10^6 at/g*
SPICE-A10	400	-	28.3	10.39	0.444	1.12

0.48178 g			±1.7	±0.23	±0.034	±0.26
	800	-	38.3	10.71	0.600	3.12
			±2.4	±0.20	±0.018	±0.24
	1200	-	0.85	8.5	0.36	0.013
			±0.65	±3.0	±0.27	$^{+0.062}_{-0.013}$
	Total	-	67.5	10.55	0.532	4.24
			±3.0	±0.16	±0.018	±0.36
10SPC01	400	0.0034	4.07	10.21	0.53	0.26
0.52770 g		±0.0016	±0.71	±0.42	±0.10	±0.10
	800	0.246	36.9	10.43	0.686	3.86
		±0.012	±2.5	±0.16	±0.036	±0.42
	1200	0.0384	19.0	10.00	0.299	0.01
		±0.0041	±1.4	±0.17	±0.045	$^{+0.23}_{-0.01}$
	Total	0.288	60.0	10.28	0.553	4.12
		±0.013	±3.0	±0.12	±0.028	±0.43
10SPC06	400	0.0019	1.29	11.9	2.8	0.86
0.50342 g		±0.0017	±0.65	±1.1	±1.3	±0.17
	800	0.195	22.6	10.37	0.754	2.79
		±0.010	±1.8	±0.33	±0.030	±0.22
	1200	0.186	7.82	9.87	0.323	0.056
		±0.010	±0.87	±0.58	±0.039	$^{+0.083}_{-0.056}$
	Total	0.383	31.7	10.31	0.731	3.65
		±0.014	±2.1	±0.28	±0.073	±0.28
10SPC07	400	0.225	73.8	10.48	0.4446	2.95
0.73352 g		±0.012	±4.3	±0.12	±0.0082	±0.23
	600	7.94	21.1	10.94	0.514	1.24
		±0.40	±1.3	±0.15	±0.023	±0.15
	800	7.03	39.3	10.35	0.309	0.13
		±0.35	±2.5	±0.11	±0.020	$^{0.21}_{-0.13}$
	1200	1.172	10.11	10.56	0.395	0.269
		±0.059	±0.80	±0.21	±0.036	±0.099
	Total	16.37	144.3	10.52	0.4143	4.32
		±0.53	±5.2	±0.07	±0.0084	$^{+0.35}_{-0.30}$

[a] $^{21}Ne_{ex}$ was calculated relative to the atmospheic $^{21}Ne/^{20}Ne$ ratio of 0.002959 (Eberhardt et al., 1965). $^{21}Ne_{ex}$ contributions from 1200°C steps are generally small and are not included in totals (Niedermann, 2002).

Table SD2. Measured cosmogenic ^{10}Be concentrations in SPICE quartz samples and associated laboratory blanks. All AMS measurements were made at the University of Cologne.

Sample ID	Quartz mass (g)	^{9}Be added in spike (10^{19} atoms)	$^{10}Be/^{9}Be$ (10^{-13}) [a]	2σ uncertainty (10^{-13}) [a]	Blank corrected ^{10}Be concentration (10^{5} at/g)[b]	2σ uncertainty (10^{5} at/g)[b]	2σ uncertainty (%)	Error-weighted mean ^{10}Be concentration (10^{5} at/g)[c]	2σ uncertainty (10^{5} at/g)[c]
SPICE-A1	2.1608	1.691	1.15	0.10	8.86	0.78	8.8		
SPICE-A2	2.0707	1.687	1.14	0.10	9.11	0.85	9.3		
SPICE-A3	2.0711	1.651	1.09	0.09	8.49	0.76	8.9	8.58 [c]	0.76
SPICE-A3 [c]	2.0559	1.691	1.07	0.09	8.67	0.76	8.8		
SPICE-A4	2.1188	1.689	1.07	0.09	8.37	0.76	9.1	8.48 [c]	0.77
SPICE-A4 [c]	2.0803	1.695	1.07	0.09	8.59	0.78	9.1		
SPICE-A5	2.1358	1.694	1.06	0.09	8.24	0.76	9.2		
SPICE-A6	2.1112	1.691	1.03	0.09	8.08	0.75	9.3	8.28 [c]	0.76
SPICE-A6 [c]	2.0919	1.695	1.07	0.09	8.49	0.77	9.1		
SPICE-A7	2.0676	1.700	1.11	0.10	8.94	0.80	9.0		
SPICE-A8	2.1340	1.693	1.11	0.10	8.63	0.79	9.1		
SPICE-A8 [c]	2.1391	1.689	1.11	0.10	8.56	0.79	9.3	8.60 [c]	0.79
SPICE-A9	2.0503	1.702	1.05	0.09	8.52	0.78	9.2		
SPICE-A10	2.0525	1.696	1.05	0.09	8.44	0.77	9.2		
Process blanks									
Blank[d]		1.696	0.0155	0.0081					
Blank[d]		1.704	0.0235	0.0097					
Blank[e]		1.695	0.0175	0.0094					
Blank[e]		1.697	0.0304	0.0137					

Note: ^{10}Be concentrations in this table are not scaled to sea level and high latitude (SLHL). All uncertainties are **2σ**. A spike of approximately 250 microgram of ^{9}Be were added to each sample. Natural amounts of ^{9}Be were not measured in SP flow quartz samples.

[a] $^{10}Be/^{9}Be$ values are normalized using the standards of Nishiizumi et al. (2007). Standards and their nominal values used in these AMS measurements are KN01-6-2 ($^{10}Be/^{9}Be$ = 5.35×10^{-13}) and KN01-5-1 ($^{10}Be/^{9}Be$ = 2.709×10^{-11}). Uncertainties in our $^{10}Be/^{9}Be$ measurements include uncertainty in the number of counts and any scatter in the standards. The AMS standardization parameter 07KNSTD in the online calculator of Balco et al. (2008) indicates internal $^{10}Be/^{9}Be$ normalization to the Nishiizumi et al. (2007) standard, and is used with $^{10}Be/^{9}Be$ data from CologneAMS in the online calculator.

[b] Blank subtractions are between 1.7% to 2.2 % of the total ^{10}Be measured. Uncertainties in the blank corrected ^{10}Be concentrations include the propagated uncertainties in the total number of ^{10}Be atoms in the sample and the uncertainty in the ^{10}Be atoms in the blank, estimated from the mean and standard deviation of the pair of blank measurements included

in each sample batch. The uncertainty in the number of ^{10}Be atoms in the sample includes an estimated 1% (1 s.d.) uncertainty in the mass of ^{9}Be added to the sample, propagated with the uncertainty in the AMS ^{10}Be/^{9}Be measurement.

[c] Error-weighted (pooled) means and standard deviation of the means of duplicate AMS measurements are calculated for samples –A3, -A4, -A6, and –A8 after Wilson and Ward (1978).

[d] Processed alongside samples SPICE-A1 through SPICE-A5.

[e] Processed alongside samples SPICE-A6 through SPICE-A10.

Table SD3. Measured cosmogenic ^{14}C concentrations in SPICE quartz samples and associated laboratory blanks. All AMS measurements were made at the University of Cologne.

Sample ID	Mass sample (g)	µg C [a]	$^{14}C/^{12}C$ (10^{-13})[b]	2σ uncertainty (10^{-13})[b]	^{14}C (10^5 atoms)[c]	2σ uncertainty (10^5 atoms)	Blank-corrected ^{14}C concentration (10^5 at/g)[d]	2σ uncertainty (10^5 at/g)[d]
SPICE-A1	1.001	6.89	10.70	0.37	3.70	0.12	3.18	0.33
SPICE-A2	0.989	7.67	8.90	0.28	3.42	0.10	2.94	0.32
SPICE-A3	0.957	4.67	11.30	0.53	3.55	0.12	3.18	0.33
SPICE-A4	0.984	6.82	10.40	0.33	3.39	0.12	2.93	0.33
SPICE-A5	0.994	6.76	10.00	0.33	3.33	0.12	2.84	0.32
SPICE-A6	0.972	7.47	8.89	0.31	3.59	0.14	3.17	0.34
SPICE-A7	0.983	7.51	9.54	0.35	4.36	0.14	3.92	0.33
SPICE-A8	0.999	12.01	7.24	0.22	2.99	0.12	2.48	0.32
SPICE-A9	1.061	7.63	8.55	0.29	2.65	0.12	2.01	0.31
SPICE-A10	0.978	4.77	12.50	0.50	3.27	0.10	2.82	0.33
10SPCO6	1.052	8.69	9.07	0.30	3.95	0.14	3.27	0.31
10SPCO7	1.071	7.07	9.85	0.34	3.49	0.12	2.79	0.30

Process blanks	Mass of synthetic quartz (g)	µg C [a]	$^{14}C/^{12}C$ (10^{-13})[b]	2σ uncertainty (10^{-13})[b]	^{14}C (10^3 atoms)[c]	2σ uncertainty (10^3 atoms)
CGN 40	3.054	6.33	0.86	0.13	27	4
CGN 47	1.003	18.03	0.53	0.06	48	6
CGN 48	0.996	9.32	0.57	0.08	27	4
CGN 49	2.999	12.03	0.72	0.07	44	4
CGN 106	0.495	13.12	0.87	0.08	57	6
CGN 107	1.015	19.76	0.75	0.06	74	6
CGN 108	1.000	10.34	0.89	0.12	46	6
CGN 109	3.014	4.97	2.09	0.31	52	8
CGN 124 [d,e]	2.047	13.06	1.12	0.09	73	3
CGN 130 [d,e]	3.542	5.53	2.13	0.33	59	5

Note: ^{14}C concentrations in this table are not scaled to sea level and high latitude (SLHL). All uncertainties are **2σ**.

[a] Amount of carbon in carrier added, the carrier was added as $CaCO_3$ (fragments of a '^{14}C-dead' Iceland spar; Fülöp et al. 2015)

[b] $^{14}C/^{12}C$ values are normalized using the OX-II standard (N.I.S.T designation SRM 4990 C). Uncertainty quoted is the counting uncertainty.

[c] The ^{14}C concentration is calculated from the $^{14}C/^{12}C$ concentration determined by AMS multiplied by the ^{12}C content of the sample (i.e. carrier + sample). The amount of C provided is the sum of carbon in the carrier and any carbon in the sample. The carbon amount is determined on a calibrated capacitance manomenter (calibrated with accurately weighed amounts of carrier), after cryogenic separation of CO_2 from other gases.

[d] Blank subtractions are between 1.7% to 2.2 % of the total ^{14}C measured. Uncertainties in the blank corrected ^{14}C concentrations include the propagated uncertainties in the total number of ^{14}C atoms in the sample and the uncertainty in the ^{14}C atoms in the blank, estimated from the mean and standard deviation of all blank measurements.

Table SD4. *St*, *Sf*, and *Sa* scaling factors calculated for calibration sites on the SP lava flow.

	^{21}Ne, ^{10}Be, and ^{14}C	**^{21}Ne, ^{10}Be, and ^{14}C**	**^{21}Ne and ^{10}Be (over past 72 ka)**	**^{21}Ne and ^{10}Be (over past 72 ka)**	**^{14}C (over past 25 ka)**	**^{14}C (over past 25 ka)**	**^{10}Be (over past 72 ka)**	**^{10}Be (over past 72 ka)**	**^{14}C (over past 25 ka)**	**^{14}C (over past 25 ka)**	**^{14}C (over past 8270 yr)**	**^{14}C (over past 8270 yr)**	**^{14}C (over past 8270 yr)**	**^{14}C (over past 8270 yr)**
Sample ID	***St*** scaling factor for fast and slow muons [a]	***St*** scaling factor for neutron spallation [a]	***Sf*** scaling factor for fast and slow muons [b]	***Sf*** scaling factor for neutron spallation [b]	***Sf*** scaling factor for fast and slow muons [c]	***Sf*** scaling factor for neutron spallation [c]	***Sa*** scaling factor for fast and slow muons[b]	***Sa*** scaling factor for neutron spallation [b]	***Sa*** scaling factor for fast and slow muons[c]	***Sa*** scaling factor for neutron spallation [c]	***Sf*** scaling factor for fast and slow muons[d]	***Sf*** scaling factor for neutron spallation [d]	***Sa*** scaling factor for fast and slow muons[d]	***Sa*** scaling factor for neutron spallation [d]
SPICE-A1	1.993	3.515	1.506	3.861	1.498	3.602	1.506	4.021	1.498	3.582	1.490	3.522	1.490	3.498
SPICE-A2	1.965	3.445	1.496	3.777	1.488	3.524	1.496	3.931	1.488	3.505	1.480	3.446	1.480	3.423
SPICE-A3	1.968	3.452	1.497	3.786	1.489	3.533	1.497	3.941	1.489	3.513	1.481	3.454	1.481	3.431
SPICE-A4	1.962	3.436	1.495	3.766	1.486	3.515	1.495	3.920	1.486	3.495	1.479	3.437	1.479	3.414
SPICE-A5	1.959	3.430	1.494	3.758	1.485	3.507	1.494	3.911	1.485	3.488	1.478	3.430	1.478	3.406
SPICE-A6	1.938	3.379	1.486	3.697	1.478	3.451	1.486	3.847	1.478	3.432	1.471	3.375	1.471	3.352
SPICE-A7	1.959	3.430	1.494	3.758	1.485	3.507	1.494	3.911	1.485	3.488	1.478	3.430	1.478	3.406
SPICE-A8	1.939	3.380	1.486	3.698	1.478	3.452	1.486	3.848	1.478	3.433	1.471	3.376	1.471	3.353
SPICE-A9	1.968	3.452	1.497	3.786	1.489	3.533	1.497	3.941	1.489	3.513	1.481	3.454	1.481	3.431
SPICE-A10	1.959	3.430	1.494	3.758	1.485	3.507	1.494	3.911	1.485	3.488	1.478	3.430	1.478	3.406
10SPC01	2.031	3.609	1.520	3.974	--	--	--	--	--	--	--	--	--	--
10SPC06	1.958	3.427	1.493	3.755	1.485	3.504	--	--	1.485	3.485	1.477	3.427	1.477	3.403
10SPC07	1.946	3.399	1.489	3.721	1.481	3.473	--	--	1.481	3.454	1.473	3.396	1.473	3.373

Note: -- indicates a sample which was not analysed for the respective nuclide, and thus needs no scaling factor.

[a] The scaling factors were determined using CRONUSCalc (Marrero et al., 2016). Scaling factors are time independent.

[b] The scaling factors were determined using the mmc1 Matlab code of Lifton et al. (2014). Scaling factors are time-dependent. *Sf* scaling factors for ^{21}Ne and ^{10}Be and *Sa* scaling factors for ^{10}Be are integrated over the past 72 ka. There is no option for calculating Sa scaling factors for ^{21}Ne. *Sf* and *Sa* scaling factors for ^{14}C are integrated over the past 25 ka, the time at which ^{14}C reaches 95% saturation.

[c] *Sf* and *Sa* scaling factors for ^{14}C are integrated over the past 25 ka, the time at which ^{14}C reaches 95% saturation.

[d] *Sf* and *Sa* scaling factors for ^{14}C are integrated over the past 8270 a, based on the integration time equations 7 and 9 from Blard et al. (2019).

Table SD5. Local production-rate ratios and production-rate ratios for total reference ^{21}Ne and spallogenic $^{10}Be_{sp}$ and $^{14}C_{sp}$ in SP-flow quartz.

(a) Scaled with St scaling factors Sample ID	$^{21}Ne/^{10}Be$	2σ Uncertainty	$^{21}Ne/^{14}C$	2σ Uncertainty	$^{14}C/^{10}Be$	2σ Uncertainty	$^{21}Ne/^{10}Be_{sp}$	2σ Uncertainty	$^{21}Ne/^{14}C_{sp}$	2σ Uncertainty	$^{14}C_{sp}/^{10}Be_{sp}$	2σ Uncertainty
SPICE-A1	4.29	0.61	1.39	0.21	3.08	0.43	4.41	0.76	1.68	0.36	2.63	0.61
SPICE-A2	4.49	0.63	1.63	0.25	2.76	0.41	4.61	0.80	1.98	0.45	2.33	0.58
SPICE-A3	4.37	0.58	1.38	0.20	3.17	0.45	4.49	0.74	1.65	0.35	2.73	0.64
SPICE-A4	4.37	0.53	1.48	0.20	2.96	0.44	4.49	0.71	1.79	0.39	2.51	0.62
SPICE-A5	4.45	0.65	1.54	0.25	2.90	0.44	4.58	0.81	1.87	0.44	2.45	0.62
SPICE-A6	4.25	0.64	1.29	0.21	3.28	0.48	4.37	0.79	1.54	0.34	2.83	0.67
SPICE-A7	4.35	0.70	1.07	0.17	4.07	0.53	4.47	0.85	1.23	0.24	3.64	0.75
SPICE-A8	4.69	0.61	1.90	0.30	2.47	0.41	4.82	0.79	2.39	0.62	2.02	0.57
SPICE-A9	4.39	0.82	2.17	0.48	2.03	0.37	4.52	0.95	2.90	1.00	1.56	0.52
SPICE-A10	4.66	0.60	1.73	0.26	2.70	0.41	4.78	0.78	2.11	0.49	2.27	0.57
10SPC06	--	--	1.28	0.17	--	--	--	--	1.53	0.30	--	--
10SPC07	--	--	1.78	0.25	--	--	--	--	1.82	0.35	--	--

(b) Scaled with *Sf* scaling factors Sample ID	$^{21}Ne_{sp}/^{10}Be_{sp}$	2σ Uncertainty	$^{21}Ne_{sp}/^{14}C_{sp}$	2σ Uncertainty	$^{14}C_{sp}/^{10}Be_{sp}$	2σ Uncertainty		**(c) Scaled with *Sa* scaling factors** Sample ID	$^{14}C_{sp}/^{10}Be_{sp}$	2σ Uncertainty
SPICE-A1	4.41	0.76	1.64	0.34	2.94	0.65		SPICE-A1	3.08	0.68
SPICE-A2	4.61	0.80	1.93	0.41	2.61	0.62		SPICE-A2	2.73	0.64
SPICE-A3	4.49	0.74	1.61	0.33	3.04	0.68		SPICE-A3	3.19	0.71
SPICE-A4	4.49	0.71	1.74	0.36	2.81	0.66		SPICE-A4	2.94	0.69
SPICE-A5	4.58	0.81	1.82	0.41	2.74	0.66		SPICE-A5	2.87	0.69
SPICE-A6	4.37	0.79	1.51	0.32	3.15	0.72		SPICE-A6	3.30	0.69
SPICE-A7	4.47	0.85	1.21	0.23	4.01	0.80		SPICE-A7	4.20	0.84
SPICE-A8	4.82	0.79	2.30	0.56	2.28	0.61		SPICE-A8	2.38	0.64
SPICE-A9	4.52	0.95	2.74	0.88	1.79	0.55		SPICE-A9	1.88	0.58
SPICE-A10	4.78	0.78	2.05	0.45	2.54	0.61		SPICE-A10	2.66	0.64
10SPC06	--	--	1.49	0.27	--	--		10SPC06	--	--
10SPC07	--	--	2.15	0.45	--	--		10SPC07	--	--

Supplementary Material – photographs of SPICE sample sites.

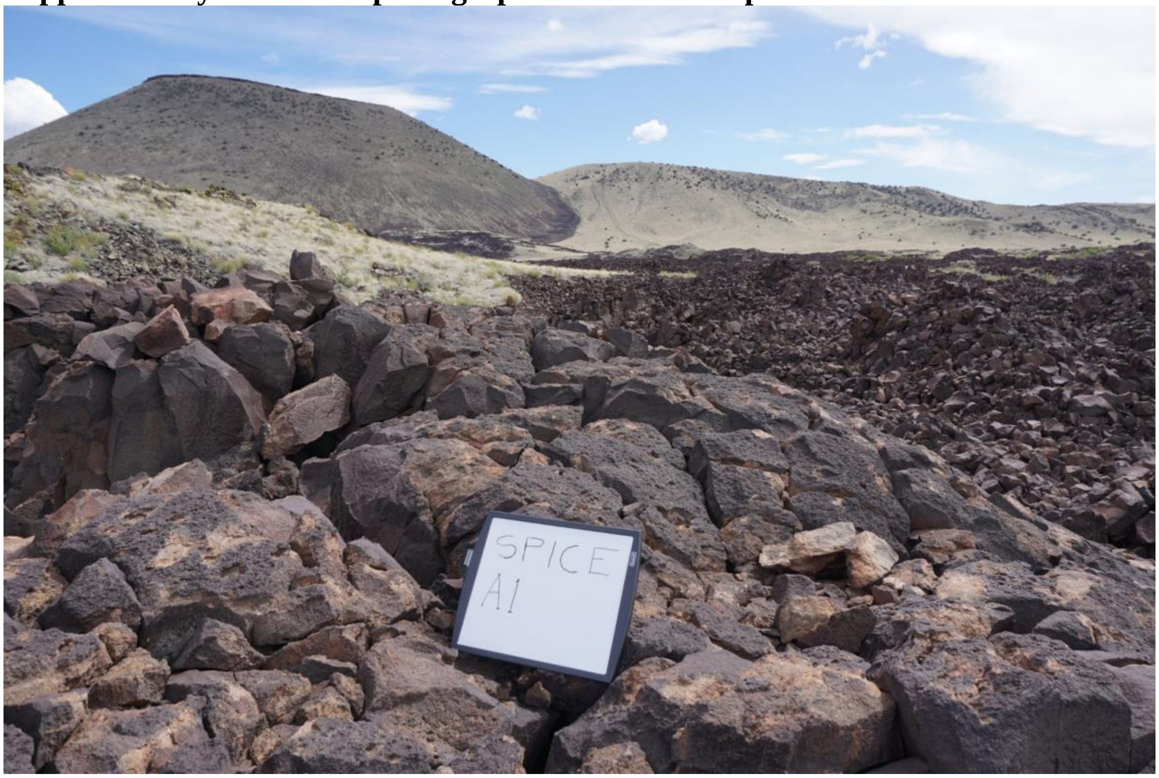

Figure S1. Photographs of sample site SPICE-A1.

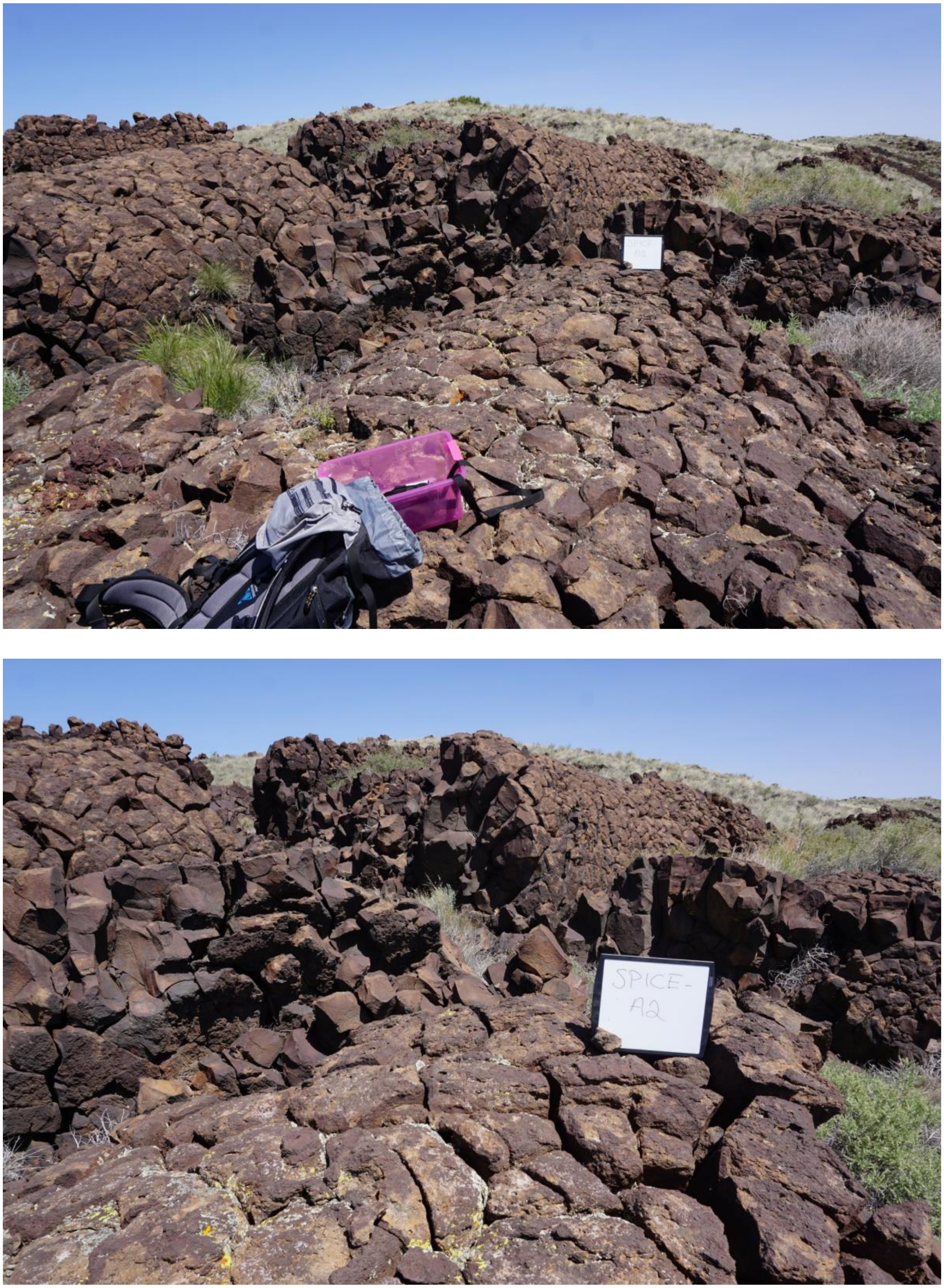

Figure S2. Photographs of sample site SPICE-A2.

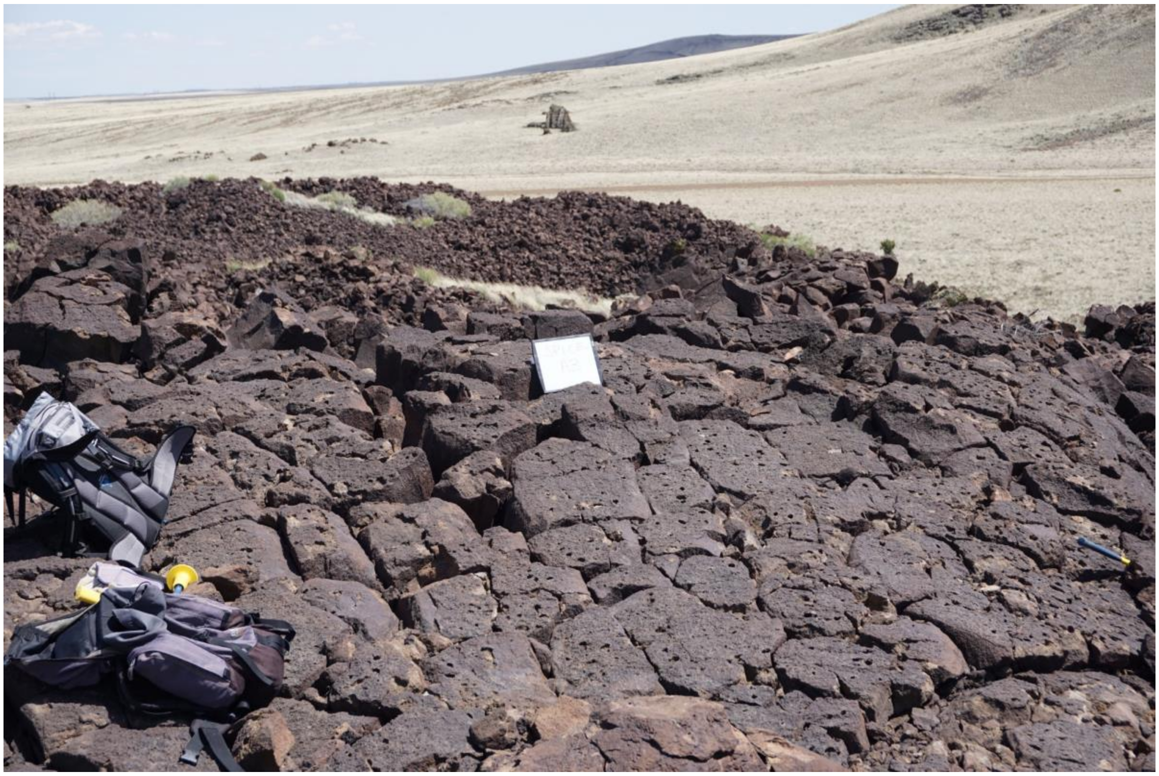

Figure S3. Photographs of sample site SPICE-A3.

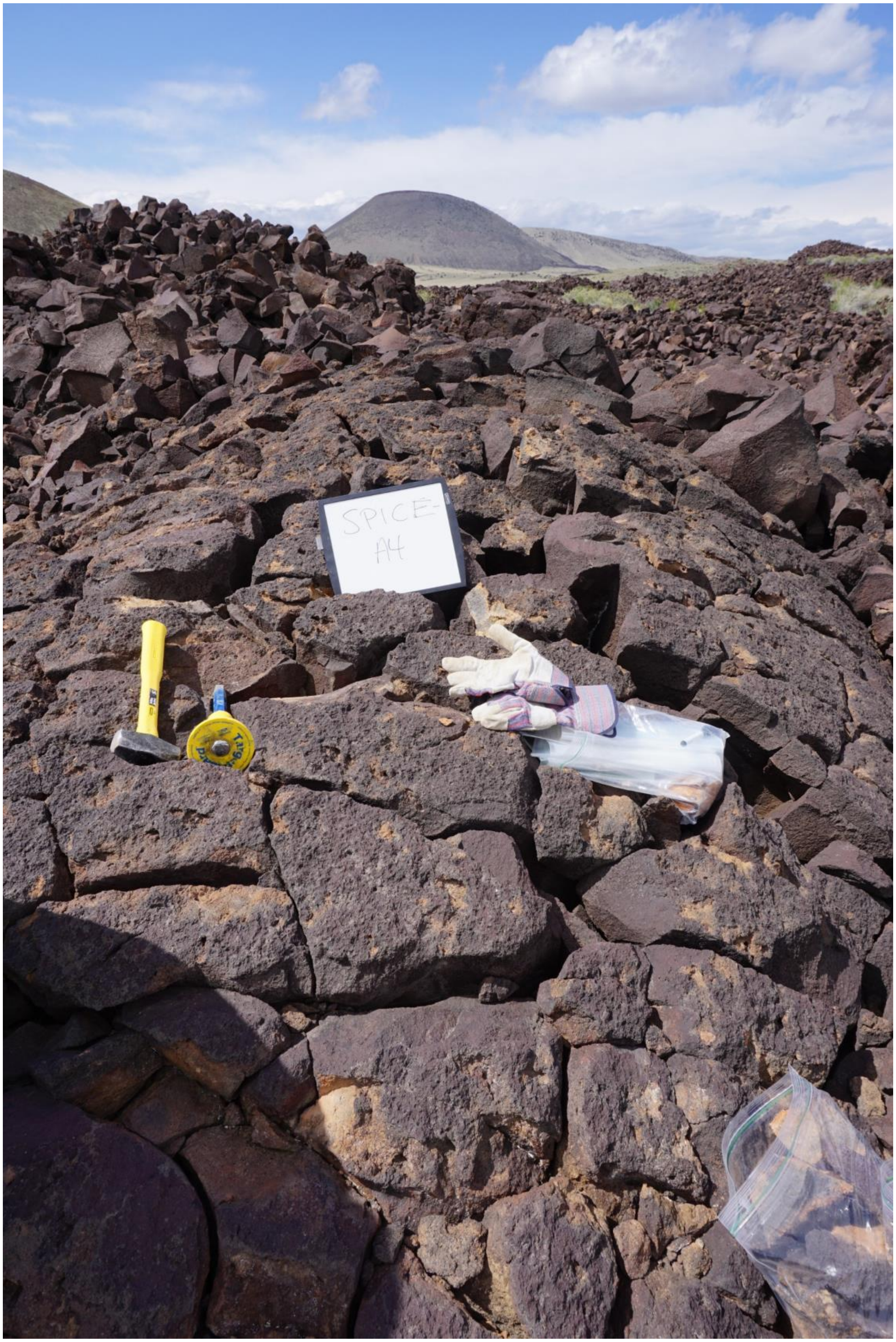

Figure S4. Photographs of sample site SPICE-A4.

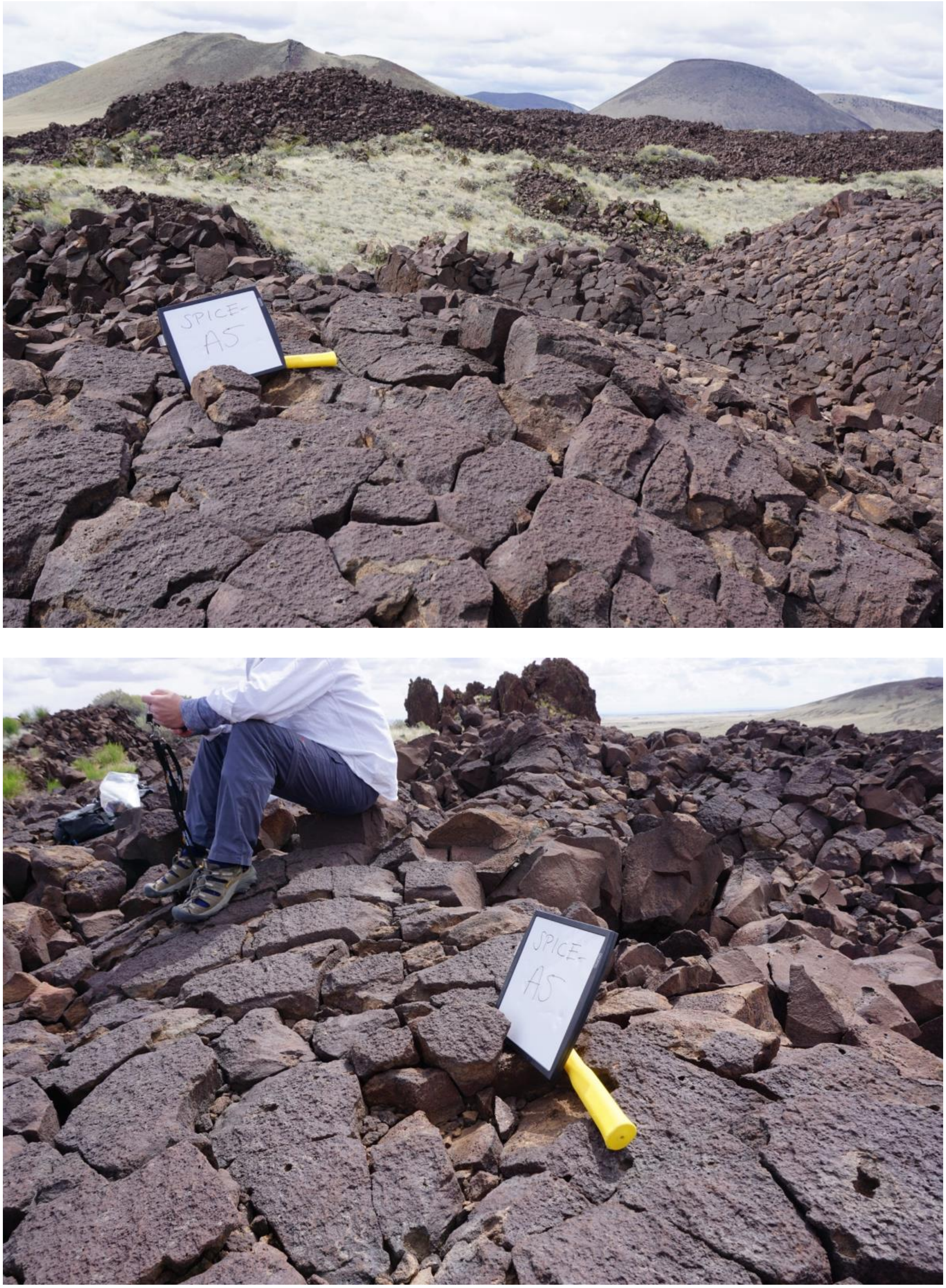

Figure S5. Photographs of sample site SPICE-A5.

Figure S6. Photographs of sample site SPICE-A6.

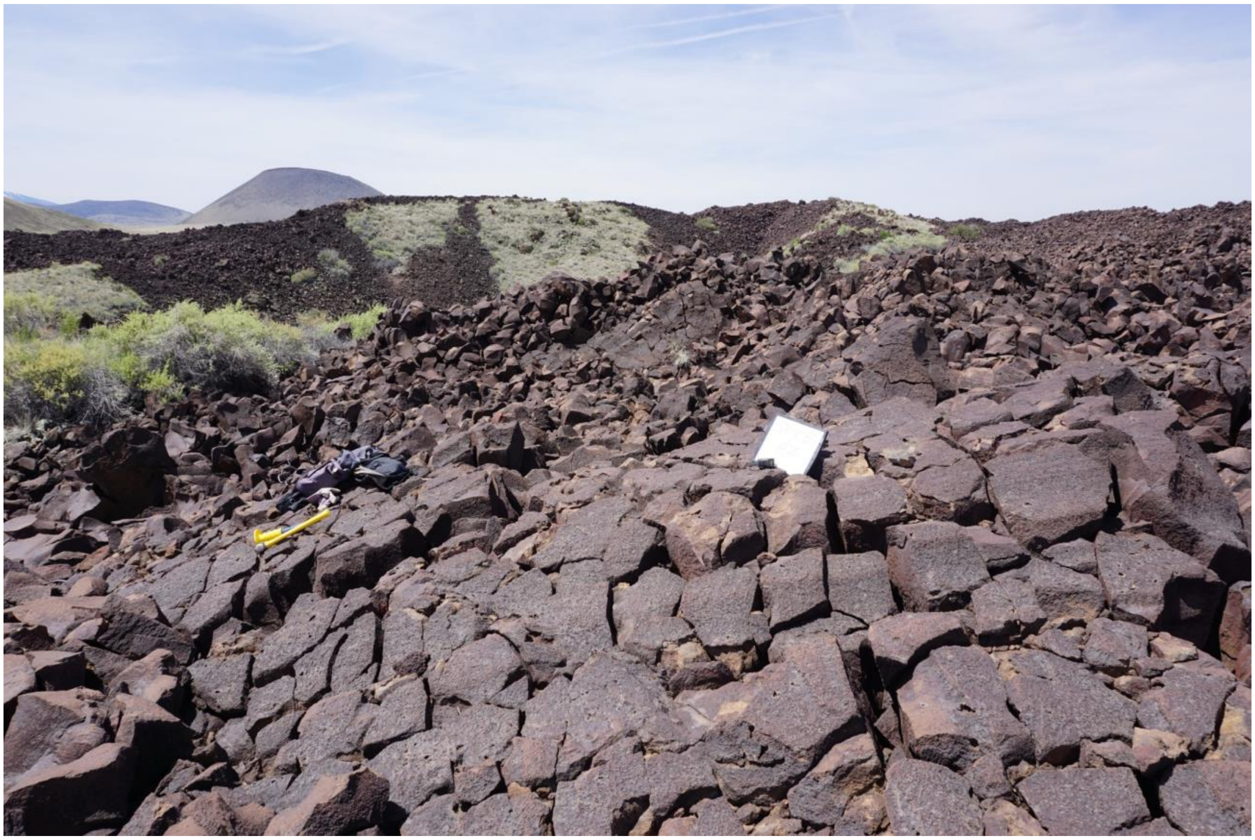

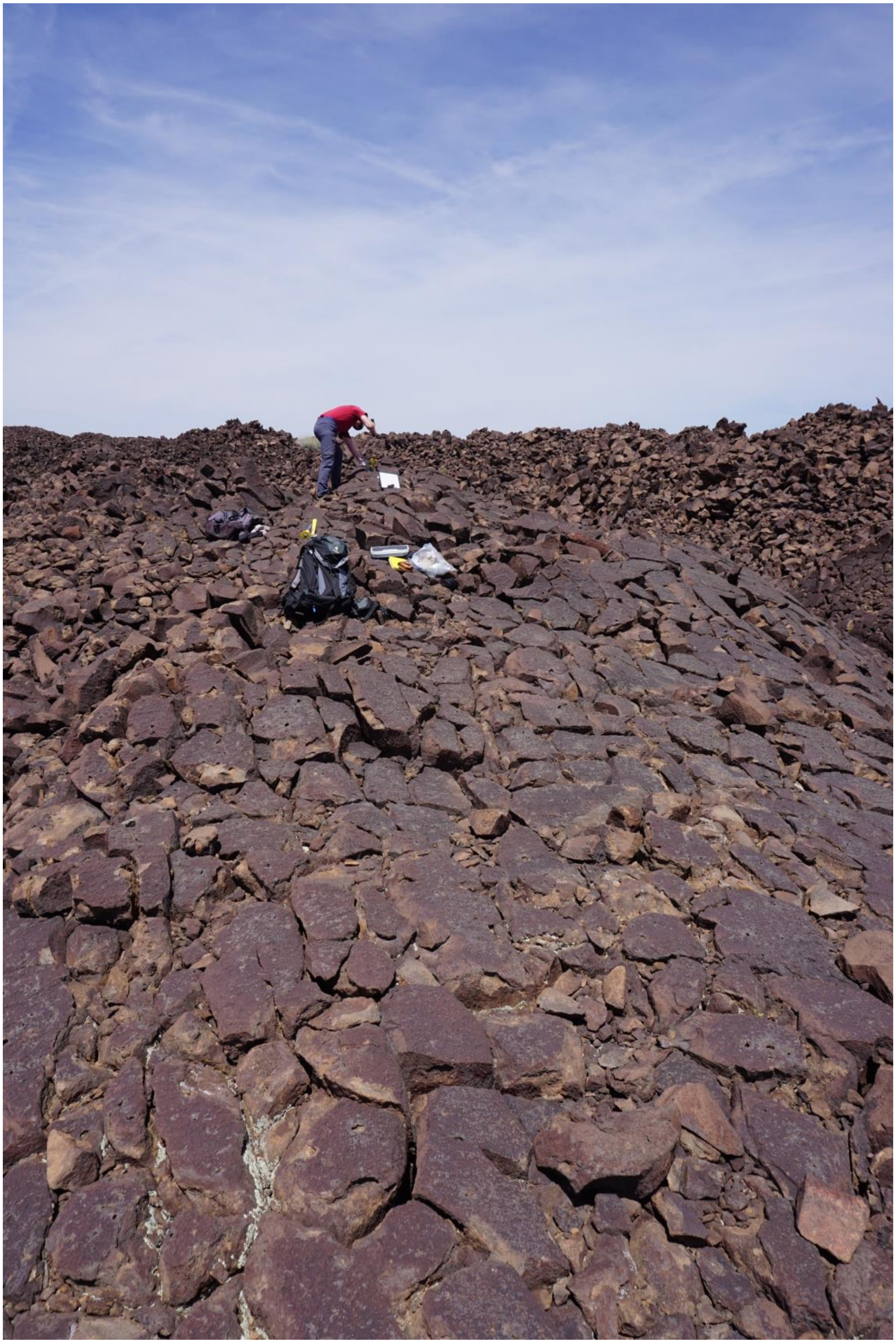

Figure S7. Photographs of sample site SPICE-A7.

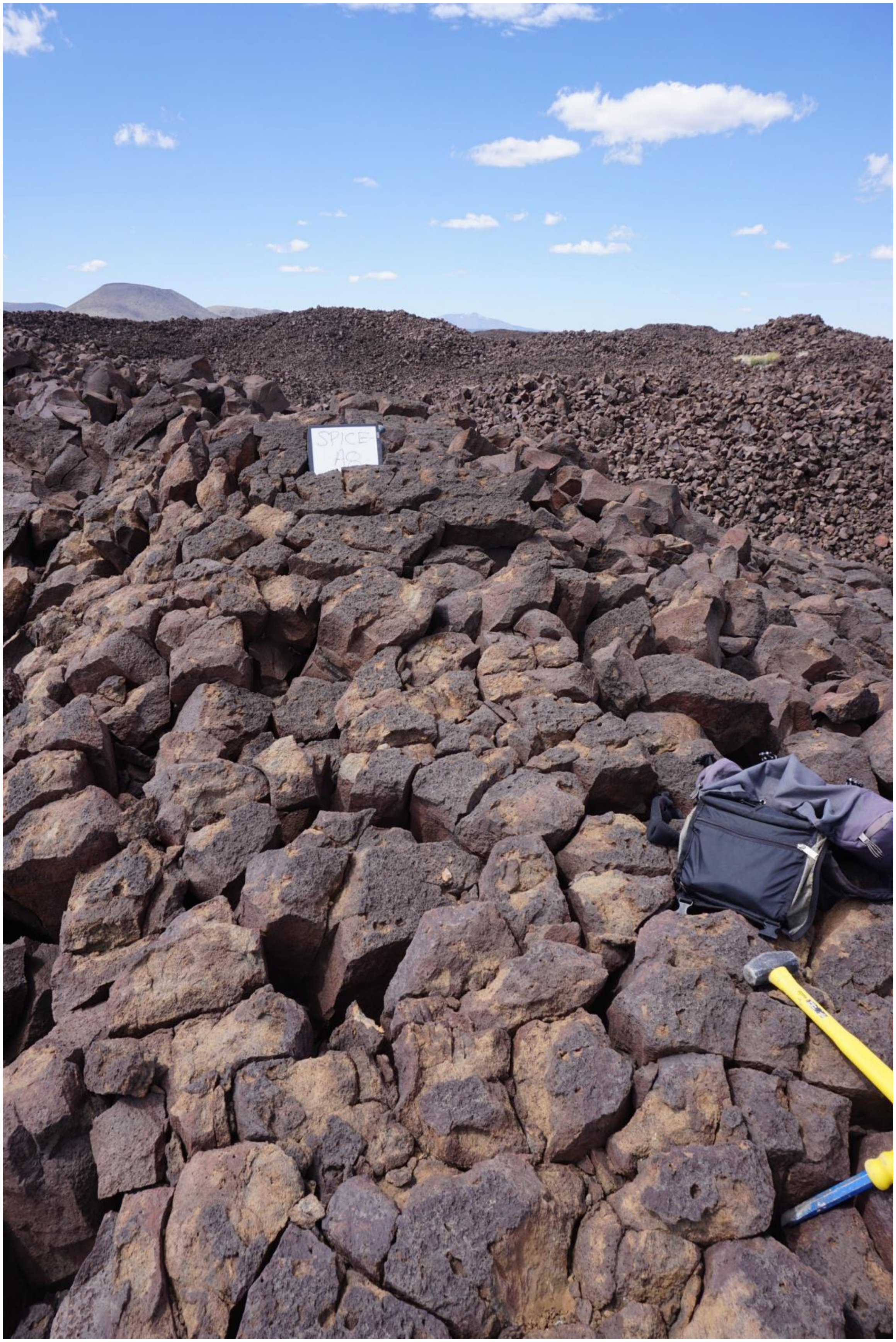
SPICE
A9

Figure S8. Photographs of sample site SPICE-A8.

Figure S9 (a and b). Photographs of sample site SPICE-A9.

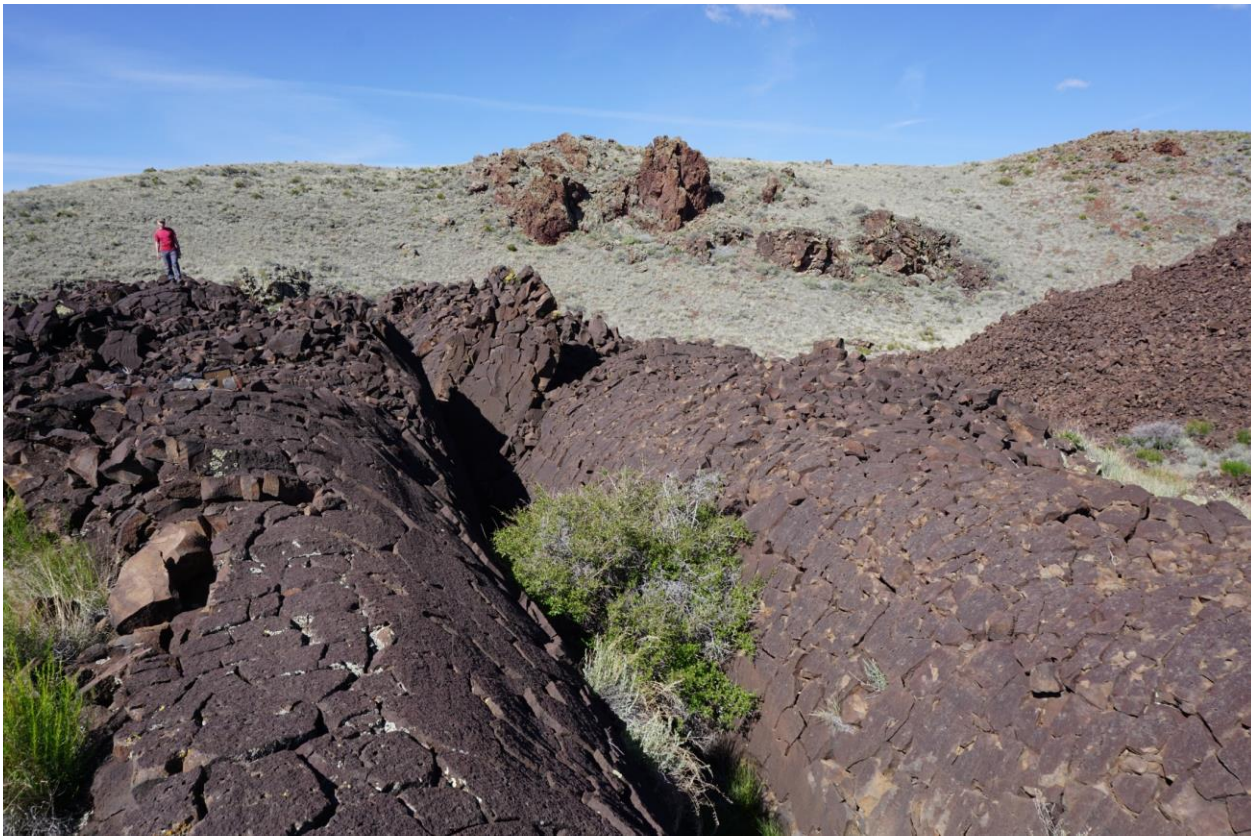

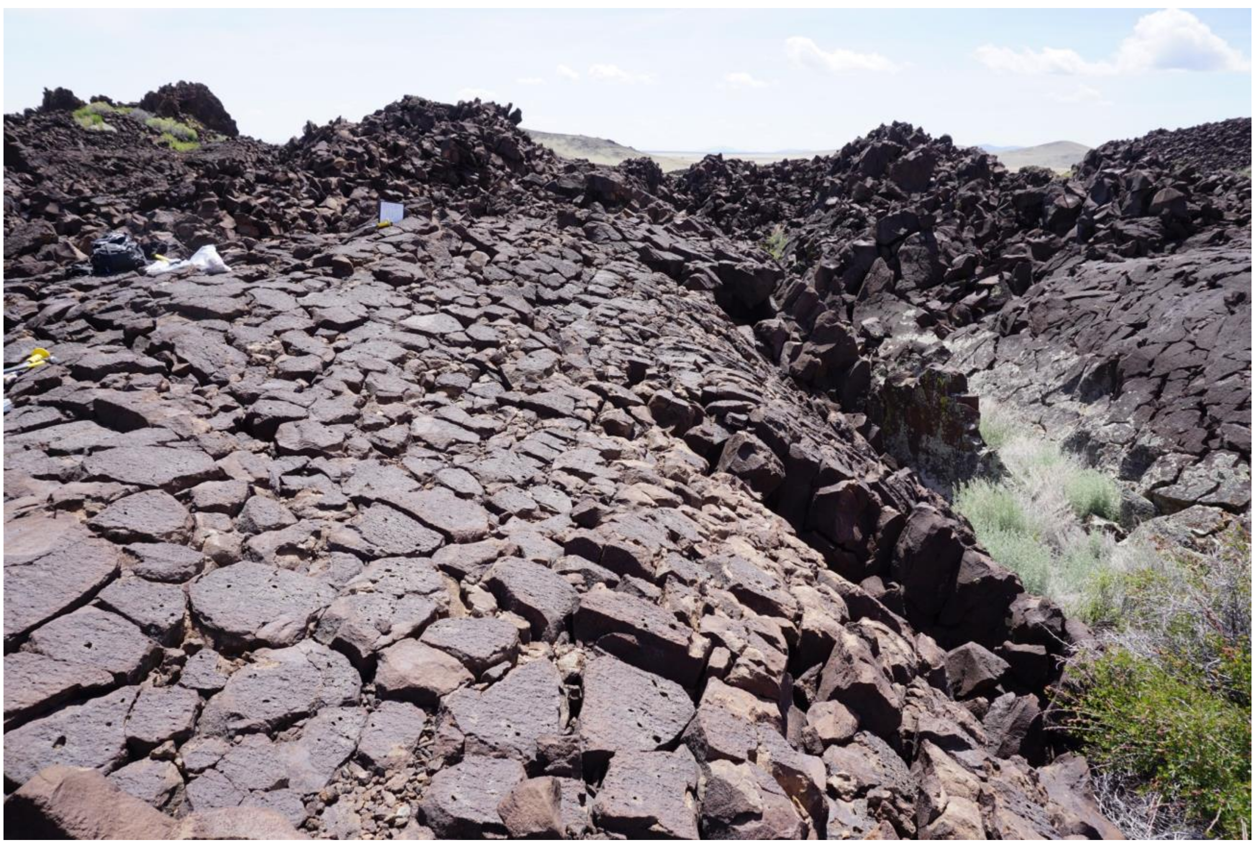

Figure S10. Photographs of sample site SPICE-A10.

Figure S10. Photographs of sample site SPICE-A10.

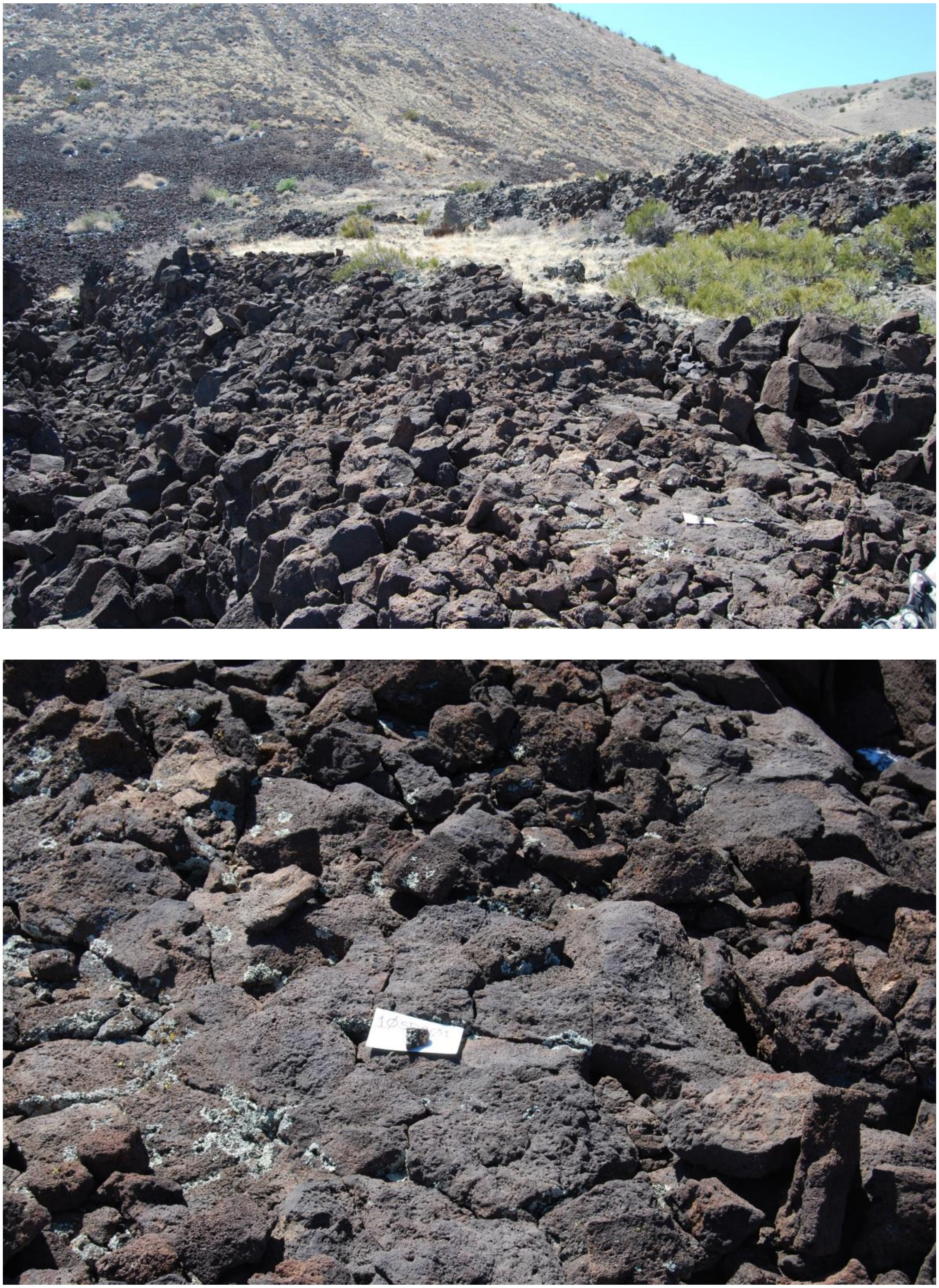

Figure S11. Photographs of sample site 10SPC01.

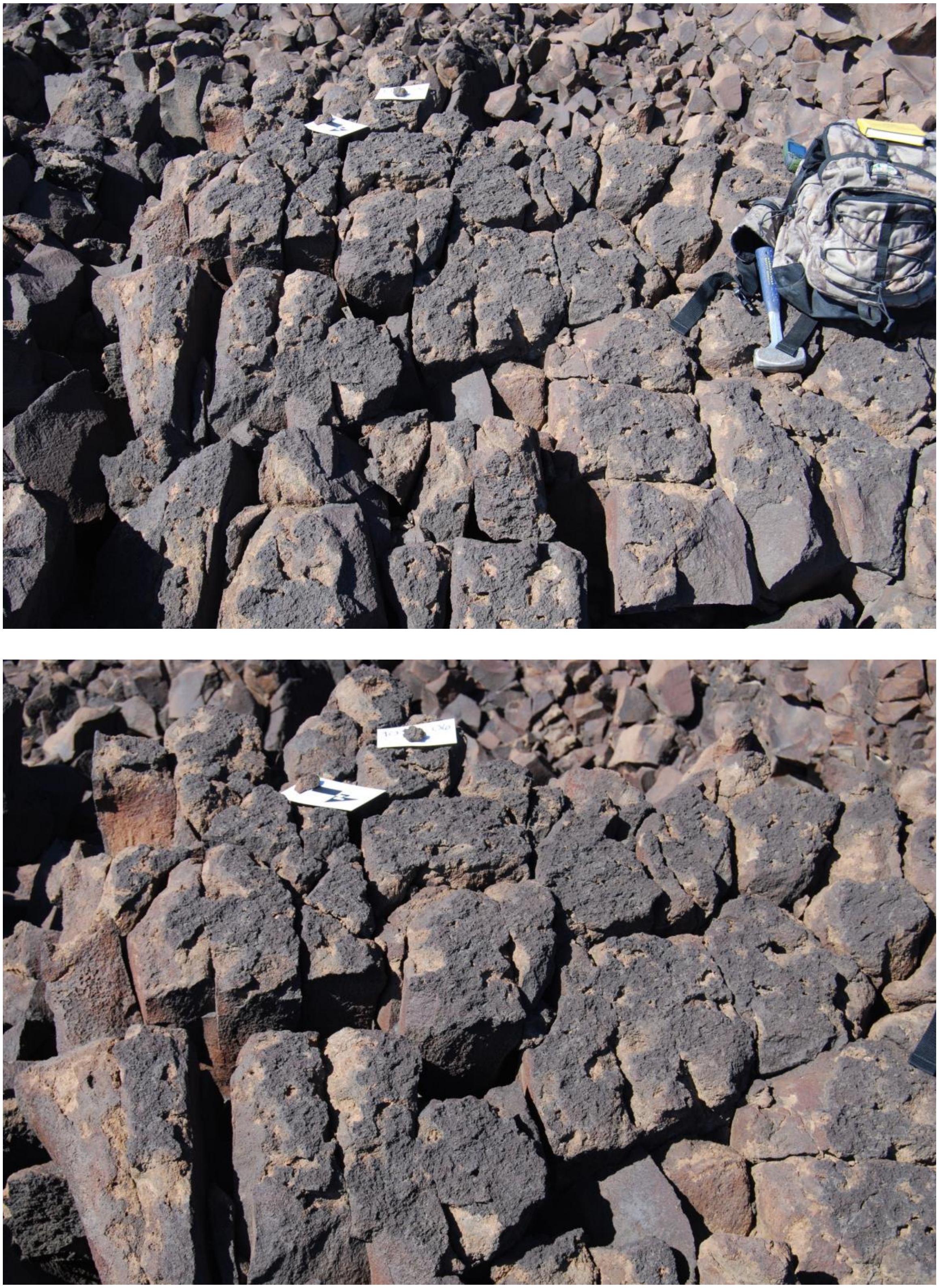

Figure S12. Photographs of sample site 10SPC06.

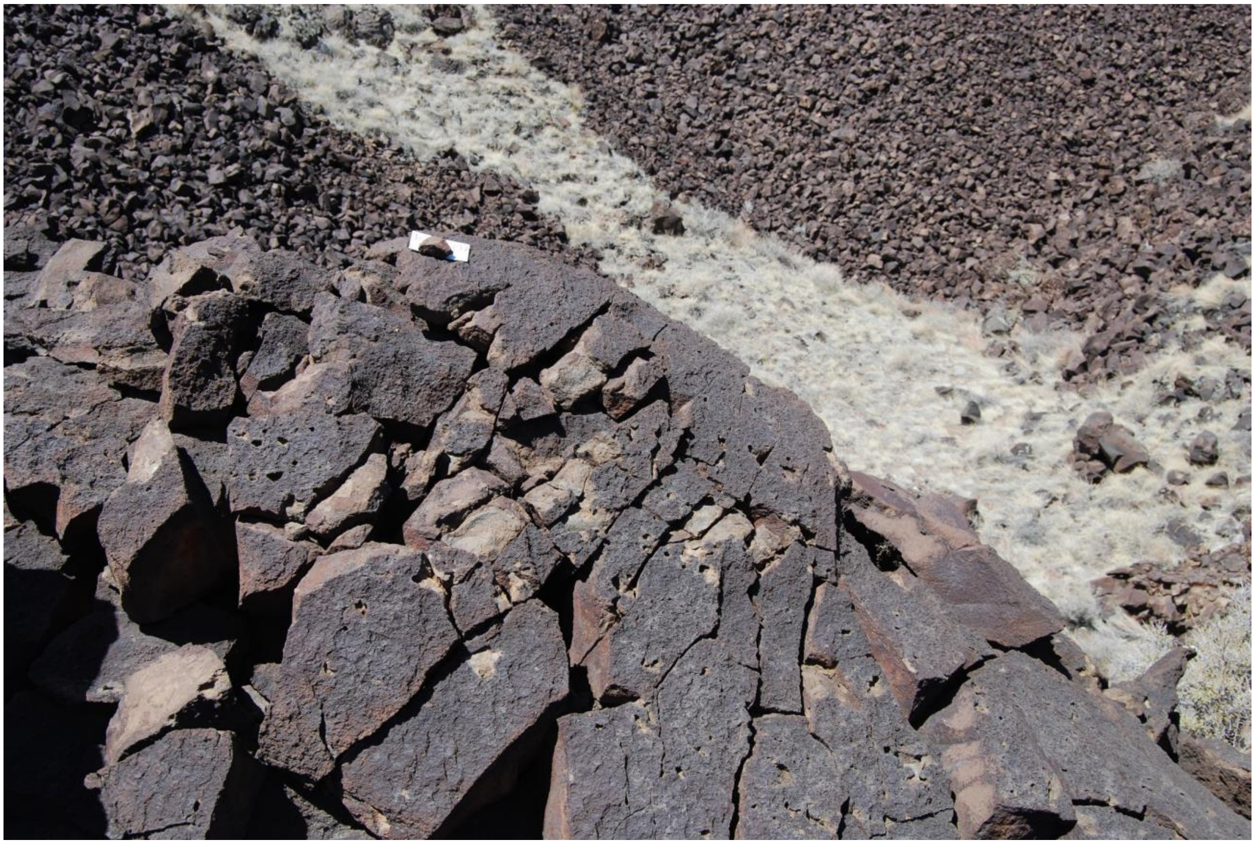

Figure S13. Photograph of sample site 10SPC07.